Energetic ion dynamics near Callisto

Lucas Liuzzo [a,*], Sven Simon [a], Leonardo Regoli [b]

[a] School of Earth and Atmospheric Sciences, Georgia Institute of Technology, 311 Ferst Drive, Atlanta, GA, 30332, USA
[b] Department of Climate and Space Sciences and Engineering, University of Michigan, Ann Arbor, MI, USA

A B S T R A C T

We examine the dynamics of energetic magnetospheric ions in the highly perturbed and asymmetric electromagnetic environment of the Jovian moon Callisto. The Alfvénic interaction of the (nearly) corotating magnetospheric plasma with Callisto's ionosphere and induced dipole generates electromagnetic field perturbations near the moon, the structure of which vary as a function of Callisto's orbital position. For this study, these perturbations are obtained from the AIKEF hybrid model (kinetic ions, fluid electrons) which has already been successfully applied to Callisto's local plasma environment (Liuzzo et al., 2015, 2016, 2017). To isolate the influence of Callisto's ionosphere and induced dipole field on energetic ion dynamics, we analyze the trajectories of energetic hydrogen, oxygen, and sulfur ions exposed to various configurations of the locally perturbed electromagnetic fields. We present spatially resolved surface maps that display accessibility of Callisto to these ion populations for select energies from 1 keV to 5000 keV. The Alfvénic plasma interaction with (i) Callisto's induced magnetic field, (ii) Callisto's ionosphere, and (iii) the combination of both, all leave distinct imprints in these accessibility patterns. Draping of the magnetospheric field around Callisto's ionosphere partially shields the moon's trailing (ramside) hemisphere from energetic ion impacts, and the induced field tends to focus energetic ion impacts near Callisto's Jupiter-facing and Jupiter-averted apices. Depending on the nature of Callisto's Alfvénic plasma interaction, the accessibility of its surface to energetic protons may evolve non-monotonically with increasing energy. We also present maps of energetic ion accessibility and the resulting energy deposition onto Callisto at the time of the Galileo C3, C9, and C10 flybys. Our findings show that the shielding of Callisto's surface from energetic ion impacts is most effective during flybys that took place while the moon was located at an intermediate distance to the center of Jupiter's magnetospheric current sheet. In this case, the ionosphere and induced dipole field both make substantial contributions to the electromagnetic field perturbations near Callisto.

1. Introduction

The magnetospheric plasma near Jupiter's second-largest moon Callisto (radius $R_C = 2,410$ km) consists of two distinct populations. The first is the "thermal" plasma population with energies below $E \approx 10$ keV, which was the lower detection threshold of the *Energetic Particles Detector* (EPD) on board the Galileo spacecraft (Williams et al., 1992). Due to the 9.6° tilt between Jupiter's magnetic and rotational axes, there is considerable variability in composition and density of the thermal population at Callisto's orbital distance of $26.3R_J$ ($R_J = 71,492$ km), as Jupiter's plasma sheet continually sweeps over the moon with an approximately 10 h periodicity. On average, however, the mass of the thermal magnetospheric ions near Callisto is approximately $m = 16$ amu, with a number density of $n \approx 0.1$ cm^{-3} and an average charge of $q = 1.5e$ (Kivelson et al., 2004). The thermal plasma nearly corotates with Jupiter, and

therefore continuously impinges onto Callisto's ramside hemisphere (i.e., the trailing hemisphere with respect to the moon's orbital motion) at an average relative velocity of $u_0 \approx 192$ km/s.

The Jovian magnetic field, frozen into the corotating magnetospheric plasma, drapes around Callisto's induced magnetic field (e.g., Zimmer et al. (2000)) and its ionosphere (e.g., Kliore et al. (2002)), generating Alfvén wings (e.g., Liuzzo et al. (2016)). The auroral footprint of Callisto, an optical manifestation of this electromagnetic interaction, has recently been identified in observations of Jupiter's polar ionosphere by the Hubble Space Telescope (Bhattacharyya et al., 2017). Plasma from Callisto's ionosphere, freshly created predominately via solar ultraviolet ionization, is picked-up and convected downstream by the $\mathbf{E} \times \mathbf{B}$ drift. Callisto's Alfvénic interaction with the thermal Jovian plasma population has been studied analytically by, e.g., Neubauer (1999) and Strobel et al. (2002). Moreover, the local magnetic field and plasma perturbations near

Callisto have recently been investigated by, e.g., the hybrid (kinetic ions, fluid electrons) modeling studies of Liuzzo et al. (2015, 2016, 2017). These studies found that the magnetic field perturbations measured by Galileo (Khurana et al., 1998; Kivelson et al., 1999), as well as the plasma density enhancements observed in Callisto's wake (Gurnett et al., 2000), can be attributed to the moon's interaction with the thermal plasma population alone.

The second magnetospheric plasma population near Callisto's orbital distance is made up of particles at the high-energy end of the distribution function, with energies beginning near $E = 10$ keV (i.e., the lower range of the Galileo EPD) and exceeding $E = 10$ MeV. The number density of this "energetic" population does not exceed $n \approx 0.01$ cm^{-3}, and this plasma is comprised of electrons as well as hydrogen, oxygen, and sulfur ions (Mauk et al., 2004). As these energetic particles have only minor quantitative impact on the local electromagnetic perturbations associated with Callisto (e.g., Zimmer et al. (2000); Liuzzo et al. (2015, 2016, 2017)), they can be treated as test particles exposed to a pre-defined electromagnetic field configuration that have no feedback on the fields themselves.

Since the arrival of the Galileo spacecraft at Jupiter in 1995, multiple studies have used data from the EPD to investigate energetic particle dynamics near the three icy Galilean moons. At Ganymede, Ip et al. (1997) used EPD measurements to determine the ion sputtering rate of the moon's surface, and found that energetic ion precipitation onto the surface may contribute to generation of the moon's extended exosphere. Using data from the Ganymede G8 flyby, Williams et al. (1997a) identified energetic electrons that were trapped on closed magnetic field lines of Ganymede's intrinsic field. In a follow-up study, Williams et al. (1998) used EPD measurements to identify regions of slowed thermal magnetospheric plasma that extend for multiple R_J along field lines connecting Ganymede with Jupiter. These authors also identified electron loss cone signatures during multiple flybys of the moon. Recently, Fatemi et al. (2016) modeled Ganymede's electromagnetic interaction with the Jovian thermal plasma population using a hybrid model. While these authors did not use data from the EPD, they applied the electromagnetic field output from their hybrid model to study the effects of Ganymede's Alfvénic plasma interaction on energetic ion dynamics, and were able to correlate energetic ion fluxes onto the moon's surface with the observed brightness patterns of its high-latitude polar regions.

At Europa, Ip et al. (1998) applied EPD measurements to constrain the ion sputtering rate of the moon's surface, and suggested that the surface may be subjected to strong erosion by charged particles from Jupiter's magnetosphere. Paranicas et al. (2001) investigated the energetic electron population measured by the EPD near Europa. These authors found that electron precipitation onto the moon's surface was confined to its trailing (ramside) hemisphere, due to the electron bounce times being much smaller than the transit time of magnetic flux tubes across the moon. They also postulated that the hemispherical differences in albedo observed at Europa are mainly caused by this asymmetric electron bombardment, and not by ion bombardment as was previously suggested by Pospieszalska and Johnson (1989). Paranicas et al. (2002) analyzed the flyby-to-flyby variability of EPD spectra collected near Europa, and estimated radiation dose rates into Europa's surface up to a depth of 1 m. This study found that, unlike the energetic electron population, ions have a more uniform access to Europa's surface and are therefore responsible for radiolysis of Europa's leading (wakeside) hemisphere.

Cooper et al. (2001) presented EPD fluxes for the ambient, magnetospheric energetic plasma population measured near Europa, Ganymede, and Callisto, and calculated global fluxes and radiation dose rates of energetic particles precipitating onto the surface of each moon. Using a superposition of the intrinsic dipolar magnetic field of Ganymede with Jupiter's background field, these authors applied a test particle simulation to trace trajectories of energetic protons near the moon. They identified regions of Ganymede's surface that were shielded from energetic particles of certain energies due to the closed field lines of the moon's intrinsic dipole.

Several modeling studies of energetic particle dynamics near Europa have used a similar test particle approach as Cooper et al. (2001). By assuming a uniformly southward magnetospheric field orientation (i.e., by assuming Europa's interaction with the thermal plasma population to be weak and by neglecting Europa's induced dipole field), Cassidy et al. (2013) generated spatially-resolved maps of energetic ion fluxes and sputtering rates of Europa's surface. These authors found that, while precipitation of high-energy ions was largest at Europa's poles, the sputtering rates of Europa's surface peaked near the moon's dayside equator due to the locally enhanced surface temperature and the increased sputtering efficiency of the thermal (corotating) ion population at low latitudes. A companion study by Dalton et al. (2013) similarly used a test particle approach with uniform electromagnetic fields near Europa to investigate the dynamics of energetic electrons. These authors show that, unlike energetic ion fluxes, the electron fluxes onto Europa's surface peak in the equatorial region of the moon's trailing hemisphere. However, the degree to which energetic particle dynamics and the resulting surface fluxes and sputtering rates are affected by Europa's interaction with the thermal magnetospheric plasma or by Europa's induced dipole was not considered by either of these studies, and remains unexplored.

So far, no study has modeled energetic particle dynamics near Callisto and the resulting patterns of precipitation onto the moon. Therefore, the major goal of this study is to close the gap in the understanding of Callisto's local plasma environment by investigating the dynamics of energetic ions near the moon, as has already been done at Ganymede and Europa. However, in contrast to preceding studies of energetic ion dynamics near Europa, our study will include the electromagnetic perturbations generated by Callisto's Alfvénic interaction with the thermal plasma.

Near Titan and the icy moons of Saturn, these electromagnetic interactions were found to play a crucial role for energetic particle dynamics. For example, although the interactions of the icy moons Dione and Rhea with the Saturnian magnetospheric plasma generate only weak electromagnetic field perturbations (Simon et al., 2011, 2012), particle tracing studies of electron dynamics near Rhea and Dione found that even these weak perturbations have a drastic effect on the trajectories of energetic electrons near these moons (Roussos et al., 2012; Krupp et al., 2013). These studies have shown that complex trajectories of the energetic electrons form as a result of the plasma interaction, with some regions near the moons completely inaccessible to these particles. Additionally, Kotova et al. (2015) showed that the local electromagnetic field perturbations generated by Rhea's and Dione's interactions needed to be taken into account in order to explain the intensities of energetic ion fluxes (between $E = 30$ keV and $E = 600$ keV) measured by the *Low Energy Magnetospheric Measurement System* on board Cassini during multiple flybys of these moons.

At Titan, Regoli et al. (2016) investigated energetic particle dynamics during the Cassini T9 flyby. Using results from a hybrid model (Feyerabend et al., 2015), that study included the local electromagnetic field perturbations generated by Titan's interaction with Saturn's outer magnetospheric plasma. By tracing the trajectories of energetic test particles in the 1 keV–1000 keV range, Regoli et al. (2016) found that the local electromagnetic field perturbations had a tremendous effect on the accessibility of Titan's exobase to energetic ions. Especially for 1 keV–100 keV ions, particles were channeled to the exobase through Titan's magnetic neutral region in its leading (wakeside) hemisphere due to the reduced magnetic field strength within this region, whereas magnetic pileup in Titan's trailing (ramside) hemisphere reduced energetic particle accessibility there.

In many respects, Titan's thermal plasma interaction is highly analogous to Callisto's. At both moons, the gyroradii r_g of thermal magnetospheric and newly generated ionospheric ions clearly exceed the radii of Callisto and Titan, which generates substantial asymmetries in the magnetospheric flow deflection around each moon. These large gyroradii are also responsible for the asymmetric pileup of magnetospheric field lines upstream of each moon: at both bodies, the ramside magnetic pileup

region is stretched by up to several moon radii into the hemisphere where the convective electric field points away from the moon (e.g., Feyerabend et al. (2015) and Liuzzo et al. (2015)). The Alfvénic Mach numbers of the incident Jovian or Saturnian plasma can assume a wide range of values at both moons, even exceeding unity (e.g., Kivelson et al. (2004); Arridge et al. (2011)). Additionally, the Alfvén conductances of the magnetospheric plasmas near Callisto and Titan are on the order of $\Sigma_A \approx 1$ S, which is small compared to the ionospheric Pedersen and Hall conductances on the order of $\Sigma_{P,H} \approx 10^3$ S (Strobel et al., 2002; Rosenqvist et al., 2009). These large transverse conductance values are responsible for strong currents within Callisto's and Titan's ionospheres which, in turn, generate strong magnetic draping signatures (on the order of the background field magnitude) and Alfvén wing currents.

Despite these similarities, Callisto's plasma interaction is even more complex than Titan's. Due to the tilt between Jupiter's magnetic and rotational axes, currents are induced in Callisto's conducting subsurface ocean which manifest as a time-varying dipolar field outside of the moon (Khurana et al., 1998; Kivelson et al., 1999; Zimmer et al., 2000). As shown by Hartkorn and Saur (2017), magnetic field data from the Galileo C3 flyby of Callisto can alternatively be explained by a (quasi-) dipolar field induced within the moon's ionosphere, without inclusion of a conducting subsurface layer. However, this approach did not succeed in quantitatively reproducing magnetic field data from any other Callisto flyby. The interaction of the thermal magnetospheric plasma with the obstacle (that consists of Callisto's ionosphere *and* induced field) includes the formation of a quasi-dipolar "core region" downstream of the moon (at altitudes below $1R_C$) where the induced field dominates the local magnetic perturbations; farther from the moon, field line draping dominates (Liuzzo et al., 2016).

The contributions of Callisto's ionosphere and induced dipole to the electromagnetic interaction change systematically as a function of System III longitude and local time (e.g., Liuzzo et al. (2015, 2016, 2017)). Understanding the influence of these changes on energetic particle dynamics is especially important, since Callisto's induced magnetic field periodically vanishes on a time-scale of approximately 5 h as Jupiter's current sheet sweeps over the moon. When Callisto is located close to the center of the Jovian magnetospheric current sheet where the induced field nearly vanishes, the electromagnetic perturbations are therefore dominated by Callisto's ionosphere-magnetosphere interaction (e.g., Liuzzo et al. (2015, 2017)). Conversely, at large distances to the center of Jupiter's current sheet, the dipole-magnetosphere interaction clearly dominates any electromagnetic field perturbations generated by ionospheric mass-loading (e.g., Zimmer et al. (2000); Liuzzo et al. (2015)). At intermediate distances between Callisto and the center of the magnetospheric current sheet, the electromagnetic field perturbations near the moon are generated by a non-linear coupling of the ionosphere-magnetosphere and dipole-magnetosphere interactions (Liuzzo et al., 2016).

Hence, regarding energetic ion dynamics near Callisto, several important questions are yet to be addressed:

- To what extent do the contributions of the dipole-magnetosphere interaction and the ionosphere-magnetosphere interaction (in isolation *and* in combination) affect the dynamics of energetic ions near Callisto?
- How strongly do the local electromagnetic field perturbations influence the accessibility of Callisto to energetic ions?
- To what degree do the energetic ion fluxes measured in the ambient plasma outside of Callisto's interaction region differ from the fluxes onto the top of the moon's atmosphere?

Titan's interaction with the thermal plasma of Saturn's magnetosphere significantly affects energetic ion dynamics (Regoli et al., 2016). Because of the strong parallels with Callisto's interaction, it is expected that Callisto's perturbed electromagnetic environment may also drastically modify energetic ion dynamics. Consequently, any reasonable model of energetic ion dynamics near Callisto must include the local electromagnetic perturbations generated by its plasma interaction. In our study, this will be accomplished by using the electromagnetic field output from the *Adaptive Ion-Kinetic, Electron-Fluid* (AIKEF, Müller et al. (2011)) hybrid model.

Our study is structured as follows: Section 2 will briefly describe the hybrid model used to calculate the local electric and magnetic field perturbations near Callisto. This section will also introduce the test particle model that will be used throughout the study. Section 3.1 briefly discusses the perturbations from four different electromagnetic field configurations that represent the various thermal plasma interaction scenarios that occur at Callisto throughout a full synodic rotation. Then, Sections 3.2–3.5 present maps that display accessibility of Callisto to energetic protons for these four interaction scenarios, whereas the dynamics and accessibility maps of energetic oxygen and sulfur ions are presented in Appendices A–D. Our findings are applied in Section 4 to generate maps displaying accessibility of Callisto to energetic H^+ ions during three Galileo flybys (C3, C9, and C10). Section 5 presents a comparison between the energetic ion precipitation patterns from the four scenarios of Callisto's plasma interaction, and discusses the intensity of energetic ion flux onto Callisto after taking into account the reduction caused by the moon's plasma interaction. Conclusions of the study, as well as outlook to the upcoming *JUpiter ICy moons Explorer* (JUICE) mission, are presented in Section 6.

This study focuses only on energetic *ion* dynamics near Callisto. Modeling and understanding of energetic *electron* dynamics near the moon will be the subject of a future publication.

2. Modeling energetic ion dynamics near Callisto

Callisto's interaction with the thermal plasma population of Jupiter's magnetosphere shapes the electromagnetic perturbations near the moon. These perturbations are obtained from the AIKEF hybrid model (Müller et al., 2011), which is briefly described in Section 2.1. The maximum time step possible in the hybrid model is constrained by the Courant-Friedrichs-Lewy (CFL) condition. For the thermal, nearly corotating plasma with a velocity of $u_0 = 192$ km/s, the time step required for the AIKEF model to satisfy this condition allows the simulations to finish in a computing time on the order of a week when using approximately 256 cores on a supercomputer. However, energetic protons with energies of $E = 1$ MeV, for example, already have a velocity of $v = \sqrt{\frac{2E}{m}} \approx 10^4$ km/s, which is nearly two orders of magnitude larger than the bulk velocity of the thermal plasma u_0. As a result, the time step required for the hybrid model to satisfy the CFL condition would *decrease* by two orders of magnitude (e.g., Kabanovic et al. (2018)). Inclusion of the energetic particle population into the hybrid simulation would therefore increase the simulation run time well beyond feasibility. However, due to the test particle nature of the energetic ions, this can be overcome by studying energetic ion dynamics using a stand-alone model that injects these ions into the *stationary* electromagnetic field configuration from the hybrid model. This test particle model is introduced in Section 2.2.

2.1. Hybrid simulations of Callisto's electromagnetic environment

The AIKEF hybrid model solves the Newtonian equations of motion for individual ion "macroparticles" which have the same charge-to-mass ratio as real ions. A kinetic representation of the thermal ion population near Callisto is necessary, as the gyroradii of the magnetospheric and ionospheric ions can be up to 10 times the size of the moon (e.g., Kivelson et al. (2004); Liuzzo et al. (2015)). In the hybrid model, electrons are treated as a massless, charge-neutralizing fluid. Callisto's atmosphere, mainly consisting of O_2 with a minor CO_2 component, is represented using barometric laws for the altitudinal dependence of the number densities with a superimposed ramside/wakeside asymmetry. This

representation is consistent with all available observations of Callisto's atmosphere, and detailed discussion is presented in Liuzzo et al. (2015). The modeled atmosphere is ionized by a combination of solar ultraviolet radiation and electron impacts. For further discussion of the atmosphere and ionosphere models, and a detailed listing of the parameters used, the reader is referred to Section 2.3 of Liuzzo et al. (2015).

The time scales associated with Callisto's thermal plasma interaction are much shorter than the time scales associated with induction at the moon (Seufert et al., 2011). Therefore, it is possible to represent Callisto's induced magnetic field as a static magnetic moment $\mathbf{M}_{ind}$ within the center of the moon. Further details on the calculation of $\mathbf{M}_{ind}$ can be found in Appendix A of Liuzzo et al. (2015) and Section 3 of Liuzzo et al. (2016). AIKEF uses the Callisto-centered, Cartesian, CphiO coordinate system in which unit vector $\hat{\mathbf{x}}$ aligns with the direction of corotation, unit vector $\hat{\mathbf{y}}$ points toward Jupiter, and unit vector $\hat{\mathbf{z}}$ is aligned with the Jovian spin axis, completing the right-handed set.

The standard West Longitude system is used to define longitude on Callisto's surface (e.g., Dessler (1983)). In this system, 0° W longitude is aligned with the y-axis of the CphiO coordinate system (i.e., in Callisto's equatorial plane it is located at $x = 0R_C, y = 1R_C$). Longitude increases in a *clockwise* manner, such that 90° W faces downstream of the plasma flow in Callisto's leading hemisphere (located at $x = 1R_C, y = 0R_C$ in the moon's equatorial plane), 180° W longitude is the point antipodal to 0° W and is located in the Jupiter-averted hemisphere, and 270° W is located in Callisto's trailing (ramside) hemisphere (in the moon's equatorial plane, this longitude occurs at $x = -1R_C, y = 0R_C$). In latitude, 90° N coincides with the location of Callisto's geographic north pole (at $x = 0R_C, y = 0R_C, z = 1R_C$) and 90° S is positioned at the moon's geographic South pole (at $z = -1R_C$).

The AIKEF model has recently been used to investigate the plasma interactions of many small solar system bodies, including Titan (e.g., Feyerabend et al. (2015)), Pluto (e.g., Feyerabend et al. (2017)) and Mercury (e.g., Exner et al. (2018)). At Callisto, the AIKEF model has already been applied to extensively study the moon's interaction with Jupiter's magnetosphere. Liuzzo et al. (2015) investigated the interaction of Callisto's ionosphere with the thermal magnetospheric plasma, and found that the magnitude of the associated magnetic field perturbations can be of the same order as the background magnetospheric field. Subsequently, Liuzzo et al. (2016) disentangled the signatures of Callisto's ionosphere-magnetosphere interaction from those of its dipole-magnetosphere interaction, thereby explaining plasma and magnetic field measurements obtained during the wakeside Galileo C10 flyby of the moon. In a follow-up study, Liuzzo et al. (2017) investigated magnetic field measurements from the Galileo C21, C22, C23, and C30 flybys of Callisto, and determined that no signatures of the moon's induced dipole were detected during these encounters. These three studies provide a comprehensive analysis of the electromagnetic field perturbations generated by Callisto's thermal plasma interaction and associated observations from the Galileo era. For detailed explanations of the model features, the reader is therefore referred to our previous studies.

Furthermore, the electromagnetic field output from AIKEF simulations has been used to investigate energetic ion dynamics at various moons of Saturn (Roussos et al., 2012; Krupp et al., 2013; Kotova et al., 2015; Regoli et al., 2016). In analogy to these studies in the Saturnian system, we will use output from the AIKEF hybrid model to investigate the sensitivity of energetic ion dynamics on Callisto's interaction with the thermal plasma population. Four scenarios of Callisto's electromagnetic interaction will be studied (see Table 1), each of which represents the stationary electromagnetic environment near Callisto at a snapshot in time as Jupiter's magnetospheric current sheet sweeps over the moon:

1. The first scenario (Run #1 in Table 1) is used to determine the "baseline" behavior of energetic particles near Callisto. Scenario #1 uses the superposition of Callisto's induced dipolar field with the Jovian magnetospheric background field at the moon's orbit when

Table 1

Parameters of the four scenarios examined in this study. The calculation of the induced magnetic moment ($\mathbf{M}_{ind}$) assumes that Callisto's interior is perfectly conducting, and the value is consistent with other studies (e.g., Zimmer et al. (2000); Liuzzo et al. (2015, 2016)). The magnetospheric background field ($\mathbf{B}_0$), bulk velocity ($\mathbf{u}_0$), ion mass (m_0), and number density (n_0), as well as the plasma beta (β) and the Mach numbers (Alfvénic M_A, magnetosonic M_{MS}, and sonic M_S) are within the range of values found near the orbit of Callisto (e.g., Kivelson et al. (2004)).

	Run#1	Run#2	Run#3	Run#4
Plasma interaction?	No	Yes	Yes	Yes
Ionosphere?	No	No	Yes	Yes
Induced dipole?	Yes	Yes	No	Yes
$\mathbf{M}_{ind}$ ($\cdot 10^{18}$ Am^2)	$+ 2.35\hat{\mathbf{y}}$	$+ 2.35\hat{\mathbf{y}}$	N/A	$+ 2.35\hat{\mathbf{y}}$
$\mathbf{B}_0$ (nT)	$- 33.58\hat{\mathbf{y}}$	$- 33.58\hat{\mathbf{y}}$	$- 33.58\hat{\mathbf{y}}$	$- 33.58\hat{\mathbf{y}}$
$\mathbf{u}_0$ (km/s)	$+ 192\hat{\mathbf{x}}$	$+ 192\hat{\mathbf{x}}$	$+ 192\hat{\mathbf{x}}$	$+ 192\hat{\mathbf{x}}$
$\mathbf{E}_0 = \mathbf{u}_0 \times \mathbf{B}_0$ (mV/m)	$+ 6.4\hat{\mathbf{z}}$	$+ 6.4\hat{\mathbf{z}}$	$+ 6.4\hat{\mathbf{z}}$	$+ 6.4\hat{\mathbf{z}}$
m_0 (amu)	N/A	16 (O$^+$)	16 (O$^+$)	16 (O$^+$)
n_0 (cm^{-3})	N/A	0.58	0.58	0.58
β	N/A	0.53	0.53	0.53
M_A	N/A	0.8	0.8	0.8
M_{MS}	N/A	0.6	0.6	0.6
M_S	N/A	1.1	1.1	1.1
AIKEF domain (R_C)	N/A	$- 15 \leq x, y, z \leq 15$	$- 15 \leq x, y, z \leq 15$	$- 15 \leq x, y, z \leq 15$
Max. AIKEF resolution (R_C)	N/A	0.05	0.05	0.05

Callisto is located at large distances to Jupiter's magnetospheric current sheet (e.g., Kivelson et al. (1999); Zimmer et al. (2000)). This scenario does not consider any electromagnetic perturbations associated with Callisto's plasma interaction, and therefore the undisturbed convective electric field ($\mathbf{E}_0 = - \mathbf{u}_0 \times \mathbf{B}$, where $\mathbf{B}$ is the superposition of the magnetospheric background field and the induced dipole field) is used. Hence, scenario #1 is the only setup where electromagnetic field output from the hybrid model is not required as the fields can be determined analytically. This scenario reflects the conditions near Callisto when located at large distances to the center of the Jovian current sheet.

2. The second scenario investigated (denoted Run #2 in Table 1) also corresponds to Callisto being located far from the center of Jupiter's magnetospheric current sheet. However, compared to the "baseline" fields of Run #1, Run #2 is representative of a stronger interaction between the magnetospheric plasma and Callisto's induced dipole. At large distances to the center of the current sheet, the electromagnetic perturbations near Callisto are primarily generated by the moon's dipole-magnetosphere interaction (Liuzzo et al., 2015). Run #2 therefore only includes Callisto's induced magnetic field and its plasma interaction with the corotational upstream plasma, but does not include any currents generated by mass-loading from the ionosphere. This scenario is similar to the setup used by Liuzzo et al. (2015) to reproduce the magnetic field perturbations observed during the Galileo C3 and C9 flybys of Callisto (see Appendix A in that work).

3. The third scenario considered for the electromagnetic fields near Callisto (Run #3) corresponds to those System III longitudes where the moon is located near the center of the Jovian current sheet. In this scenario Callisto's induced dipole nearly vanishes, and the moon's ionosphere-magnetosphere interaction dominates the local electromagnetic perturbations. Therefore, Run #3 includes only the electromagnetic perturbations generated by mass-loading from Callisto's ionosphere. This scenario is similar to the cases studied in Sections 3.1 and 3.2 of Liuzzo et al. (2015).

4. Finally, for intermediate distances between Callisto and the center of Jupiter's magnetospheric current sheet, the electromagnetic field perturbations near the moon are generated by a non-linear coupling

of the ionosphere-magnetosphere and dipole-magnetosphere interactions. This scenario is represented by Run #4 in Table 1, and includes contributions from Callisto's induced dipole field *and* mass-loading from its ionosphere. The setup of Run #4 is analogous to the conditions near Callisto during, for example, the Galileo C10 and C21 flybys studied by Liuzzo et al. (2016, 2017).

The four scenarios presented in the first part of this study use identical parameters of the upstream magnetospheric plasma. This is by design in order to facilitate a straightforward comparison between the test particle simulations, and allows us to attribute all changes in energetic ion dynamics to the modified properties Callisto to the upstream flow. Moreover, the four scenarios presented in Table 1 assume that the magnetospheric background field is anti-aligned with the *y*-axis. Although the assumed magnetospheric field orientation is an "idealized" setup, it ensures that any unexpected asymmetries in the dynamics of energetic ions are a result of Callisto's plasma interaction, and *not* a result of an "oblique" orientation of the upstream field. The upstream magnetic field orientation is also chosen such that Callisto's induced magnetic moment exactly cancels the background field on the moon's surface at the two "magnetic poles," see Liuzzo et al. (2016). The electromagnetic perturbations associated with each of the four scenarios are briefly discussed in Section 3.1, while energetic ion dynamics during these scenarios are discussed in Sections 3.2 through 3.5.

We note that, for Callisto's induced dipole to be absent, the time-varying component of the Jovian magnetospheric background field must vanish. This occurs when Callisto is located close to the center of Jupiter's magnetospheric current sheet, where the background field is aligned mainly along $-\hat{\mathbf{z}}$. Run #3 does not include contributions to Callisto's electromagnetic environment from its induced dipole, and therefore assumes that Callisto is embedded within this current sheet. However, to facilitate the comparison between the dynamics of energetic ions from the different runs, we do *not* rotate the orientation of the magnetospheric background field in Run #3 such that it is aligned with $-\hat{\mathbf{z}}$; i.e., the background field remains oriented along $-\hat{\mathbf{y}}$ as in the other runs. Aligning the magnetospheric background field with $-\hat{\mathbf{z}}$ would only rotate the electromagnetic field output around the *x*-axis by 90°.

These four idealized scenarios form the basis of our subsequent investigation of energetic particle dynamics near Callisto for the upstream conditions of the C3, C9, and C10 Galileo flybys (see Section 4). Callisto's thermal plasma interaction at the time of these flybys has been previously analyzed by Liuzzo et al. (2015, 2016). For this investigation, the upstream conditions measured by Galileo at the respective distance to the Jovian current sheet are used as input into the hybrid model, as documented in our aforementioned studies. During these flybys, the ambient magnetospheric field $\mathbf{B}_0$ mainly pointed in the $\pm\hat{\mathbf{y}}$ direction, but the non-zero $B_{x,0}$ and $B_{z,0}$ components of the background field made weak contributions to the observed plasma interaction signatures as well. Energetic proton dynamics during these flybys are presented in Section 4, while the upstream parameters for C3, C9, and C10 are documented in our aforementioned publications.

2.2. Test particle simulations of energetic ion dynamics

The dynamics of charged particles with mass m and charge q embedded in an electric field $\mathbf{E}$ and a magnetic field $\mathbf{B}$ are governed by the Lorentz force,

$$m\frac{\mathrm{d}(\gamma\mathbf{v})}{\mathrm{d}t} = q(\mathbf{E} + \mathbf{v}\times\mathbf{B}) \quad , \tag{1}$$

with the Lorentz factor γ. For all ions studied (with initial energies from $E = 10$ keV to $E = 5000$ keV), the value of γ has been continuously monitored during tracing and the Lorentz factor always remained at a value of $\gamma \approx 1$. For the most energetic protons traced with $E = 5000$ keV, γ still remained below a value of 1.01. Treating the energetic ion

population as non-relativistic is therefore valid for the energy regime studied here. Under these conditions, the non-relativistic equation of motion reads:

$$m\frac{\mathrm{d}\mathbf{v}}{\mathrm{d}t} = q(\mathbf{E} + \mathbf{v}\times\mathbf{B}) \quad . \tag{2}$$

This set of ordinary differential equations is solved using a fourth-order Runge-Kutta integration routine.

For an energetic ion with position $\mathbf{r} = [x, y, z]$ located inside the domain of the AIKEF simulation (within $-15R_C \leq x, y, z \leq 15R_C$, see Table 1), the local electric and magnetic fields required to solve equation (2) are extracted from the hybrid model (see discussion in Section 2.1). Once the ion leaves the domain of the AIKEF simulation, the electric and magnetic fields acting on it are treated as constant, and are set to the undisturbed upstream values of the respective hybrid run (see Table 1), in analogy to the approach of Regoli et al. (2016) and Kabanovic et al. (2018) for Titan. This method assumes that the half-bounce time of an ion $\frac{1}{2}\tau_b$ (i.e., the time it takes a mirroring particle to travel from Callisto's orbital plane to its mirror point and back) is longer than the time scale of the azimuthal plasma motion through Callisto's interaction region. Therefore, this method is valid only if, once an ion exits the moon's interaction region, it returns to Callisto's orbital plane multiple moon radii downstream where the locally perturbed electromagnetic fields have returned to their undisturbed background values and the ion can no longer impinge onto Callisto. Otherwise, a full description of the ion's bounce motion (which starts in Jupiter's equatorial plane near Callisto, travels to its mirror point, and subsequently returns to Jupiter's equatorial plane at the orbital distance of the moon) would have to be included in the particle tracing simulations.

To determine if this approximation is valid for energetic ions near Callisto's orbit, we calculate their equatorial displacement r_{eq} after a half-bounce as well as their gyroradii r_g. The equatorial displacement along the moon's orbital path (r_{eq}), is defined as the distance at which an energetic ion (launched near Callisto) can be found downstream of the moon after completing a half-bounce and returning to the moon's orbital plane. This displacement is calculated by $r_{eq} = \frac{1}{2}\tau_b v_d$, where τ_b is the particle's bounce time (see, e.g., Thomsen and Van Allen (1980)) and v_d is the bounce-averaged azimuthal drift velocity of the energetic ion relative to Callisto. This ion drift velocity v_d contains the contributions from the corotation ($\mathbf{E}\times\mathbf{B}$), gradient, and curvature drifts, and points along the $+\hat{\mathbf{x}}$ direction. Thus, if the value $\Delta = r_{eq} - r_g$ is large compared to the length of Callisto's wakeside interaction region, our approach is valid. Fig. 1 shows the values of r_{eq} and r_g as a function of energy for the three predominant energetic ion species near Callisto's orbit: hydrogen, oxygen, and sulfur (Mauk et al., 2004).

For this study, we focus on H^+, O^{2+}, and S^{3+} ions. Using these multiply-charged states for oxygen and sulfur is consistent with observations of energetic heavy ions in Jupiter's middle magnetosphere by the Voyager and Ulysses spacecrafts (Hamilton et al., 1981; Geiss et al., 1992; Collier and Hamilton, 1995; Keppler and Krupp, 1996). These data sets suggest that, near the orbit of Callisto, the energetic heavy ion population is mainly comprised of O^{2+} and S^{3+}. This approach is also consistent with the work of Cooper et al. (2001), Cassidy et al. (2013), and Fatemi et al. (2016) who used charge states of 2+ and 3+ for energetic oxygen and sulfur, respectively, in their studies of energetic ion dynamics near the icy Galilean moons. However, there is still an ongoing debate regarding the charge state of heavy ion species, such as oxygen and sulfur, in Jupiter's inner magnetosphere (e.g., Bagenal et al. (2015)).

Values of ion equatorial displacement (r_{eq}), gyroradius (r_g), the quantity Δ, half-bounce time ($\frac{1}{2}\tau_b$), as well as the corkscrew energy (E_{gr}, the energy where the particle's gyroradius is equal to Callisto's radius) are provided in Table 2 for H^+, O^{2+}, and S^{3+} at select energies. The equatorial displacement increases non-monotonically with energy for each of the species studied here. For an O^{2+} ion, the lowest value of its equatorial
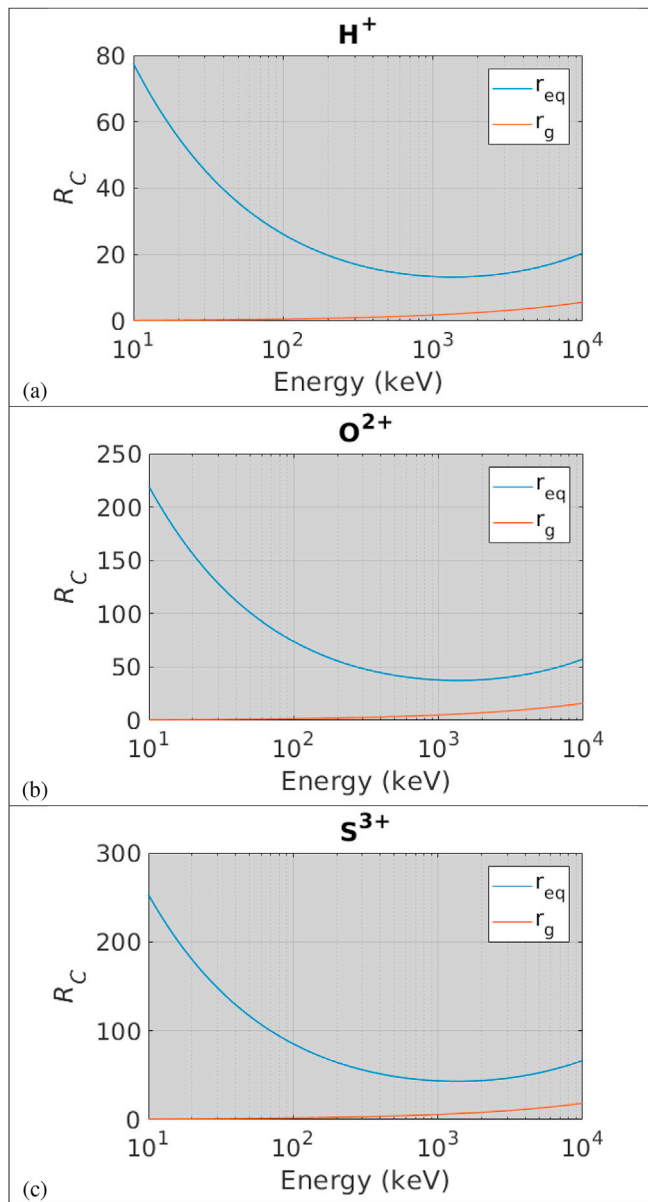
Fig. 1. Equatorial displacement (r_{eq}, blue) after a half-bounce period $\frac{1}{2}\tau_b$ and particle gyroradius (r_g, orange) for (a) H$^+$, (b) O^{2+}, and (c) S^{3+} ions near Callisto's orbit with a pitch angle near $\alpha = 90°$ as a function of energy. Note the difference in scale along the vertical axis. (For interpretation of the references to color in this figure legend, the reader is referred to the Web version of this article.)

displacement after a half-bounce period occurs for an energy of $E \approx 2$ MeV (see Fig. 1(b)). Such an ion has an azimuthal drift velocity of $v_d = 234$ km/s, using a 50% reduction in the azimuthal bulk velocity of the corotating magnetospheric plasma to $u_0 = 100$ km/s, which is a reasonable estimate for the wake region of Callisto (Liuzzo et al., 2015). As a result, the equatorial displacement of a doubly-charged 2 MeV oxygen ion is $r_{eq} = 38R_C$, with a corresponding gyroradius of only $r_g = 7.1R_C$. The difference by approximately a factor of 5 between r_{eq} and r_g means that this ion returns to Callisto's orbital plane at a distance of $\Delta = 31R_C$ downstream of the moon. At this distance, the electromagnetic fields are no longer perturbed by Callisto's interaction with the thermal magnetospheric plasma, and have returned to their background values. Thus, the ion can *not* be deflected back toward Callisto and impact the moon.

As also visible in Fig. 1 and Table 2, the lowest equatorial

displacement for the three ion species studied occurs for protons. Fig. 1(a) shows that the value of r_{eq} is minimized for an H$^+$ ion with an energy of $E \approx 2$ MeV, with $r_{eq} \approx 13R_C$ more than 5 times larger than $r_g = 2.5R_C$. However, even for an H$^+$ ion with this energy, the difference between r_{eq} and r_g of $\Delta = 11R_C$ is still large enough to place bouncing protons far downstream of Callisto's interaction region. Compared to H$^+$ and O^{2+} ions, S^{3+} ions similarly return to Callisto's orbital plane with r_{eq} approximately 5 times larger than r_g, but at distances $\Delta > 35R_C$; i.e., even farther downstream of Callisto for all energies than the other two species (see Fig. 1(c)). Therefore, for each of the energetic species within the range of energies considered in this study, a mirroring ion is unable to re-encounter the perturbed electromagnetic fields near Callisto after completing a half-bounce, as it returns too far downstream of the moon. Our approach of treating the electromagnetic fields as uniform outside of the AIKEF hybrid simulation is therefore valid, as was also found to be the case for energetic ions near Titan (Regoli et al., 2016; Kabanovic et al., 2018).

The numerical solution of equation (2) can be obtained in two different ways. Integrating equation (2) forward in time is useful for examining the evolution of a given upstream particle distribution. However, this approach would be very expensive from the computational standpoint. Such a "forward integration" approach would initialize particles upstream of Callisto, and their motion may result in some of them impinging onto the moon. In order to create a reliable, statistical representation of impact maps and accessibility patterns of the moon to energetic particles, each individual simulation would have to solve for the evolution of billions of energetic test particles, as only a small fraction of the initial particle population may actually come close to the moon (e.g., Wulms et al. (2010); Kabanovic et al. (2018)). The starting grid from which these particles are launched would necessarily extend multiple Callisto radii in each direction perpendicular to the upstream flow simply to ensure that there would be enough particles that actually hit the moon. The large fraction of initialized particles that miss the moon would not contribute *at all* to the impact maps of energetic particles. Therefore, for our study where we aim to constrain accessibility of Callisto to energetic particles, this forward integration approach would be an uneconomic use of computational resources.

For these reasons, we have chosen to integrate the equation of motion for energetic ions *backward* in time (i.e., solving equation (2) using a *negative* time step). This "backtracing" technique has already been extensively applied to study energetic particle dynamics near Ganymede and Europa (e.g., Cooper et al. (2001); Cassidy et al. (2013); Dalton et al. (2013)) as well as near Rhea, Dione, and Titan (e.g., Kotova et al. (2015); Regoli et al. (2016)). For our study, ions are injected near the surface of Callisto and their motion is integrated backward in time.

Callisto's atmospheric scale height is approximately 23 km; i.e., it is less than 1% of the moon's radius (e.g., Carlson (1999)). However, achieving a grid resolution on the order of $0.01R_C$ in the hybrid model is not feasible. Even with multiple levels of refinement of the simulation

Table 2

Half bounce period ($\frac{1}{2}\tau_b$), equatorial displacement (r_{eq}), equatorial gyroradius (r_g), and the difference $\Delta = r_{eq} - r_g$ for ions at select energies E with equatorial pitch angles of $\alpha \approx 90°$ in Jupiter's dipole field at Callisto's orbit. The corkscrew energies E_{gr} for H$^+$, O^{2+}, and S^{3+} ions are also given. See text for further details.

Species	E (keV)	$\frac{1}{2}\tau_b$ (s)	$r_{eq}(R_C)$	$r_g(R_C)$	$\Delta(R_C)$	E_{gr} (keV)
H$^+$	10	2016	78	0.2	77.8	314
H$^+$	100	637	26	0.6	25.4	314
H$^+$	1000	64	20	5.6	14.4	314
O^{2+}	10	5701	219	0.5	218.5	79
O^{2+}	100	1803	74	1.6	72.4	79
O^{2+}	1000	180	58	16.0	42.0	79
S^{3+}	10	6583	253	0.6	252.4	88
S^{3+}	100	2082	85	1.8	83.2	88
S^{3+}	1000	208	67	18.4	48.6	88

grid, AIKEF must also simultaneously resolve the large-scale features of Callisto's plasma interaction that extend to distances of more than $10R_C$ from the moon (e.g., Liuzzo et al. (2016)). To resolve the vastly different scales of Callisto's plasma interaction and atmospheric scale height within the same simulation, all available models of Callisto's thermal plasma interaction use an artificially inflated atmosphere with the scale height increased by a factor of 10 and the surface density of the neutral gas reduced by the same factor (e.g., Seufert (2012); Liuzzo et al. (2015)). Using this approach, magnetic field and plasma densities from the AIKEF model are in quantitative agreement with Callisto flyby data from the Galileo mission, most of which was obtained well above an altitude of $230\,km \approx 0.1R_C$.

The reader should recognize that below these altitudes, the electromagnetic field output of the hybrid model—and therefore the dynamics of energetic particles—can not be represented by our model in a quantitatively realistic way. Therefore, we inject energetic ions onto a sphere with a radius of $\tilde{R}_C = 1.1R_C$. Studying energetic particle dynamics in the immediate vicinity of Callisto's surface is beyond the scope of this paper, as it requires a more accurate representation of the electromagnetic fields near the moon's surface. However, we note that simulations were performed with the present model where the energetic ions were injected on a sphere of radius $1R_C$ (i.e., at Callisto's surface), and resulted in only very minor quantitative differences to the accessibility patterns presented here.

Each model run presented in Sections 3.2 through 3.5 uses one of the four electromagnetic field configurations described in Section 2.1 and Table 1, for a prescribed, mono-energetic ion population. Performing multiple runs that each include a mono-energetic ion population allows us to investigate the energy-dependence of particle accessibility at Callisto. For each run, over 65 million ions are inserted on a spherical starting grid placed around Callisto. The starting points of these energetic ions are separated in position space by 2° in latitude and 4° in longitude. At each of these 8100 points on the spherical starting grid, individual, non-relativistic ions of a given energy E and velocity $v = \sqrt{\frac{2E}{m}}$ are launched at distinct starting angles with respect to the local zenith direction. The resolution in velocity space (i.e., the difference between the initial propagation directions of two neighboring ions) is characterized by 2° steps measured from local zenith and 4° in the azimuth direction yielding 8100 ions launched at each point, for a total of 8100^2 ions per each run of the particle tracing model.

After an ion is initialized in the simulation and begins to move through Callisto's perturbed electromagnetic field environment, it can encounter one of two fates. The first fate that can befall an ion is that it impacts Callisto. In this case, the trajectory of the ion is denoted "forbidden." In a forward integration approach, such an ion would be required to travel *through* the solid body of Callisto in order to reach its starting point on the spherical grid. A "forbidden" particle therefore can *not* contribute to the energetic particle bombardment of Callisto at its starting point.

The second fate of an ion in our backtracing approach is that it never penetrates the sphere of radius $\tilde{R}_C$; i.e., during the entire simulation, the particle position fulfills $|\mathbf{r}| > \tilde{R}_C$. In this case, without an additional boundary condition, the particle tracer would continue updating the position and velocity of the ion indefinitely. Therefore, an ion is considered "escaped" from Callisto's local interaction region after it fulfills two additional criteria (adapted from Regoli et al. (2016) for energetic ion dynamics near Titan). First, the ion must exit the AIKEF simulation domain and enter the realm of uniform electromagnetic fields outside of this box. As soon as the ion has left the AIKEF domain for the first time, it must subsequently complete two full gyration cycles without impacting the spherical starting grid. After fulfilling these additional criteria, the ion is considered "escaped." We have verified that an increase of the escape condition to more than two complete gyration cycles does *not* affect the resulting precipitation maps. In a forward integration approach, an "escaped" ion would be able to access its starting position

and is therefore able to contribute to energetic particle bombardment of Callisto.

In future studies, the combination of a backtracing tool for energetic particles with the electromagnetic field output of the AIKEF simulation will be applied to study energetic electron dynamics near Callisto, as well as energetic particles near the other Galilean moons. This combined simulation suite has been named the *Galilean Energetics Tracing Model* (GENTOo).

3. Accessibility of Callisto to energetic ions

Before analyzing energetic ion dynamics, a brief discussion of the local electromagnetic field perturbations near Callisto is presented in Section 3.1. A more exhaustive discussion of Callisto's electromagnetic environment can be found in Liuzzo et al. (2015, 2016, 2017). Dynamics of energetic H$^+$ions for the four scenarios (see Table 1) are discussed in Sections 3.2 through 3.5, whereas the dynamics of O^{2+} and S^{3+} ions are presented in Appendices A–D.

3.1. Callisto's electromagnetic field environment

The perturbed magnetic fields from the four scenarios investigated in this study (see Table 1) are shown in Fig. 2. In the first column of Fig. 2 (panels 2(a)–2(d)), the B_x component of the magnetic field in the $z = 0$ plane is shown for each scenario. This plane contains the background magnetic field ($\mathbf{B}_0$) and bulk velocity ($\mathbf{u}_0$) vectors. The second and third columns of Fig. 2 show the magnitude of the magnetic field $|\mathbf{B}|$ in the $z = 0$ plane (panels 2(e)–2(h)) and the $y = 0$ plane (panels 2(i)–2(l)), respectively.

Callisto's induced dipole is clearly visible in the scenario that considers only the superposition of the induced field with the Jovian background field, but no plasma interaction currents (Run #1, see panels 2(a), 2(e), 2(i)). In Fig. 2(a), the "shamrock leaves" of Callisto's induced dipole are apparent, which correspond to the magnetic field either aligned ($B_x > 0$, red) or anti-aligned ($B_x < 0$, blue) with the corotational flow direction. The moon's induced field exactly cancels the magnetospheric background field at Callisto's "magnetic poles" which are located at $x = 0R_C, y = \pm1R_C, z = 0R_C$ (see Fig. 2(e)). This superposition is also visible in Fig. 2(i), where the magnetic field strength is maximized at Callisto's surface and, in the $y = 0$ plane, falls off symmetrically with a r^{-3} dependence.

The reader is advised that, for a pure dipole in isolation (i.e., without the magnetospheric background field), the maximum strength of the magnetic field occurs at the dipole's "magnetic poles," whereas at the "magnetic equator," the field strength is weaker by a factor of 2. However, for the superposition of a dipole field with a spatially homogeneous background field (in which the dipole's magnetic moment is anti-aligned with the direction of the background field), the field strength at the dipole's "magnetic poles" is *minimized*, whereas the field is *maximized* at the "magnetic equator" (see Fig. 2(e)).

Run #2 uses the AIKEF hybrid simulation to obtain the electromagnetic field perturbations near Callisto, depicted in Fig. 2(b), (f), and 2(j). This scenario considers the plasma interaction with Callisto's induced dipole, but does not include the moon's ionosphere. In this case, the plasma interaction gives rise to two Alfvén wings that are inclined against $\mathbf{B}_0$ by approximately 40° (see Fig. 2(b)). The plasma interaction with the induced dipole alone is rather weak: the magnitude of the draped B_x component does not exceed 15% of the background field. The "shamrock leaves" of the induced dipole field are still discernible in Run #2 (see Fig. 2(b)), but the Alfvén wings strongly compress the two "leaves" at Callisto's wakeside (see Liuzzo et al. (2016) for details). This weak plasma interaction is also depicted in Fig. 2(f) and (j), where upstream of Callisto, a slight enhancement in the magnetic field magnitude is seen, corresponding to magnetospheric field lines piled-up against the moon's induced dipole. Due to the plasma interaction, the regions of reduced
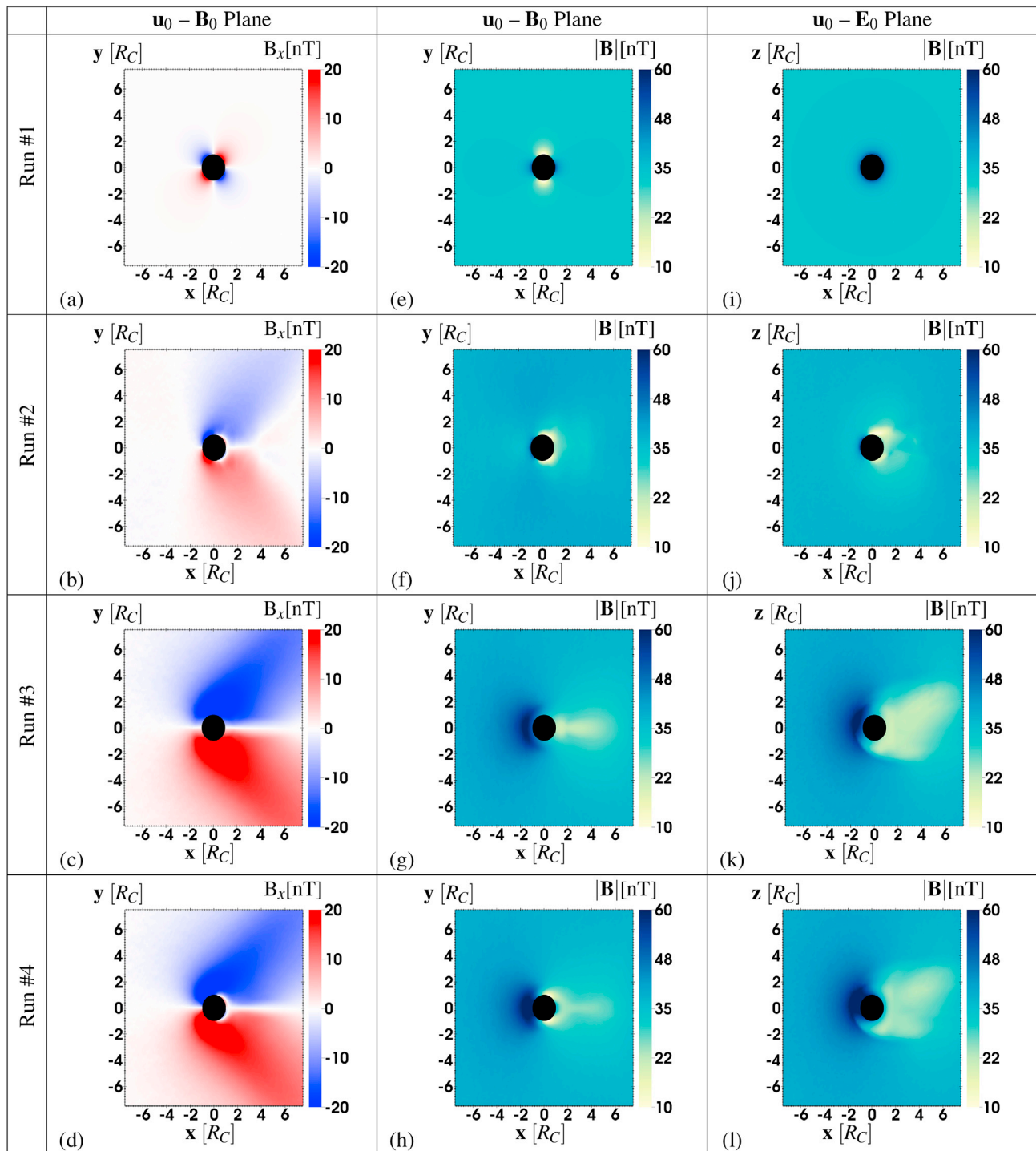
Fig. 2. Magnetic field perturbations associated with the four scenarios described in Table 1: a very weak plasma interaction with Callisto's induced dipole (Run #1), a stronger plasma interaction with the induced dipole (Run #2), the plasma interaction with Callisto's ionosphere alone (Run #3), and the interaction with Callisto's ionosphere *and* induced dipole (Run #4). In the first column (panels (a)–(d)) is the B_x component of the magnetic field in the $\mathbf{u}_0$–$\mathbf{B}_0$ (x–y) plane. The second column (panels (e)–(h)) depicts the magnetic field magnitude $|\mathbf{B}|$ in the $\mathbf{u}_0$–$\mathbf{B}_0$ plane. The third column (panels (i)–(l)) shows $|\mathbf{B}|$ in the $\mathbf{u}_0$–$\mathbf{E}_0$ (x–z) plane.

magnetic field strength above Callisto's "magnetic poles" are slightly stretched toward downstream. Downstream of Callisto and in its $y = 0$ plane (Fig. 2(j)), the magnetic field is also reduced below the value of the background field $|\mathbf{B}_0|$.

The third electromagnetic field scenario studied (Run #3) considers only the magnetospheric interaction with Callisto's ionosphere but no induced dipole. This scenario shows a much stronger plasma interaction

than Run #2. Fig. 2(c) displays a strongly draped magnetic field generating large B_x perturbations in Callisto's Jupiter-facing ($y > 0$) and Jupiter-averted ($y < 0$) hemispheres, with magnitudes of the perturbations approximately 50% of the background field strength. Compared to Run #2 with Callisto's induced dipole alone (cf. Fig. 2(b)), the moon's ionosphere is able to sustain intense transverse currents that generate much stronger magnetospheric field line draping. In the plane containing

the background magnetic field (i.e., the $z = 0$ plane, see Fig. 2(g)), a symmetric pileup region extends more than $2R_C$ upstream of Callisto and the local magnetic field magnitude exceeds the background field strength by nearly a factor of two. In Callisto's wake, a broad and symmetric decrease in the magnetic field magnitude is formed. This region extends multiple moon radii downstream of Callisto. In the plane perpendicular to $\mathbf{B}_0$ (i.e., the $y = 0$ plane, see Fig. 2(k)), asymmetries associated with the Hall effect and the large ion gyroradii near Callisto are visible. In particular, the magnetic pileup region upstream of Callisto is slightly extended into the moon's north-polar hemisphere ($z > 0$), following the curvature of the moon's pick-up tail (Liuzzo et al., 2015).

The magnetic field perturbations from Run #4 are shown in Fig. 2(d), (h), and 2(l). This run contains the full non-linear coupling of the various features that were present in the previous three scenarios. Strong field line draping is visible in Fig. 2(d) with a similar B_x magnitude as in Run #3 (i.e., approximately $0.5|\mathbf{B}_0|$). In Callisto's wake and in the immediate vicinity of its surface, the quasi-dipolar "core region" is present, extending approximately $0.4R_C$ downstream of the moon. This is visible in Fig. 2(d), where the B_x component in the immediate vicinity of Callisto's wakeside surface is opposite from the orientation of the draped field: the (slightly compressed) $B_x > 0$ region of the dipolar field (red) is still visible in Callisto's $y > 0$ hemisphere and the $B_x < 0$ region (blue) is still visible in Callisto's $y < 0$ hemisphere. Compared to the overall size of Callisto's interaction region, the quasi-dipolar "core region" is small. To better illustrate these features and their role in shaping energetic ion dynamics, a magnified version of this panel is included in Section 3.5 (see Fig. 11). A comprehensive schematic of the quasi-dipolar "core region" is also provided in Fig. 4(a) of Liuzzo et al. (2016).

A similar pileup region as in Run #3 is present upstream of Callisto in Run #4 (see Fig. 2(h)). However, regions of reduced magnetic field are now formed near Callisto's "magnetic poles," corresponding to induced magnetic field lines that "escape" from and "return" to Callisto. These regions of reduced magnetic field strength are stretched slightly toward downstream by the magnetospheric plasma interaction. Fig. 2(l) shows that magnetic field asymmetries in the $y = 0$ plane are also present in Run #4 (caused by the orientation of the pick-up tail in the $y = 0$ plane), while the pileup region extends farther upstream of Callisto than in Run #3.

Fig. 3 depicts the electric field in the $\mathbf{u}_0$–$\mathbf{B}_0$ plane (panels (a)–(d)) and the $\mathbf{u}_0$–$\mathbf{E}_0$ plane (panels (e)–(h)) for the four scenarios used throughout Section 3 (Table 1). Panels 3(a) and 3(e) show the undisturbed, convective electric field ($\mathbf{E}_0 = -\mathbf{u}_0 \times \mathbf{B}$) that is associated with the superposition of Callisto's induced dipole with the magnetospheric background field and a homogeneous plasma bulk velocity $\mathbf{u}_0$ everywhere (Run #1). For Run #2, a slight decrease in the electric field magnitude is visible in Callisto's wake (see Fig. 3(b)), as the weak plasma interaction causes a deflection of the upstream flow around the Alfvén wings. In the $y = 0$ plane for Run #2 (see Fig. 3(f)), a slight electric field enhancement forms near the moon's geometric north and south poles as the incident plasma is accelerated and deflected around the obstacle. The slight north/south asymmetries in the deflection pattern are caused by the non-zero gyroradii of the incident magnetospheric ions (Liuzzo et al., 2015).

The strong plasma interaction during Runs #3 and #4 is clearly visible in the electric field (Fig. 3(c) and (g) for Run #3, and Fig. 3(d) and (h) for Run #4). The interaction generates intense Alfvén wings (see Fig. 2(c) and (d)) which deflect the upstream flow out of the $z = 0$ plane. This causes a strong reduction in the electric field magnitude downstream of the Alfvén wings (see Fig. 3(c) and (d)). In the plane perpendicular to the background magnetic field (the $y = 0$ plane in Fig. 3(g) and (h)), the asymmetric plasma flow pattern around Callisto causes a north/south asymmetry in the electric field magnitude, as the plasma is accelerated more strongly in the moon's southern hemisphere.

3.2. Energetic proton accessibility: very weak plasma interaction (Run #1)

In order to quantitatively compare accessibility of Callisto to energetic ions for various combinations of starting energy and electromagnetic field configuration, we define an energy-dependent, *local* accessibility $\lambda(\tilde{\mathbf{r}}_C, E)$ for each point of the starting sphere:

$$\lambda(\tilde{\mathbf{r}}_C, E) = \frac{N_e(\tilde{\mathbf{r}}_C)}{N_p} \quad . \tag{3}$$

In equation (3), $\tilde{\mathbf{r}}_C$ represents a single grid point on the starting sphere (with radius $|\tilde{\mathbf{r}}_C| = \tilde{R}_C$) from which ions are launched. The quantity N_p is the total number of ions launched from *each* starting grid point $\tilde{\mathbf{r}}_C$ (i.e., $N_p = 8,100$ particles, see Section 2.2), and $N_e(\tilde{\mathbf{r}}_C)$ is the total number of ions that "escape" Callisto from this starting point $\tilde{\mathbf{r}}_C$. This *local* accessibility $\lambda(\tilde{\mathbf{r}}_C, E)$ is the same as studied by Regoli et al. (2016) for Titan, and can range in value from 0% when no ions are able to "escape" Callisto's interaction region (i.e., the trajectory of every ion launched at point $\tilde{\mathbf{r}}_C$ is "forbidden"), up to 100% when every ion "escapes" (i.e., each ion trajectory initialized at $\tilde{\mathbf{r}}_C$ denotes a possible path to access Callisto). At each point $\tilde{\mathbf{r}}_C$, exactly half of the initialized ions *immediately* impact Callisto, as they are launched with a velocity vector that points toward the moon. These ions are *not* included in the calculation of λ; i.e., ions that are considered in equation (3) must survive at least a single time step in GENTOo. If such ions were not filtered out, the maximum local accessibility at any grid point would not exceed a value of $\lambda = 50\%$.

The sum of these *local* accessibilities can be used to define an energy-dependent, *global* (average) accessibility of Callisto to energetic ions:

$$\Lambda(E) = \frac{1}{N_G} \sum_{\tilde{\mathbf{r}}_C} \lambda(\tilde{\mathbf{r}}_C, E) = \frac{1}{N_G N_p} \sum_{\tilde{\mathbf{r}}_C} N_e(\tilde{\mathbf{r}}_C) \quad , \tag{4}$$

where the sum is taken over all nodes of the spherical starting grid. Here, N_G is the *total* number of grid points on the starting sphere from which ions are launched (i.e., $N_G = 8,100$, see Section 2.2). Similar to λ, the *global* (average) energetic ion accessibility $\Lambda(E)$ ranges from 0% to 100%.

Maps of the local accessibility pattern of energetic protons to Callisto are shown in Fig. 4 for select energies and for the electromagnetic field configuration of Run #1. Because the processes governing the dynamics of energetic O^{2+} and S^{3+} ions generate qualitatively similar accessibility patterns as H^+ that are merely shifted to lower energies, maps displaying the accessibility for these two heavier species are discussed in Appendix A. Even though ions with an energy of 1 keV would have been below the threshold detectable by the EPD on board Galileo, results are included for this energy as well in order to illustrate the evolution of energetic ion accessibility of Callisto with increasing energy.

In each panel of Fig. 4, the vertical axis represents the latitude on the starting sphere of radius $\tilde{R}_C$, with 0° located at Callisto's equator, and 90° N and 90° S located at the moon's geographic north and south poles, respectively. The horizontal axis shows West Longitude (increasing from right to left) where, in Callisto's equatorial plane, 0° W longitude (and 360° W longitude) is located at $x = 0$, $y = 1\tilde{R}_C$, 180° W longitude is located at $x = 0$, $y = -1\tilde{R}_C$, and the antipodal longitudes 90° W and 270° W coincide with the apices of Callisto's leading (downstream, at $x = 1\tilde{R}_C$, $y = 0$) and trailing (upstream, at $x = -1\tilde{R}_C$, $y = 0$) hemispheres, respectively. Hence, the left half of each panel in Fig. 4 displays energetic ion accessibility of Callisto's trailing (upstream/ramside) hemisphere, whereas the right half of each panel shows accessibility to the moon's leading (downstream/wakeside) hemisphere.

The local accessibility λ of energetic H^+ ions is depicted in Fig. 4(a)–(e), with the global accessibility Λ for each energy listed at the bottom right corner of its respective panel. For 1 keV H^+ ions, regions of
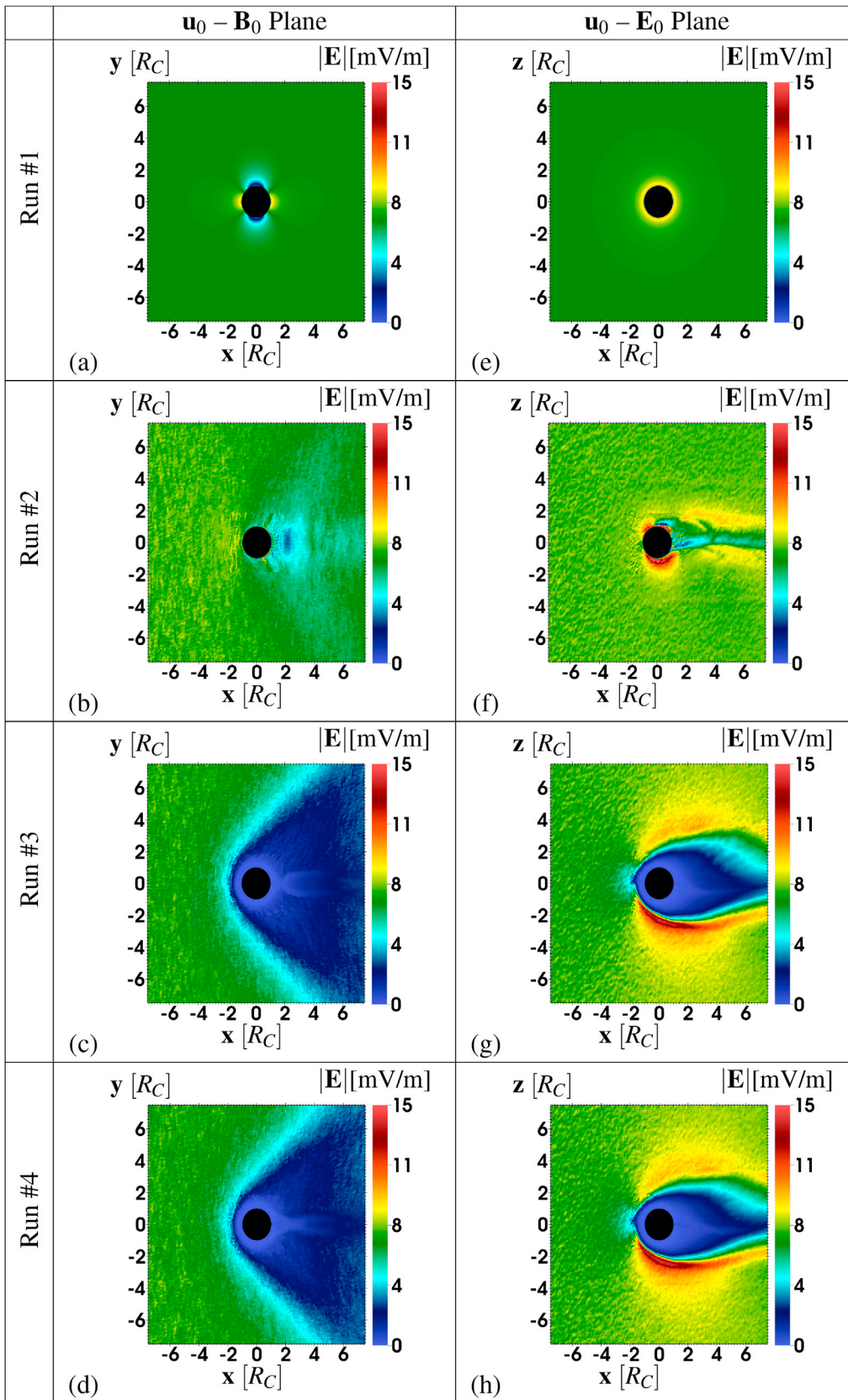
Fig. 3. Local electric field perturbations associated with the four scenarios described in Table 1: a very weak plasma interaction with Callisto's induced dipole (Run #1), a stronger plasma interaction with the induced dipole (Run #2), the plasma interaction with Callisto's ionosphere alone (Run #3), and the interaction with Callisto's ionosphere *and* induced dipole (Run #4). The first column (panels (a)–(d)) shows the magnitude of the electric field $|\mathbf{E}|$ in the $\mathbf{u}_0$–$\mathbf{B}_0$ (*x–y*) plane. The second column (panels (e)–(h)) depicts $|\mathbf{E}|$ in the $\mathbf{u}_0$–$\mathbf{E}_0$ (*x–z*) plane.
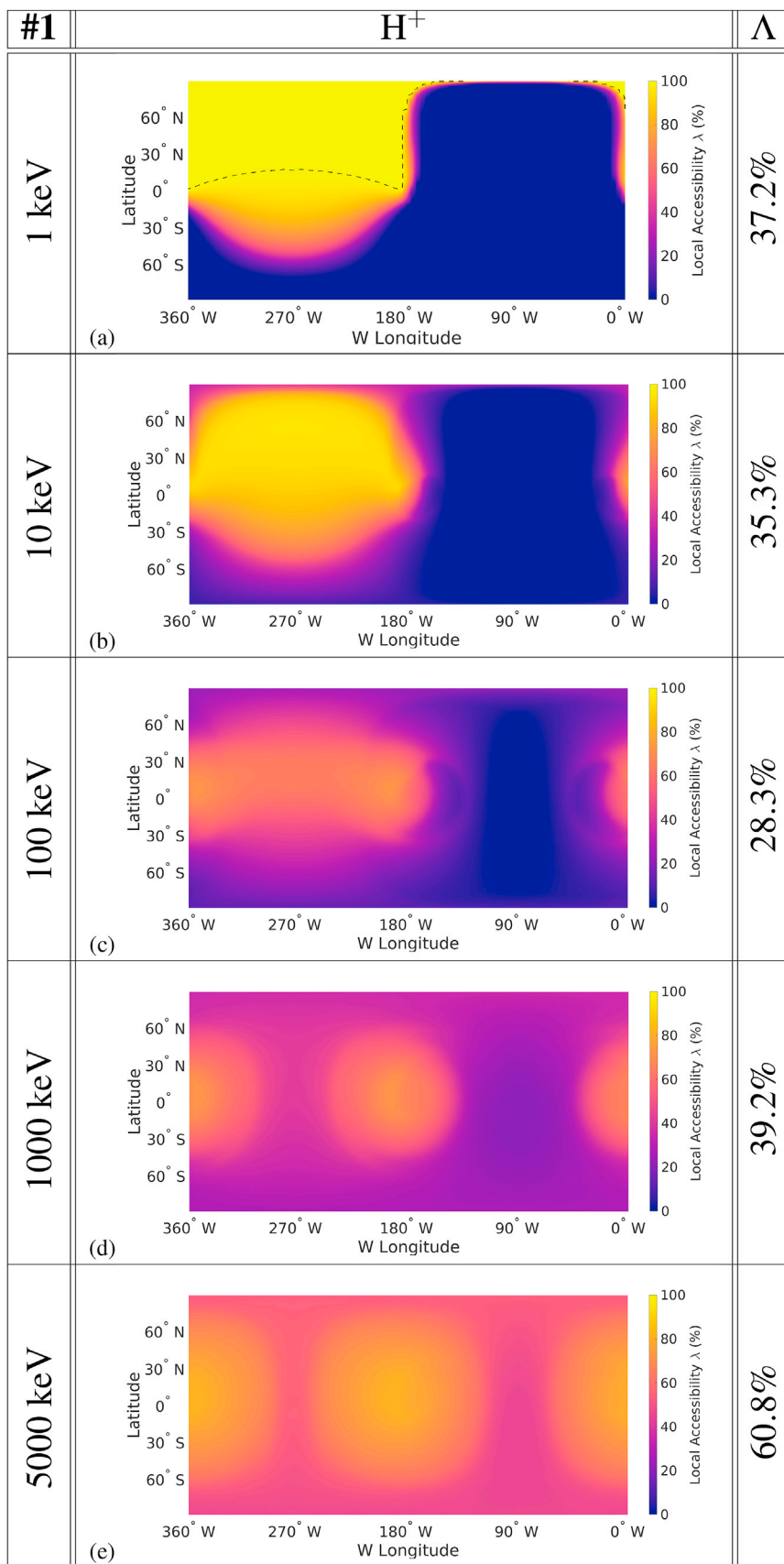
Fig. 4. Energetic proton accessibility of Callisto at select energies for the electromagnetic fields of Run #1, a weak plasma interaction with Callisto's induced dipole (see Table 1), with lowest local accessibility ($\lambda = 0\%$) in blue, and highest local accessibility ($\lambda = 100\%$) in yellow. The dashed line in panel (a) denotes the boundary of the region where $\lambda > 99\%$ accessibility. Additionally, global proton accessibility Λ is listed at the right of each panel. See text for a description of the latitude and longitude convention used. (For interpretation of the references to color in this figure legend, the reader is referred to the Web version of this article.)

high accessibility are mainly confined to Callisto's trailing hemisphere (see panel 4(a)). At longitudes between 0° W and 180° W, nearly no back-traced ions are able to "escape" Callisto; thus, the local accessibility at points in the leading hemisphere is $\lambda(\tilde{\mathbf{r}}_C) \approx 0\%$.

This inaccessibility of the leading hemisphere is a result of "surface shadowing" (Cooper et al., 2001). In the *backtracing* approach, the guiding centers of newly initialized ions move toward upstream with the negative $\mathbf{E} \times \mathbf{B}$ drift velocity, henceforth referred to as the "reverse $\mathbf{E} \times \mathbf{B}$ drift." The gyroradius of a 1 keV proton ($r_g = 0.06 R_C$) is much too small for it to be able to completely gyrate around Callisto. Therefore, the guiding center motion of a 1 keV proton that is initialized in Callisto's leading (wakeside) hemisphere draws the particle directly into the moon before it can escape. As a result, Callisto's leading (wakeside) hemisphere is inaccessible to 1 keV protons that approach the moon from upstream (see Fig. 4(a)). In order to reach Callisto's leading hemisphere, such particles would have to travel through the solid body of the moon. The local accessibility of 1 keV H$^+$ ions is maximized in Callisto's trailing (ramside) hemisphere between longitudes of 180° W and 360° W. Here, back-traced 1 keV ions experience the "reverse $\mathbf{E} \times \mathbf{B}$ drift," travel toward upstream, and escape.

For 1 keV protons launched in Callisto's geographic equatorial plane (0° latitude, $z = 0$), local accessibility starts to display slight, point-like enhancements near 180° W and 360° W longitude, respectively (as visible in bright yellow in Fig. 4(a)). To better guide the eye, the dashed line in panel 4(a) delineates the outer boundary of the region with $\lambda > 99\%$ accessibility. As can be seen, this region descends into Callisto's equatorial plane (0° latitude) near only two longitudes: 180° W and 360° W. These enhancements become even more apparent with increasing proton energy, as shown in Fig. 4(b) through 4(e). These features occur near longitudes that coincide with the "magnetic poles" of the moon's induced magnetic field, as in our setup, the magnetic moment is aligned with the $+y$-axis (see Table 1). As a result of the superposition of Callisto's induced magnetic field and Jupiter's background field (which is aligned with the $-y$-axis in Run #1), the total magnetic field near 180° W and 360° W longitude is drastically reduced, and even vanishes at Callisto's surface (i.e., at $x = 0$, $y = \pm 1 R_C$, e.g., Zimmer et al. (2000)). The gyroradii of ions that are injected near these locations are therefore increased, compared to those of particles launched farther away from the "magnetic poles." This increase allows the protons to avoid impacting Callisto during their gyrations.

Moreover, near these longitudes a strong component of the magnetic field is perpendicular to Callisto's surface. *Back-traced* ions can therefore travel along the nearly perpendicular magnetic field lines before they start gyrating, thereby facilitating escape of ions from these locations. As a result, even when launched slightly downstream of the "magnetic poles" (i.e., at $x > 0$), ions can avoid impacting Callisto by moving along the nearly perpendicular field before gyrating with a locally enhanced r_g. This effect is visible near 0° W longitude, where the local accessibility within a small range of longitudes in Callisto's northern hemisphere is non-zero. Hence, the reduced magnitude of the nearly perpendicular magnetic field creates a "funnel" effect that slightly enhances energetic ion precipitation at low latitudes and near 180° W and 360° W, thereby effectively making Callisto more accessible near the moon's "magnetic poles" to ions of all energies (see Fig. 4).

In addition to these longitudinal asymmetries, the 1 keV H$^+$ accessibility pattern in Fig. 4(a) displays a pronounced north/south asymmetry. In southern latitudes of Callisto's trailing hemisphere (between longitudes 180° W and 360° W), the local accessibility of 1 keV H$^+$ ions falls off rapidly toward Callisto's geographic south pole (see Fig. 4(a)). This is a result of the orientation of the convective electric field which points northward (i.e., along the $+z$-axis). This electric field results in cycloidal trajectories that bring the ions upstream, with cycloidal arcs that are *open* toward Callisto's southern hemisphere; i.e., the maximum z value of the arcs is reached approximately $2 r_g$ *north* of the particles' initial positions.

Therefore, most of the ions that are injected in Callisto's southern hemisphere immediately impact the moon as they gyrate toward the north. In the forward integration approach, these particles would need to gyrate *through* Callisto in order to reach their impact points, and therefore have forbidden trajectories. Only very few particles launched in Callisto's southern hemisphere have initial pitch angles suitable for escape which leads to a small, non-zero accessibility of 1 keV H$^+$ ions in this region.

The same process also causes accessibility of 1 keV protons to be maximized in Callisto's northern hemisphere (see Fig. 4(a)). Compared to their counterparts in the southern hemisphere, energetic H$^+$ ions injected in the moon's northern hemisphere do *not* impact Callisto as they gyrate toward the north, and can escape. As a result, the local accessibility of 1 keV H$^+$ ions is much larger in Callisto's northern hemisphere than in the southern hemisphere, and remains near $\lambda(\tilde{\mathbf{r}}_C) \approx 100\%$ at latitudes between 0° and 90° N.

We remind the reader that the accessibility map in Fig. 4(a) is only a snapshot in time for one specific magnetic field configuration. As the Jovian magnetospheric current sheet sweeps over Callisto, the $B_{y,0}$ component of the magnetospheric background field continuously changes its direction from $B_{y,0} < 0$ to $B_{y,0} > 0$ with a period of approximately 5 h (e.g., Kivelson et al. (1999)). Those regions in Callisto's trailing hemisphere that are partially inaccessible in Run #1 are located near the moon's geographic *south* pole, due to the *northward* sense of gyration of the *back-traced* ions. If the ambient magnetospheric field direction were reversed, these regions would rather be located near Callisto's geographic *north* pole. Therefore, the north/south asymmetry in 1 keV proton accessibility visible in Fig. 4(a) is likely "washed out" over the course of half of a Jovian rotation.

Fig. 4(b) shows the accessibility of Callisto to 10 keV protons for the electromagnetic field configuration of Run #1 (see Table 1). Similar to the 1 keV protons, accessibility at this energy minimizes in Callisto's leading (wakeside) hemisphere, where no back-traced ions are able to escape from the moon. The combination of the "reverse $\mathbf{E} \times \mathbf{B}$ drift" and small gyroradii ($r_g \approx 0.2 R_C$ for a 10 keV proton, see Table 2) immediately drags most ions initialized in the leading hemisphere into the moon's surface.

Regions of high accessibility of 10 keV protons are mainly confined to Callisto's trailing hemisphere (see Fig. 4(b)). In Callisto's equatorial plane, the region accessible to these protons extends slightly farther into the moon's leading hemisphere compared to the case of 1 keV protons. When increasing the starting energy of the protons by a factor of 10, the starting velocity $v = \sqrt{\frac{2E}{m}}$ is increased by a factor of $\sqrt{10}$. Therefore, the expansion of regions that are highly accessible to 10 keV protons farther into Callisto's leading hemisphere is driven by the increased proton gyroradii. The enhanced gyroradii at 10 keV make it easier for protons initialized in the leading hemisphere to avoid immediate impact with Callisto (see also Fig. 4(a)). Additionally, near 180° W and 360° W, the reduction in the magnetic field near Callisto's "magnetic poles" further increases ion gyroradii, thereby allowing even more particles that are initialized downstream to escape.

As with 1 keV protons, Fig. 4(b) shows that the northward sense of gyration causes Callisto's northern hemisphere to be more accessible to 10 keV protons than the moon's southern hemisphere. The local accessibility of 1 keV H$^+$ ions in the northern hemisphere reached peak values of $\lambda = 100\%$ and remained at this value up to the geographic north pole (see Fig. 4(a)). However, the local accessibility of 10 keV H$^+$ ions maximizes around values of only $\lambda \approx 90\%$. Additionally, when approaching high northern latitudes in Callisto's trailing hemisphere, the local accessibility of 10 keV protons decreases around the geographic north pole (see Fig. 4(b)). Near each of Callisto's geographic poles, the magnetic field magnitude is enhanced up to twice the background field $|\mathbf{B}_0|$, due to the superposition of Callisto's dipole with the background magnetic field (see, e.g., Fig. 2(e) of this study, or Fig. 7 of Cooper et al. (2001)). Hence,

the local gyroradii are reduced by a factor of two compared to gyration in the background field $\mathbf{B}_0$ alone. The smaller gyroradii in the locally enhanced and curved magnetic field increase the number of newly initialized protons that immediately impact near Callisto's geographic north pole, which reduces the accessibility of 10 keV H$^+$ ions in that region.

Therefore, in contrast to 1 keV protons, accessibility of 10 keV protons in Callisto's upstream hemisphere changes *non-monotonically* with latitude. The difference in proton accessibility near 90° N at these two energies is caused by the change of the proton gyroradius. On the one hand, 1 keV protons have gyroradii of $r_g \approx 0.03 R_C$ near Callisto's north pole. These gyroradii are so small that gyration of these protons can be neglected. Thus, their trajectories are nearly identical to their guiding center paths, many of which do not intersect with Callisto. On the other hand, the gyroradii of 10 keV protons are increased compared to 1 keV protons. As a result, it is easier for gyration of these protons about their guiding centers to cause them to hit the moon, even though their guiding center path does not intersect Callisto.

Fig. 4(c) shows the accessibility of 100 keV protons to Callisto. As with 1 keV and 10 keV protons, the accessibility of 100 keV protons is minimized in the leading hemisphere near 90° W longitude. However in Callisto's trailing hemisphere, while the accessibility distribution is much more diffuse and the values of λ are reduced compared to the two lower energies, the local accessibility λ now assumes non-zero values at all points within this hemisphere. Near the "magnetic poles" in Callisto's equatorial plane, proton accessibility is still increased compared to other locations, but reaches a maximum value of only $\lambda = 72\%$ (compared to $\lambda \approx 100\%$ accessibility at the "magnetic poles" for 1 keV and 10 keV protons, cf. Fig. 4(a) and (b)). For 100 keV protons, regions of high accessibility begin to cluster near the moon's "magnetic poles" (where the magnitude of the magnetic field is minimized with an orientation that is nearly perpendicular to Callisto's surface) and the north/south asymmetry that was visible at lower energies has almost disappeared (see Fig. 4(c)). Away from the two clusters of high accessibility that surround the "magnetic poles," the magnetic field becomes more tangential to the moon's surface, causing more protons to gyrate into the moon before the "reverse $\mathbf{E} \times \mathbf{B}$ drift" is able to transport them upstream. This effect

reduces local accessibility away from these regions (see Fig. 4(c)). The "clustering" becomes even more prominent at higher energies of $E = 1000$ keV and $E = 5000$ keV (see Fig. 4(d) and (e)).

To illustrate this effect, Fig. 5 depicts the trajectories of select 100 keV protons in the electromagnetic field configuration of Run #1. Panel 5(a) shows the trajectories of four protons (in red, green, blue, and orange) projected onto the moon's polar ($y = 0$) plane, which contains the corotational upstream velocity $\mathbf{u}_0$ as well as the northward-pointing convective electric field $\mathbf{E}_0 = -\mathbf{u}_0 \times \mathbf{B}$. The red trajectory corresponds to a proton that is initialized at 0° latitude and 270° W longitude (i.e., in Callisto's equatorial plane at the apex of its trailing hemisphere). This particle is initialized with a velocity of $\mathbf{v}(t = 0) = \sqrt{\frac{2E}{m}}\left[+\frac{1}{\sqrt{2}}, 0, +\frac{1}{\sqrt{2}} \right]$. Therefore, in the *backtracing* approach with a negative time step, this proton initially moves *southward* and toward *upstream*.

The three remaining trajectories (green, orange, and blue in Fig. 5(a)) illustrate the motion of protons that are injected at $\mathbf{r} = [0, 0, 1\tilde{R}_C]$ near Callisto's north pole. These protons are initialized with velocities of $\mathbf{v}(t = 0) = \sqrt{\frac{2E}{m}}\left[-\frac{1}{\sqrt{2}}, 0, -\frac{1}{\sqrt{2}} \right]$ (for the green trajectory), $\mathbf{v}(t = 0) = \sqrt{\frac{2E}{m}}[0, 0, -1]$ (for the orange trajectory), and $\mathbf{v}(t = 0) = \sqrt{\frac{2E}{m}}\left[+\frac{1}{\sqrt{2}}, 0, -\frac{1}{\sqrt{2}} \right]$ (for the blue trajectory). Hence, in the *backtracing* approach, these protons initially move toward *downstream* and *northward* (green), strictly *northward* (orange), and toward *upstream* and *northward* (blue).

Fig. 5(b) shows the trajectories of two *additional* 100 keV protons (in purple and magenta), projected onto Callisto's equatorial ($z = 0$) plane. This plane contains the moon's "magnetic poles" (which are located at $x = 0, y = \pm 1 R_C$) as well as the corotational upstream velocity $\mathbf{u}_0$ and the background field $\mathbf{B}_0$. The two protons are initialized either in Callisto's Jupiter-facing (purple trajectory) or Jupiter-averted (magenta trajectory) hemisphere, at positions $\mathbf{r} = [0, \pm 1\tilde{R}_C, 0]$. The initial velocities of these protons are $\mathbf{v}(t = 0) = \sqrt{\frac{2E}{m}}\left[-\frac{1}{\sqrt{2}}, -\frac{1}{\sqrt{2}}, 0 \right]$ (for the purple trajectory) and $\mathbf{v}(t = 0) = \sqrt{\frac{2E}{m}}\left[-\frac{1}{\sqrt{2}}, +\frac{1}{\sqrt{2}}, 0 \right]$ (for the magenta trajectory).
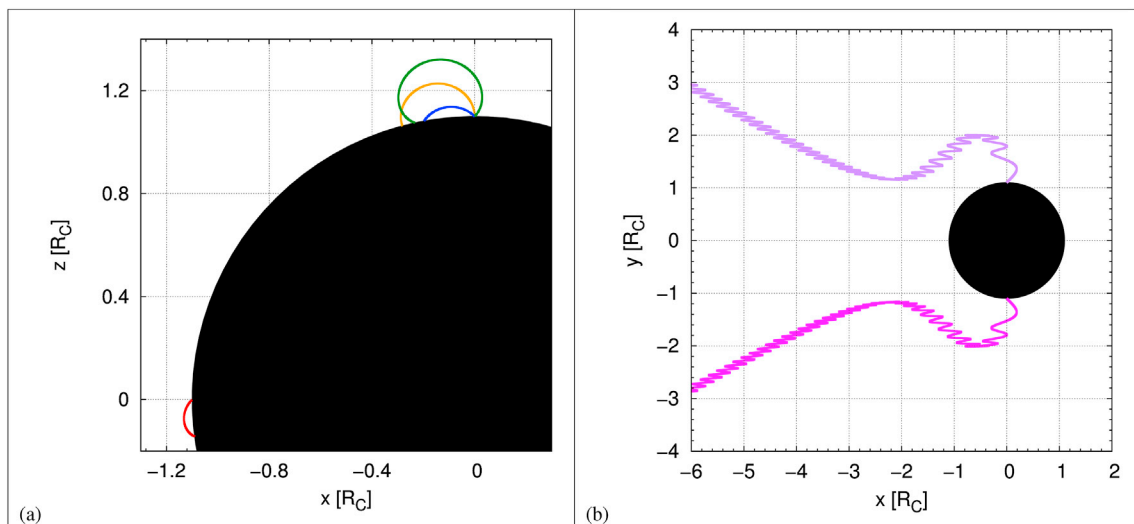

Fig. 5. Trajectories of 100 keV protons in the electromagnetic field configuration of Run #1. Panel (a) shows four trajectories projected onto Callisto's $y = 0$ plane which contains $\mathbf{u}_0$ and $\mathbf{E}_0$, whereas panel (b) shows two additional trajectories projected onto Callisto's equatorial ($z = 0$) plane, which contains $\mathbf{u}_0$, $\mathbf{B}_0$ and $\mathbf{M}_{ind}$. The colored trajectories correspond to individual protons that are inserted at specific points near Callisto with a given velocity vector and traced *backward* in time. In panel (a), the red proton is injected at position $\mathbf{r} = [-\tilde{R}_C, 0, 0]$, whereas the green, blue, and orange protons are injected at $\mathbf{r} = [0, 0, \tilde{R}_C]$. In panel (b), the purple and magenta protons are injected at positions $\mathbf{r} = [0, \pm 1\tilde{R}_C, 0]$ (see text for further documentation). To clearly show the dynamics of these protons, panel (a) is zoomed onto Callisto's northern and trailing hemispheres, whereas panel (b) is zoomed farther out to show more of the upstream region. (For interpretation of the references to color in this figure legend, the reader is referred to the Web version of this article.)

Hence, both of these *back-traced* protons initially move toward *downstream*, with the purple proton initially traveling *toward* Jupiter, and the magenta proton initially traveling *away from* Jupiter.

The cause of decreased proton accessibility in Callisto's equatorial plane and near 270° W longitude (i.e., between the two "clusters") is visible in Fig. 5(a). During its first gyroperiod, the "reverse $\mathbf{E} \times \mathbf{B}$ drift" displaces the red ion toward upstream by less than $1r_g$. Therefore, this proton impacts with Callisto after less than half of a gyration. For the same reason, the gyration of 100 keV protons launched at Callisto's geographic north pole (green, blue, and orange in Fig. 5(a)) causes forbidden trajectories, and thus a reduced accessibility at high northern latitudes (see Fig. 4(c)).

The effect that leads to increased accessibility for 100 keV protons near Callisto's magnetic poles (see Fig. 4(c)) is illustrated by the two proton trajectories depicted in Fig. 5(b). These two H^+ test particles are "funneled" toward the moon's "magnetic poles" by moving nearly parallel/anti-parallel to the field lines close to the surface. Even in this simple electromagnetic field geometry, the protons' guiding centers change their directions multiple times. This "ping-pong" behavior will play an even more important role for energetic ion accessibility when more complex electromagnetic fields near the moon are studied (i.e., Run #2, see Section 3.3).

At even higher energies of 1000 keV and 5000 keV, the north/south and leading/trailing asymmetries in accessibility nearly disappear (illustrated in Fig. 4(d) and (e), respectively). The occurrence of high accessibility near Callisto's "magnetic poles" is even more apparent at these energies, with the extent of these clusters growing in latitude as well as longitude (see Fig. 4(d) and (e)). With increasing energy, the clusters of high accessibility near the moon's "magnetic poles" would grow even further until they merge together, and the local ion accessibility would become uniform with $\lambda \approx 100\%$ everywhere. This is due to the fact that, at energies well above the corkscrew energy $E_{gr} \approx 314$ keV, the large proton gyroradii (with $r_g \gg R_C$) allow ions initialized in Callisto's southern and even in its wakeside hemisphere to completely gyrate around the moon without impacting (see Table 2). Hence, even in these initially inaccessible regions, Callisto then becomes more and more accessible to protons at energies $E \gg E_{gr}$, with the value of λ increasing monotonically with increasing energy.

3.3. Energetic proton accessibility: stronger plasma interaction with Callisto's induced dipole (Run #2)

Maps of the local accessibility of energetic H^+ ions for Run #2 are shown in Fig. 6, whereas the patterns for O^{2+} and S^{3+} ions are discussed in Appendix B. The electromagnetic fields of Run #2 are representative of a stronger plasma interaction with Callisto's induced dipole *alone* (compared to Run #1), again without the presence of Callisto's ionosphere (see Table 1).

Fig. 6(a) shows the local accessibility of Callisto to 1 keV protons. For the electromagnetic fields of Run #2, the accessibility map of 1 keV protons displays similar features as in Run #1 (see Fig. 4): pronounced leading/trailing and north/south asymmetries in accessibility are present. As in Run #1, accessibility for Run #2 reaches values of $\lambda \approx 100\%$ throughout most of Callisto's northern trailing hemisphere.

One main difference in the accessibility of 1 keV protons between Runs #1 and #2 occurs in Callisto's leading hemisphere: above latitudes above of approximately 50° N, the local accessibility in Run #2 remains near values of $\lambda \approx 100\%$ (see Fig. 6(a)), compared to accessibility values of $\lambda = 0\%$ in Run #1 at these latitudes (see Fig. 4(a)). As a result of the stronger interaction between the thermal magnetospheric plasma and Callisto's induced dipole (Run #2), the local magnetic field in Callisto's leading hemisphere is slightly reduced and stretched toward downstream (see Fig. 2(j)). This depletion of $|\mathbf{B}|$ at Callisto's wakeside becomes much more prominent when the ionosphere is included in the hybrid model as

well (e.g., Fig. 2(k) and (l)). Compared to Run #1, the resulting increase of proton gyroradii in the northern leading hemisphere, as well as the slightly changed orientation of the local magnetic field, facilitate the escape of 1 keV protons from this region. Therefore, regions with accessibility values of $\lambda \approx 100\%$ extend from the moon's geographic north pole into the leading hemisphere down to approximately 50° N latitude. At high latitudes in the southern hemisphere, the northward sense of ion gyration again results in protons that immediately impact Callisto after less than a single gyroperiod, reducing accessibility to $\lambda = 0\%$.

An additional difference in the accessibility maps of 1 keV protons between Runs #1 and #2 is visible in the moon's leading hemisphere, but only slightly north of Callisto's equatorial plane. Whereas the regions of non-zero accessibility for Run #1 did not extend more than approximately 5° in longitude into Callisto's leading hemisphere (i.e., from 180° W to 175° W, and from 0° W to 5° W, see Fig. 4(a)), regions of non-zero accessibility of 1 keV protons are able to clearly reach the 150° W and 35° W lines of longitude in Run #2 (see Fig. 6(a)).

The thermal plasma interaction with Callisto's induced dipole is responsible for the longitudinal expansion of these highly accessible regions into the leading hemisphere. In Callisto's geometric equatorial plane, regions of minimized magnetic field (that are formed near the moon's "magnetic poles" even without the plasma interaction) are transported downstream (cf. Fig. 2(e) with 2(f)). This effect will become even more intense when the thermal plasma interaction with Callisto's ionosphere is included as well (see, e.g., Fig. 2(h)), as was also documented in our study of the Galileo C10 flyby (Liuzzo et al., 2016). Due to the expansion of these regions with reduced magnetic field away from the "magnetic poles," Callisto's equatorial leading hemisphere for the electromagnetic fields of Run #2 is more accessible to 1 keV protons than in Run #1.

A third noticeable difference in 1 keV proton accessibility between these two electromagnetic field configurations is visible in Callisto's southern hemisphere (cf. Fig. 4(a) with 6(a)). Whereas 1 keV protons were able to access southern latitudes of Callisto's trailing hemisphere to approximately 60° S in Run #1, protons at the same energy are unable to access latitudes below 30° S when the thermal plasma interaction with Callisto's dipole is stronger (i.e., in Run #2). The "tongue" of non-zero accessibility that extended into the moon's southern trailing hemisphere in Run #1 (see Fig. 4(a)) has completely disappeared in Run #2 (see Fig. 6(a)).

A schematic explaining the reduction in H^+ ion accessibility of Callisto's southern trailing hemisphere is given in Fig. 7. Panel (a) shows the trajectories of two select energetic ions in Callisto's $y = 0$ plane, for the case of uniform electric ($\mathbf{E} = E_0\widehat{\mathbf{z}}$, green), magnetic ($\mathbf{B} = -B_0\widehat{\mathbf{y}}$, pink), and bulk velocity ($\mathbf{u} = u_0\widehat{\mathbf{x}}$, blue) fields. Due to the northward orientation of the convective electric field, the cycloidal trajectories of the back-traced ions are open toward the south, and the ions drift toward upstream. Both ions are able to escape Callisto, within "escape channels" of height $2r_g$ (denoted by solid yellow lines in Fig. 7(a)) that are parallel to the streamlines of the bulk velocity.

Fig. 7(b) shows the trajectories of the same two ions when injected into non-uniform fields perturbed by Callisto's interaction with the thermal magnetospheric plasma. In Callisto's $y = 0$ plane, the plasma displays a deflection pattern around the moon (see Fig. 3(f)) that is similar to the flow pattern near a mass-loading obstacle. The upstream magnetospheric plasma is diverted around Callisto and accelerated toward the moon's northern and southern flanks. This deflection pattern in the $y = 0$ plane becomes much more pronounced when the plasma interaction with Callisto's ionosphere is taken into account as well, see Fig. 3(g) and (h). The modified streamlines result in a convective electric field in Run #2 that is no longer oriented northward, but is rather radial to Callisto and locally enhanced (see Fig. 3(f)). As a result, the guiding center trajectories of the ions in Fig. 7(b) are bent *toward* Callisto, with
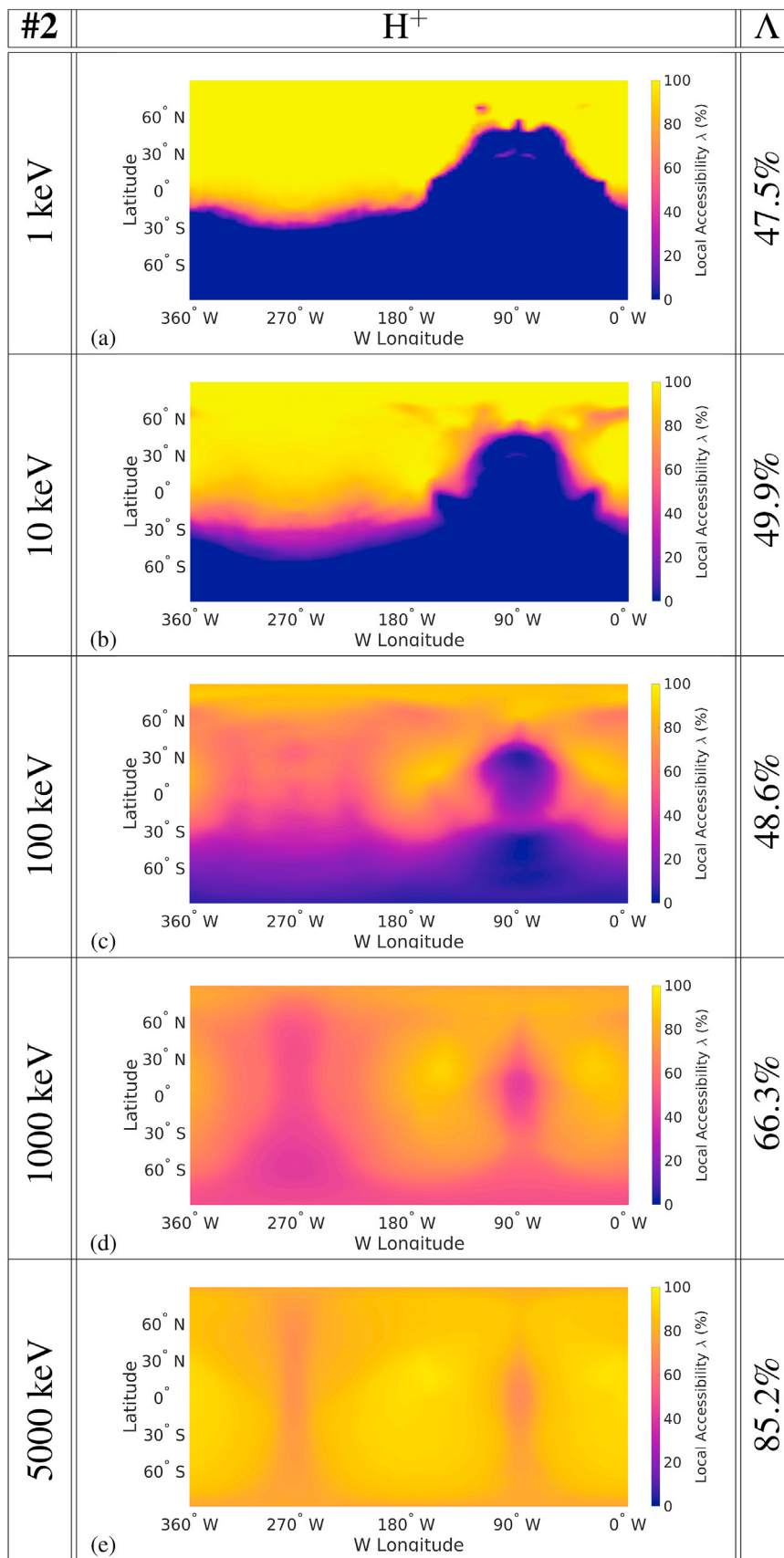
Fig. 6. Local (λ) and global (Λ) energetic proton accessibility of Callisto at select energies for the electromagnetic fields of Run #2, a stronger plasma interaction with Callisto's induced dipole (see Table 1). The energies considered are the same as in Fig. 4. See Fig. 4 and the text for further description.
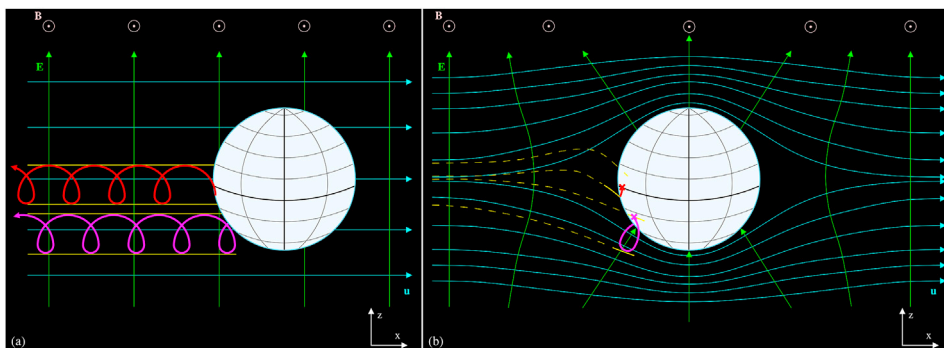
Fig. 7. Schematic of energetic ion gyration near Callisto in an electromagnetic field configuration that is (a) uniform or (b) perturbed by the moon's interaction with the thermal plasma population. Vectors of the electric field (**E**, green), magnetic field (**B**, pink), and bulk velocity (**u**, blue) are shown for both field scenarios. Trajectories of two energetic ions (red and magenta), initialized in Callisto's southern hemisphere and traced *backward* in time, are shown in moon's $y = 0$ plane, which also contains the geographic north and south poles. An arrow at the end of the ion's trajectory denotes that the ion has escaped, whereas an "x" at the end denotes that the particle has impacted Callisto. The "escape channel" for each ion in the $y = 0$ plane is depicted in yellow, with solid lines denoting valid particle trajectories and dashed lines denoting forbidden particle trajectories. The figure is not to scale. (For interpretation of the references to color in this figure legend, the reader is referred to the Web version of this article.)

their "escape channels" located closer to the moon compared to the case with uniform electromagnetic fields. This makes it easier for a particle's trajectory to collide with the moon and become forbidden (denoted by an "x" in Fig. 7(b)).

Therefore, the reduced accessibility for Run #2 at latitudes below 30° S in the trailing hemisphere (see Fig. 6(a)) is due to the changed orientation of the electric field in the immediate vicinity of Callisto. As the magnetospheric plasma is diverted around Callisto, the electric field in the southern hemisphere is reoriented radially *toward* the moon. Compared to the case with uniform electromagnetic fields, the ions' "escape channels" are confined closer to Callisto, and ions initialized in the moon's southern hemisphere are therefore more prone to impacts.

The local accessibility pattern for 10 keV protons, displayed in Fig. 6(b), shows similar features as that of 1 keV protons, as qualitatively similar physical processes are involved in governing the accessibility patterns. However, transitions between regions of high and low values of λ are more smeared-out than for 1 keV protons: the increased gyroradii of 10 keV protons facilitate escape of protons in the northern leading hemisphere, but also slightly reduce accessibility of the northern trailing hemisphere (see Fig. 6(b)).

For protons at energies $E \geq 100$ keV (Fig. 6(c), (d), and 6(e)), the clustering of highly accessible regions centered around Callisto's "magnetic poles" becomes more and more apparent, as was the case with the electromagnetic fields from Run #1. As visible in Fig. 6(c) and (d), the apex of Callisto's leading hemisphere near 90° W longitude and 0° latitude remains largely inaccessible to protons until their energy clearly exceeds the corkscrew energy $E_{gr} \approx 314$ keV. At energies above $E = 5000$ keV, accessibility quickly becomes quasi-homogeneous, with accessibility near 90° W and 270° W longitudes still remaining slightly reduced.

3.4. Energetic proton accessibility: plasma interaction with Callisto's ionosphere alone (Run #3)

The local accessibilities of energetic protons for Run #3 are shown in Fig. 8. Discussion of the accessibility maps for O^{2+} and S^{3+} ions can be found in Appendix C. The electromagnetic field perturbations in this run are generated by the thermal plasma interaction with Callisto's ionosphere *alone*, without the presence of the moon's induced dipole (see Table 1).

Compared to Run #2, the electromagnetic fields of Run #3 are much more perturbed due to the strong interaction of the thermal magnetospheric plasma with Callisto's ionosphere. In Callisto's trailing hemisphere (upstream, $x < 0$), magnetospheric field lines pile up against the moon's ionosphere and form a draping pattern (visible in Fig. 2(c) and (g)). Within the pileup region, the magnetic field is increased in magnitude to nearly twice the background value of $|\mathbf{B}_0| \approx 34$ nT (see Table 1). In Callisto's $y = 0$ plane, this pileup region as well as the associated region of reduced magnetic field in the moon's leading hemisphere (downstream, $x > 0$) are slightly asymmetric (see Fig. 2(k)), due to the large gyroradii of ionospheric pick-up ions and the Hall effect (Liuzzo et al., 2015). As visible in Fig. 3(c) and (g), an envelope of reduced electric field surrounds Callisto, with its size clearly exceeding the bounds of Callisto's ionosphere. Due to their large gyroradii, ionospheric pick-up ions must travel multiple Callisto radii away from the moon along their cycloidal trajectories in order to attain a significant velocity. Close to Callisto, the electric field therefore drops to values of approximately zero due to the decrease in the plasma bulk velocity by nearly three orders of magnitude (see, e.g., Strobel et al. (2002) and Section 3.2 of Liuzzo et al. (2015)).

For Run #3, the accessibility of H^+ ions is shown in Fig. 8(a)–(e) at identical energies as in Figs. 4 and 6. The accessibility pattern of 1 keV protons (see Fig. 8(a)) displays notable differences to Runs #1 and #2 (see Figs. 4(a) and 6(a), respectively). The distinct north/south and leading/trailing asymmetries that occurred in Runs #1 and #2 are no longer present for 1 keV protons in Run #3. Regions of high accessibility began to cluster near Callisto's "magnetic poles" for proton energies $E > 100$ keV in Runs #1 and #2 due to the combination of reduced magnetic field strength and radial field orientation in these regions. For Run #3, Fig. 8(a) displays accumulations of highly accessible regions that are already present at similar locations for protons with energies of $E = 1$ keV. However, we remind the reader that Callisto's induced dipole is *absent* in Run #3. Therefore, the clustering seen in Fig. 8(a) for 1 keV protons must be a result of the field perturbations from the interaction between the thermal plasma and Callisto's ionosphere alone.

Whereas the local accessibility of 1 keV protons reached values of $\lambda \approx$ 100% for Runs #1 and #2 in Callisto's entire northern trailing hemisphere, accessibility in Run #3 reaches a peak value of $\lambda \approx$ 90% that is, however, highly localized in Callisto's equatorial plane near 35° W longitude and 145° W longitude (see Fig. 8(a)). The regions of high λ extend pole-ward to latitudes around 70° N and 70° S. The two clusters of increased accessibility are separated by a band of drastically reduced λ located around 90° W longitude and 270° W longitude which wraps around Callisto as it extends from the moon's geographic north pole to its geographic south pole. The 10° longitudinal width of this band in the
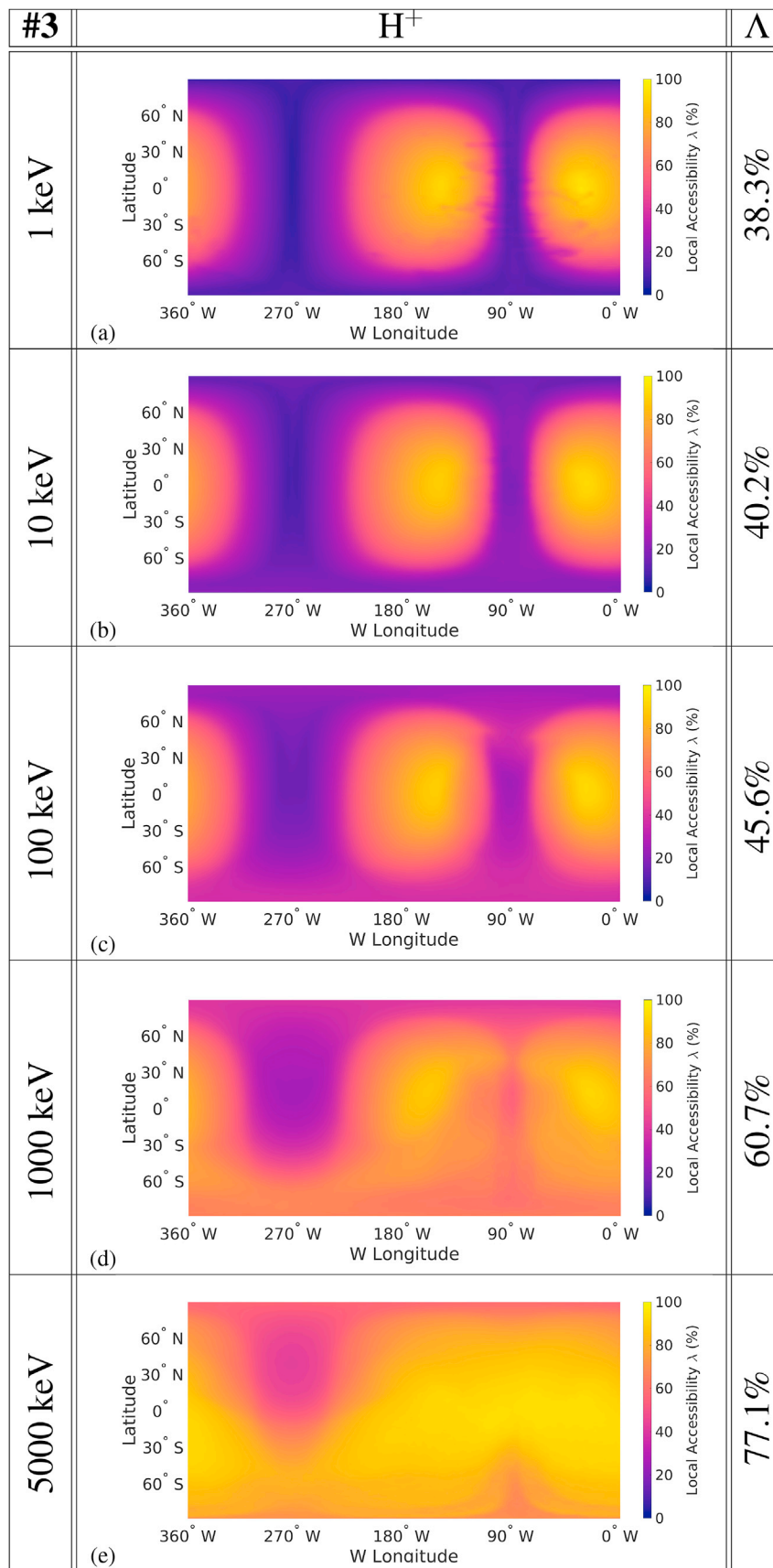
Fig. 8. Local (λ) and global (Λ) energetic proton accessibility of Callisto at select energies for the electromagnetic fields of Run #3, the plasma interaction with Callisto's ionosphere alone (see Table 1). See Fig. 4 and the text for further description.

moon's leading hemisphere is half the width of the band in the trailing hemisphere (about 20° in longitudinal extension). Overall, while boundaries between regions of high and low accessibility were sharply defined in Runs #1 and #2, the accessibility pattern of Run #3 is more blurred, with a non-zero accessibility value at all latitudes and longitudes (see Fig. 8(a)).

Independent of latitude and longitude, the electric field in Run #3 is approximately zero in the region where the energetic test particles are inserted (see Fig. 3(c) and (g), as well as Liuzzo et al. (2015)). Within this electric field void, the contribution of the "reverse $\mathbf{E} \times \mathbf{B}$ drift" to the proton's motion is therefore negligible. As a result, for an ion with a small gyroradius such that its gyration occurs entirely within this electric field void (i.e., for H$^+$ ions below $E \approx 1000$ keV and O^{2+} and S^{3+} ions below $E \approx 100$ keV, see Table 2), there is no longer any drift toward upstream that could either prevent ion escape (in Callisto's leading hemisphere) or facilitate ion escape (in Callisto's trailing hemisphere). In the immediate vicinity of Callisto, the motion of these back-traced ions perpendicular to the magnetic field is therefore dominated by gyration.

To understand the physical processes that generate the accessibility pattern shown in Fig. 8(a), we first discuss a slightly idealized scenario. Consider a vanishing electric field ($\mathbf{E} = 0$) and a spatially homogeneous magnetic field along the $-y$-axis of the CphiO coordinate system (i.e., $\mathbf{B}_0 = -B_0\widehat{\mathbf{y}}$). In addition, all ions are injected at Callisto's surface with an initial velocity vector *perpendicular* to $\mathbf{B}_0$ (i.e., $\mathbf{v}(t = 0) = \mathbf{v}_{\perp,0}$). Such an ion would therefore simply gyrate around this uniform magnetic field. In this scenario, there would be no $\mathbf{E} \times \mathbf{B}$ drift of the ion nor any translation of it along the uniform magnetic field lines. If the initial velocity vector $\mathbf{v}_{\perp,0}$ has a component perpendicular to Callisto's surface, part of the ion's gyration circle will *always* be located beneath the surface. Therefore for this ion, gyration alone will cause it to impact Callisto. Only in the case of $\mathbf{v}_{\perp,0}$ being tangential to the moon's surface could the ion complete a full gyration circle unimpeded by Callisto. Even in this case however, the ion may still impact the moon if the Lorentz force at time $t = 0$ (i.e., $q\mathbf{v}_{\perp,0} \times \mathbf{B}_0$) points *toward* Callisto.

In this idealized example, the largest number of impacts associated with pure gyration occurs in Callisto's $y = 0$ plane. This plane contains Callisto's leading and trailing apices (at longitudes of 90° W and 270° W, respectively), as well as the moon's geographic north and south poles (at latitudes of 90° N and 90° S, respectively). At each point on the moon's surface within this plane, there is only *one* initial velocity vector $\mathbf{v}_{\perp,0}$ perpendicular to the $y = 0$ plane and the magnetic field (for a given initial energy E) that does *not* lead to an impact. When leaving the $y = 0$ plane and moving into Callisto's Jupiter-facing and Jupiter-averted hemispheres, the number of gyration-associated impacts decreases. Upon reaching the apices of Callisto's Jupiter-facing and Jupiter-averted hemispheres (i.e., at a latitude of 0° and longitudes of 0° W and 180° W, respectively), *all* initial velocity vectors $\mathbf{v}_{\perp,0}$ allow for unimpeded ion gyration.

In our idealized scenario, an accessibility map of Callisto's surface would appear as follows: the accessibility minima would be located along the circle $\mathscr{C} \equiv \{[x,y,z] \big| \sqrt{x^2+z^2} = \tilde{R}_C \text{ and } y = 0\}$. This circle is the locus of points where the $y = 0$ plane intersects Callisto's surface (i.e., all latitudes at 90° W and 270° W longitudes). The circle $\mathscr{C}$ also includes the moon's geographic north and south poles. The maxima of accessibility would be located at the moon's Jupiter-facing and Jupiter-averted apices (in the moon's equatorial plane at longitudes 0° W and 180° W). We note that this accessibility pattern is already qualitatively very similar to that of 1 keV protons in Run #3 (see Fig. 8(a)).

Despite these strong similarities, unimpeded ion gyration about a uniform magnetic field does not satisfy the escape condition of the GENTOo simulation (see Section 2.2). As there is no significant contribution from the "reverse $\mathbf{E} \times \mathbf{B}$ drift" within the reduced electric field envelope encompassing Callisto, an ion must have some initial velocity

that is parallel to the magnetic field ($\mathbf{v}_{\parallel,0} \neq 0$) in order to escape the moon.

We therefore now return to our idealized scenario with $\mathbf{B}_0 = -B_0\widehat{\mathbf{y}}$ and $\mathbf{E} = 0$, but consider *only* translation of the newly initialized ions along the magnetic field lines (i.e., in the $\pm\widehat{\mathbf{y}}$ direction). For points on the circle $\mathscr{C}$, there are two velocity vectors with $\mathbf{v}(t = 0) = \mathbf{v}_{\parallel,0} = \pm v_{\parallel,0}\widehat{\mathbf{y}}$ that allow for an ion to escape (again, for a given initial energy E). At every point that is not on $\mathscr{C}$, there is only a single parallel velocity vector that allows for escape. For an ion that is initialized on the moon's surface at some position $y > 0$ (i.e., in Callisto's Jupiter-facing hemisphere), this initial velocity vector would read $\mathbf{v}_{\parallel,0} = -v_{\parallel,0}\widehat{\mathbf{y}}$ (so that the *back-traced* ion travels along $+\widehat{\mathbf{y}}$). For an ion initialized on the surface at some position $y < 0$ (i.e., in Callisto's Jupiter-averted hemisphere), this initial velocity vector would read $\mathbf{v}_{\parallel,0} = +v_{\parallel,0}\widehat{\mathbf{y}}$ (so that the *back-traced* ion travels along $-\widehat{\mathbf{y}}$). In other words, the number of initial velocities $\mathbf{v}_{\parallel,0}$ that lead to escape is the same for all surface points (i.e., only a single vector at a given energy E), except for points on the circle $\mathscr{C}$ where this number doubles. Therefore, the accessibility map associated with pure parallel motion would be homogeneous (except for locations on $\mathscr{C}$, where escape would be impeded by gyration anyway).

Thus, in our idealized scenario (with $\mathbf{B}_0$ along $-\widehat{\mathbf{y}}$ and $\mathbf{E} = 0$), and for an ion whose initial velocity is a superposition of perpendicular and parallel motion ($\mathbf{v}(t = 0) = \mathbf{v}_{\perp,0} + \mathbf{v}_{\parallel,0}$), two factors facilitate ion escape: (i) a "favorable" gyration circle that is unimpeded by Callisto, and (ii) a "favorable" initial parallel velocity that is directed away from the moon. However, the number of protons with a "favorable" parallel velocity vector is *identical* for all injection points (except those on $\mathscr{C}$, where the number is doubled). Therefore, the accessibility pattern displayed in Fig. 8(a) is roughly a map of locations with a large number of "favorable" gyration circles, and key features of the 1 keV proton accessibility map in Fig. 8(a) can be understood in terms of pure gyration within the electric field void that surrounds Callisto.

In the forward integration approach, energetic ion dynamics for this idealized scenario would work as follows: once the drifting upstream ions enter the electric field void that envelops Callisto, their $\mathbf{E} \times \mathbf{B}$ drift velocity immediately becomes negligible. Thus, these ions can only further approach Callisto through an initial non-zero velocity component parallel to the magnetic field. In this case, an energetic ion can only impact Callisto if the tube of radius r_g centered around the "guiding" magnetic field line intersects the moon. Conversely, if the parallel velocity of the approaching ion is negligible, it will enter a state of pure gyration within the electric field void. If the upstream conditions near Callisto did not change, such a gyrating ion could remain captured near the moon indefinitely without ever hitting the surface. An upper limit on the residence time of such an ion is given by half of a synodic rotation period, on the order of 5 h at Callisto.

Although our idealized scenario is able to qualitatively explain the accessibility pattern displayed in Fig. 8(a), there are some quantitative differences. While the idealized scenario predicts accessibility maxima at 0° W longitude and 180° W longitude in Callisto's equatorial plane, the maxima in accessibility of 1 keV protons in Fig. 8(a) are slightly shifted toward Callisto's leading hemisphere, occurring at longitudes of 35° W and 145° W, respectively. This discrepancy is caused by the tilt of the magnetic field toward Callisto's leading hemisphere due to field line draping (see Fig. 2(c)). We note that, with an Alfvénic Mach number of $M_A = 0.8$ for the magnetospheric upstream plasma in Run #3, the Alfvén wings are inclined against the magnetospheric background field by an angle of nearly $\tan^{-1}(0.8) \approx 40°$ (Neubauer, 1980). This angle is approximately equal to the angle by which the equatorial accessibility maxima are displaced toward downstream compared to the idealized scenario with uniform magnetic field along $-\widehat{\mathbf{y}}$.

An additional difference is that the idealized scenario predicts bands of low accessibility at 90° W longitude and 270° W longitude that are of

the same longitudinal width. However, Fig. 8(a) shows that a slightly broader band of reduced accessibility is formed in Callisto's trailing hemisphere (near 270° W longitude) compared to its leading hemisphere (near 90° W longitude). The difference in the longitudinal width of the two accessibility minima is caused by the leading/trailing asymmetry of the magnetic field strength near Callisto. Fig. 2(g) and (k) show that, at the moon's ramside, the magnetic field magnitude within the pileup region is nearly a factor of two larger than the background magnetospheric field $|\mathbf{B}_0|$. This enhancement *reduces* the local gyroperiod of an ion at this location by a factor of two compared to an ion in the undisturbed magnetospheric field. At Callisto's wakeside, the magnetic field is reduced by a factor of three compared to the background field, which *increases* the local gyroperiod of an ion by a factor of three.

Therefore, during a single gyroperiod, a back-traced ion with an initial parallel velocity component $\mathbf{v}_{\parallel,0}$ in Callisto's leading hemisphere travels in the direction of the magnetic field about six times farther than an ion in the moon's trailing hemisphere with the same $\mathbf{v}_{\parallel,0}$. After one gyration, an ion in the leading hemisphere has therefore reached a much larger distance to Callisto than an ion in the trailing hemisphere. For an ion in Callisto's leading hemisphere, this makes it more difficult for the ion to collide with the surface when it returns to the proximity of the moon upon completion of its gyration cycle. This effect reduces the longitudinal width of the band of low accessibility in Callisto's leading hemisphere compared to its trailing hemisphere.

To further highlight this effect, Fig. 9 depicts the trajectories of select 100 keV protons in the electromagnetic fields of Run #3. This energy is chosen to clearly illustrate the differences in proton gyroradii between Callisto's trailing and leading hemispheres, which would be too subtle to visualize for a proton with an energy of only $E = 1$ keV. However, the same physical processes occur for 1 keV protons as well.

The trajectories of four protons are shown projected onto Callisto's $z = 0$ plane, which contains the upstream corotational velocity $\mathbf{u}_0$ as well as the background magnetospheric field $\mathbf{B}_0$. The two protons injected at Callisto's trailing apex (270° W longitude) are launched with initial velocities of $\mathbf{v}(t = 0) = \sqrt{\frac{2E}{m}}\left[+\frac{1}{\sqrt{2}}, -\frac{1}{\sqrt{2}}, 0\right]$ for the purple trajectory, and
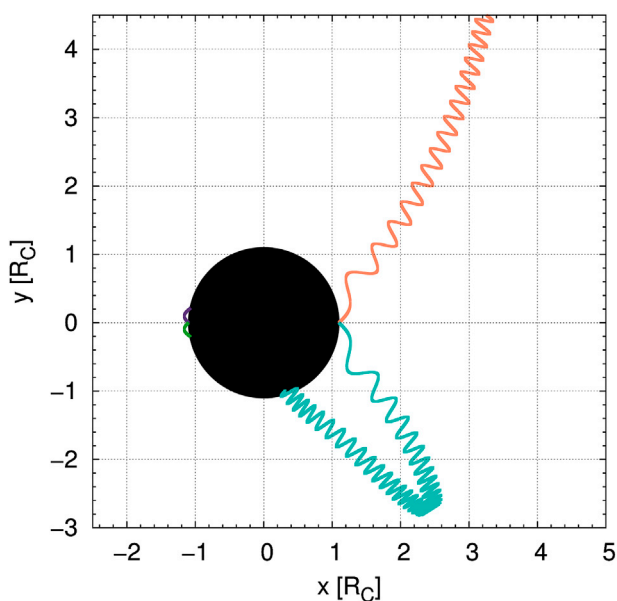
$\mathbf{v}(t = 0) = \sqrt{\frac{2E}{m}}\left[+\frac{1}{\sqrt{2}}, +\frac{1}{\sqrt{2}}, 0\right]$ for the green trajectory. These *back-traced* protons therefore initially both travel toward upstream, and toward the Jupiter-facing (purple trajectory) or Jupiter-averted (green trajectory) hemisphere of Callisto.

The two protons injected at Callisto's leading apex (90° W longitude) are counterparts to those injected at the trailing apex: the orange proton has an initial velocity of $\mathbf{v}(t = 0) = \sqrt{\frac{2E}{m}}\left[+\frac{1}{\sqrt{2}}, +\frac{1}{\sqrt{2}}, 0\right]$, whereas the teal proton has an initial velocity of $\mathbf{v}(t = 0) = \sqrt{\frac{2E}{m}}\left[+\frac{1}{\sqrt{2}}, +\frac{1}{\sqrt{2}}, 0\right]$. Therefore, these two *back-traced* protons initially move toward downstream, with the orange proton initially moving toward Jupiter, and the teal proton initially moving away from Jupiter.

The effect of the different magnetic field strengths in Callisto's leading and trailing hemispheres is distinct. In the trailing hemisphere, the gyroperiod and gyroradii of the two protons are significantly reduced compared to the gyroperiods and gyroradii of the protons in the leading hemisphere. As can be seen in Fig. 9, the protons downstream of Callisto are able to travel much farther along the magnetic field lines during a single period than their counterparts upstream. Therefore, the two ions injected at 90° W longitude (orange and teal) are able to travel far enough from Callisto during their first gyration to avoid immediate impact with the moon, whereas the ions injected upstream (purple and green) immediately impact.

Although the orange ion injected at 90° W longitude is able to escape Callisto, the teal ion injected at the same position (with a velocity mirrored against the $y = 0$ plane compared to the orange ion) is redirected toward the moon and ultimately impacts. This illustrates the strong influence of even subtle asymmetries in Callisto's electromagnetic environment (that are present everywhere outside of the $z = 0$ plane) on energetic ion dynamics. Both protons experience these asymmetries due to their non-zero gyroradii. The two protons injected in the leading hemisphere ultimately reach regions of non-negligible electric field and therefore eventually experience the "reverse $\mathbf{E} \times \mathbf{B}$ drift" which carries them toward upstream. However, this occurs much farther from Callisto for the orange proton than for the teal proton, which is deflected by Callisto's Jupiter-averted Alfvén wing and impacts the moon (see Fig. 9).

In the forward integration approach, the magnetic pileup region upstream of Callisto acts as a barrier to energetic protons. Protons from Jupiter's magnetosphere would approach from upstream and encounter the magnetic pileup region where the gradient in the magnetic field strength points toward Callisto (i.e., it has a strong component along the $+ x$-axis). With the magnetic field inside of the pileup region mainly oriented along the $- y$-axis, the gradient drift (along $+\hat{z}$ for a positive ion) would divert these protons around Callisto toward its geographic north pole. This effect has also been found to play an important role in the dynamics of energetic particles near Europa, where the gradient drift due to ramside field line pileup caused a "bite-out" in the signature of energetic electrons detected by the EPD during the E12 Galileo flyby (see Figs. 3 and 7 in Paranicas et al. (2000) and discussion within).

For proton energies of $E = 10$ keV and $E = 100$ keV, the accessibility maps look qualitatively similar as for 1 keV protons (see Fig. 8(b) and (c)). Regions of high accessibility cluster near 35° W longitude and 145° W longitude, extend pole-ward, and are separated by a band of reduced accessibility near 90° W longitude and 270° W longitude. The polar regions of Callisto remain nearly inaccessible.

At even higher energies of $E = 1000$ keV and $E = 5000$ keV, a slight north/south asymmetry in proton accessibility begins to form: while the local accessibility near Callisto's geographic north pole remains around only $\lambda = 40\%$, accessibility near the moon's geographic south pole already reaches values of $\lambda \approx 70\%$ (see Fig. 8(d) and (e)). This enhanced accessibility of Callisto's southern hemisphere is caused by the asymmetry of the magnetic field strength between the moon's northern and southern hemispheres (see Fig. 2(k)). The slightly reduced magnetic field

Fig. 9. Trajectories of four 100 keV protons (displayed in purple, green, orange, and teal) exposed to the electromagnetic field configuration of Run #3, and projected onto Callisto's $z = 0$ plane which contains the upstream bulk velocity $\mathbf{u}_0$ as well as the magnetospheric field $\mathbf{B}_0$. The trajectories correspond to ions injected at positions $\mathbf{r} = [\pm \tilde{R}_C, 0, 0]$ (i.e., in the $z = 0$ plane) and traced *backward* in time, with various initial velocity vectors (see text for discussion).

below Callisto's south pole compared to its north pole enhances the local gyroperiod of ions in the south compared to those in the north. Therefore, protons back-traced from the moon's southern hemisphere are able to travel farther from Callisto during a single gyration cycle compared to those in the northern hemisphere, which reduces the number of impacts at southern latitudes and increases the local proton accessibility. The reduced magnetic field in Callisto's leading hemisphere (see Fig. 2(g) and (k)) also causes the accessibility of 5000 keV protons at the leading apex of Callisto to reach a value of $\lambda = 100\%$. For Runs #1 and #2, the leading apex was not fully accessible even at this high energy (cf. Figs. 4(e) and 6(e)). Additionally, at these higher energies, the newly initialized ions may already leave the electric field void that surrounds Callisto during part of their first gyration cycle. Therefore, with increasing energy, the "reverse $\mathbf{E} \times \mathbf{B}$ drift" tends to play a stronger role for energetic ion dynamics near Callisto.

3.5. Energetic proton accessibility: plasma interaction with Callisto's induced dipole and ionosphere (Run #4)

The perturbations in the electromagnetic fields of Run #4 are generated by the interaction of the thermal magnetospheric plasma with Callisto's ionosphere and induced dipole. Similar to Run #3, the magnetospheric field drapes around the moon, with its magnitude downstream slightly reduced to $|\mathbf{B}| \approx 15$ nT (see Fig. 2(d), (h), and 2(l)). Additionally, an electric field void still envelops Callisto (see Fig. 3(d) and (h)). However, the magnetic field of Run #4 is substantially different from Run #3 near Callisto's wakeside surface, as the quasi-dipolar "core region" is visible downstream of the moon. This wakeside region where the dipole field dominates the magnetic signatures is entirely contained within the electric field void that surrounds Callisto. Therefore the idealized scenario presented in Section 3.4 (pure gyration with no $\mathbf{E} \times \mathbf{B}$ drift) is applicable within the quasi-dipolar "core region" for those particle energies where the resulting gyroradii are small enough such that the initial gyration of the back-traced ions occurs within the void. Additionally, the magnitude of the magnetic field is locally reduced near the moon's "magnetic poles" (located at $x = 0$, $y = \pm 1R_C$), similar to Runs #1 and #2.

Fig. 10 displays the accessibility patterns of energetic protons for Run #4 at the same energies as in Runs #1, #2, and #3. Again, the accessibility patterns of O^{2+} and S^{3+} ions are discussed in Appendix D. The accessibility patterns of protons with energies $E \leq 100$ keV (see Fig. 10(a), (b), and (c)) are similar to proton accessibility at the same energies in Run #3: clusters of increased accessibility form around Callisto's equatorial plane in the leading hemisphere near longitudes of 35° W and 145° W, respectively. However, while the maximum value of proton accessibility in Run #3 for energies $E \leq 100$ keV reached $\lambda \approx 90\%$, the maximum value in Run #4 does not exceed $\lambda \approx 50\%$ anywhere (cf. Fig. 8(a)–(c) with Fig. 10(a)–(c)). A longitudinal band of reduced accessibility again encircles Callisto, centered around 90° W longitude and 270° W longitude. However, in the trailing hemisphere the band is much broader than in Run #3, and now nearly extends to the edges of the trailing hemisphere toward its Jupiter-facing and Jupiter-averted apices.

The explanation for these features is analogous to Run #3: near Callisto's surface, ions are injected into the envelope of drastically reduced electric field. Therefore, the only way that they can escape Callisto is through an initial velocity parallel to the magnetic field and a "favorable" gyration circle. The accessibility thus maximizes near the moon's Jupiter-facing and Jupiter-averted apices where the local magnetic field is nearly perpendicular to Callisto and the number of ions with a "favorable" gyration circle is highest. In complete analogy to Run #3, draping of the magnetic field causes these regions of maximum accessibility to be slightly offset into Callisto's leading hemisphere.

The most striking qualitative difference between proton accessibil-

ities of Runs #3 and #4 are two ring-like regions of reduced λ that have been "carved out" of the two clusters of high accessibility. These "rings" encircle the accessibility maxima near 0° latitude and longitudes of 35° W and 145° W (i.e.,they are formed in Callisto's leading hemisphere, see Fig. 10(a)–(c)). On either side of these "rings," λ increases.

To reveal the process that causes these two ring-like gaps to form in the accessibility pattern of Run #4 (but not in Run #3), Fig. 11(a) and (b) show the B_x component of the magnetic field for these two runs in Callisto's $z = 0$ plane for $-2R_C \leq x$, $y \leq 2R_C$, along with the projection of the magnetic field vectors onto this plane. Fig. 11(c) again displays the accessibility pattern for 10 keV protons in Run #4, and labels ①, ②, ③, and ④ are used to link features in the accessibility pattern to the associated magnetic field regimes near Callisto's wakeside surface (see Fig. 11(b)). Labels ① and ④ in Fig. 11(a) denote those segments where the magnetic field orientation (and hence, the accessibility patterns) of Run #3 are similar to those of Run #4. However, the segments in Fig. 11(a) are *not* directly related to features in the accessibility map displayed in Fig. 11(c).

Fig. 11(a) shows that in Callisto's leading hemisphere ($x > 0$), the magnetic field is tangential to the moon's surface only at the apex of the leading hemisphere (i.e., at $x = 1R_C$, $y = 0$), denoted segment ①. Near this point, B_x reverses sign from $B_x < 0$ in the moon's Jupiter-facing hemisphere ($y > 0$) to $B_x > 0$ in its Jupiter-averted hemisphere ($y < 0$), corresponding to the transition between the two Alfvén wings. Traveling along Callisto's surface from its leading apex into its Jupiter-facing and Jupiter-averted hemispheres (i.e., into segments ④ in Fig. 11(a)), the magnetic field becomes increasingly radial to the moon and energetic ion accessibility increases (see discussion in Section 3.4).

Similar to Run #3, the magnetic field of Run #4 is tangential to Callisto's surface near the apex of its leading hemisphere, denoted by labels ① in Fig. 11(b) and (c). However, when traveling from Callisto's leading apex into its Jupiter-facing and Jupiter-averted hemispheres, the field within the quasi-dipolar "core region" maintains a strong component tangential to the surface. This quasi-dipolar "core region" is indicated by the faint red ($B_x > 0$ for $y > 0$) and blue ($B_x < 0$ for $y < 0$) shading near the wakeside surface of Callisto, and corresponds to segments ② and ③ in panels 11(b) and 11(c). These regions are also visible in the magnetic field vectors: the B_x component within the quasi-dipolar "core region" has an opposite orientation compared to the adjacent Alfvén wings. In the $y > 0$ hemisphere, the field in the Jupiter-facing Alfvén wing has $B_x < 0$ (shaded blue in Fig. 11(b)), whereas the quasi-dipolar "core region" in this hemisphere rather has $B_x > 0$ (shaded red). The opposite is true in the $y < 0$ hemisphere: the quasi-dipolar "core region" has $B_x < 0$, whereas the Jupiter-averted Alfvén wing is characterized by $B_x > 0$.

This strong tangential component of the magnetic field counteracts the increase of accessibility when moving away from Callisto's leading apex (i.e., when entering the segments labeled ②) that was seen in Run #3. Within segments ② in Fig. 11(b) and (c), the field lines are still slightly "detached" from Callisto, and accessibility begins to slightly increase (as within segments ④ of Run #3), thereby forming the outer circular edges of the two clusters. However when entering segments ③ where the field is nearly tangential to Callisto's surface, the tendency for the accessibility to increase (as clearly demonstrated in Fig. 8 for Run #3) is overcome by the enhanced number of impacts associated with the strongly tangential magnetic field. This is one of the reasons why the local accessibility decreases near longitudes of 45° W and 135° W (see, e.g., segments ③ in Fig. 11(c)).

These minima in λ are therefore associated with those segments of the quasi-dipolar "core region" where the change in orientation of the magnetic field is strongest. Within segment ③ of the Jupiter-averted hemisphere, the field lines change direction from $B_x > 0$ in Callisto's Alfvén wing to $B_x < 0$, following the curvature of the moon's surface away from its leading apex. In the corresponding segment of the Jupiter-
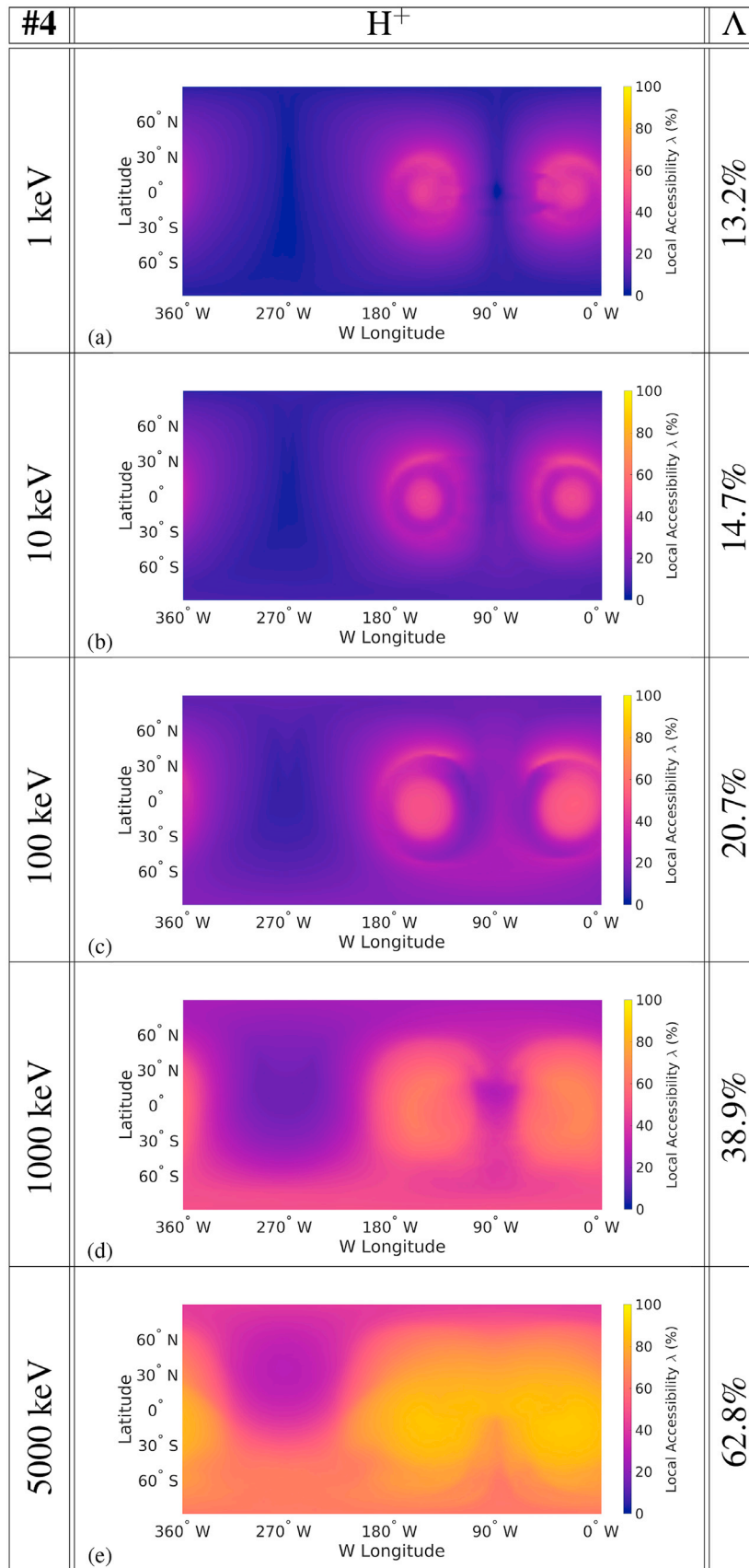
Fig. 10. Local (λ) and global (Λ) energetic proton accessibility of Callisto at select energies for the electromagnetic fields of Run #4, the plasma interaction with Callisto's ionosphere *and* induced dipole (see Table 1).
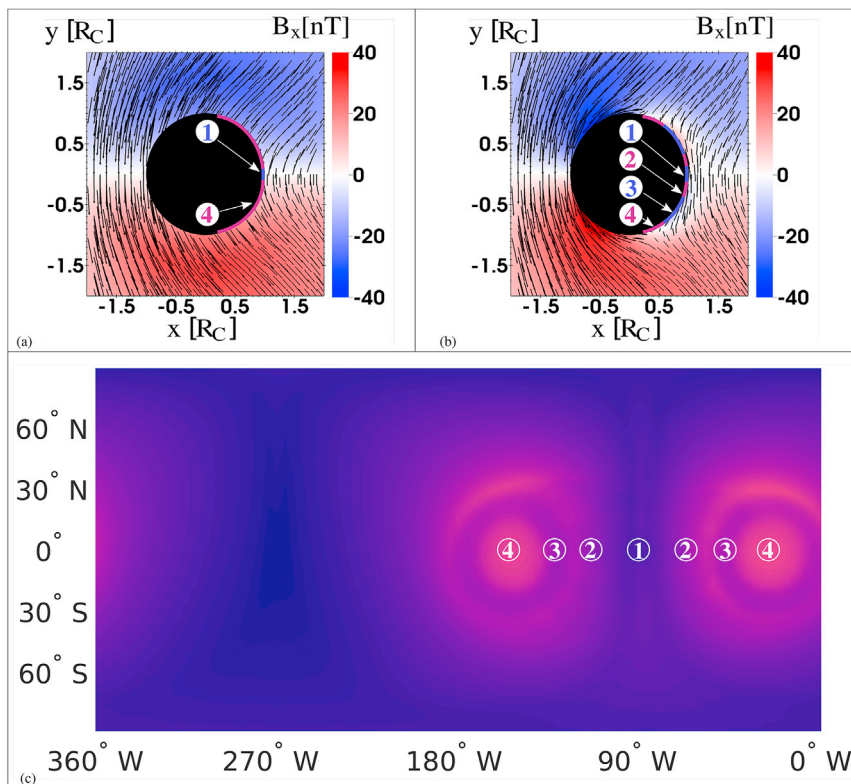
Fig. 11. Effect of the quasi-dipolar "core region" on energetic ion accessibility. (a) B_x component of the magnetic field in Run #3 in Callisto's $z = 0$ plane, with vectors of the magnetic field projected onto this plane. Labels ① and ④ denote segments where the orientation of the magnetic field in Run #3 is similar to that in Run #4. (b) B_x and projected magnetic field vectors for the magnetic field of Run #4. Segments labeled ①, ②, ③, and ④ are used to link features in the accessibility pattern (panel (c)) to the local orientation of the magnetic field. Each of the four segments labeled in Callisto's Jupiter-averted hemisphere have a counterpart in the Jupiter-facing hemisphere where the same physical processes occur. (c) Map of accessibility of 10 keV protons to Callisto for Run #4, as also displayed in Fig. 10(b) and with an identical color scale, omitted here to enhance visibility of the features in the panel. Segments ① through ④ correspond to those in Fig. 11(b). (For interpretation of the references to color in this figure legend, the reader is referred to the Web version of this article.)
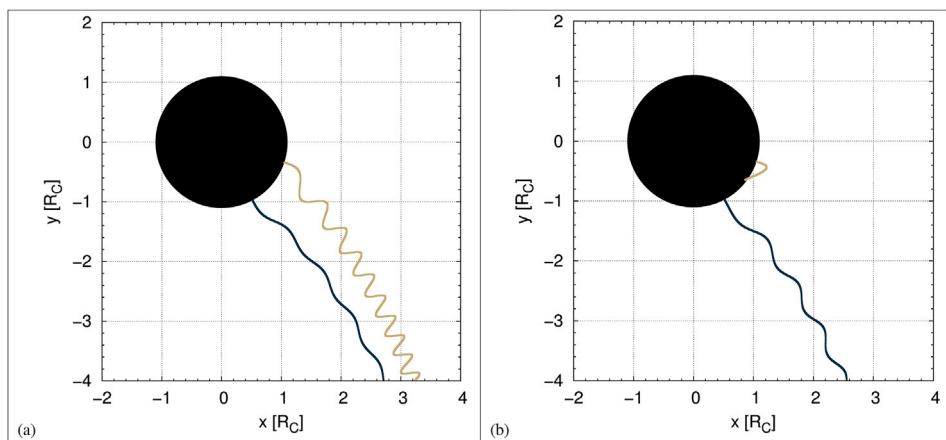
Fig. 12. Trajectories of 100 keV test particles projected onto Callisto's $z = 0$ plane for the electromagnetic fields of (a) Run #3 and (b) Run #4. Each ion is injected in Callisto's $z = 0$ plane (i.e., at 0° latitude) with a velocity vector that is radial to the surface. The gold trajectories correspond to ions injected at 108° W longitude, whereas the blue trajectories correspond to ions injected at 152° W longitude. For panel (b), the gold ion is injected in segment ③ in Fig. 11(b) and (c), whereas the blue ion is injected in segment ④ in Fig. 11(b) and (c). (For interpretation of the references to color in this figure legend, the reader is referred to the Web version of this article.)

facing hemisphere, this change in B_x orientation is mirrored. Within segments ③ of the quasi-dipolar "core region," the magnetic field is most strongly curved. Therefore, the curvature drift is at its strongest here as well. Within the quasi-dipolar "core region" and in Callisto's $z = 0$ plane, this drift is tangential to the moon's surface and points approximately along the $- z$-axis. The curvature drift therefore keeps newly injected ions near the surface of Callisto where they are more prone to impacting, and hence contributes to the rings of reduced ion accessibility in Callisto's leading hemisphere.

When exiting the wakeside quasi-dipolar "core region" and approaching Callisto's Jupiter-facing and Jupiter-averted apices (i.e., within segments marked ④ in Fig. 11(b) and (c)), energetic proton accessibility again begins to increase, forming the circular centers of the two clusters of high accessibility. Within these segments, the magnetic field again becomes nearly radial to Callisto's surface as field line draping begins to dominate the local magnetic perturbations, thereby enhancing

energetic proton escape as was also seen within segments ④ of Run #3.

To further investigate the effect of the quasi-dipolar "core region" on energetic proton accessibility, Fig. 12(a) and (b) depict the trajectories of two 100 keV protons exposed to the electromagnetic fields of Runs #3 and #4, respectively. All four ions are injected with an initial velocity that is radial to Callisto, with the gold ions injected at 0° latitude and 108° W longitude, and the blue ions injected at 0° latitude and 152° W longitude. In Fig. 12(b), the gold proton is therefore injected within segment ③, whereas the blue proton is injected within segment ④ (see also Fig. 11(b) and (c)).

For Run #3, the blue and the gold proton are both able to escape Callisto's interaction region, since the magnetic field near these longitudes has a strong radial component (see Fig. 11(a)). However, while the blue proton in Run #4 is still able to escape due to the mainly radial orientation of the magnetic field within segment ④, the gold proton immediately impacts Callisto due to the nearly tangential field

orientation within segment ③ (see Fig. 12(b)).

Exiting segment ④ and moving into Callisto's ramside hemisphere, the magnetic field in Run #4 near Callisto's Jupiter-facing and Jupiter-averted apices (i.e., at 90° W and 270° W) is even more strongly draped than in Run #3. The magnitude of the perturbed B_x in Run #4 is thus slightly higher compared to Run #3, and the field is more tangential to Callisto's surface near the two apices (cf. Fig. 11(a) with 11(b)). Therefore, when moving toward Callisto's trailing (ramside) hemisphere, the accessibility values in Run #4 (displayed in Fig. 10(a)–(c)) approach $\lambda \approx$ 0% more rapidly than in Run #3. Thus, the band of reduced accessibility in Callisto's trailing hemisphere in Run #4 is much wider than in Run #3.

For energies $E > 100$ keV (see Fig. 10(d) and (e)), the accessibility patterns of Run #4 are similar to those of Run #3. The two clusters of increased accessibility begin to merge in the leading hemisphere near 90° W longitude and the rings of reduced accessibility within the clusters disappear as well. Callisto's southern hemisphere becomes more accessible than its northern hemisphere, due to the slightly asymmetric magnetic field perturbations (see Fig. 2(l)).

4. Energetic ion accessibility of Callisto during the Galileo C3, C9, and C10 flybys

Throughout its eight year mission at Jupiter, the Galileo spacecraft performed seven Callisto flybys during which the magnetometer was active. However, Callisto's inductive response to the time-varying Jovian background field was clearly identifiable only during the first three encounters (labeled C3, C9, and C10), see, e.g., Liuzzo et al. (2017).

Around closest approach of the C3 flyby on 4 November 1996, Callisto was located approximately $3.2R_J$ *above* the center of Jupiter's magnetospheric current sheet. Near the moon, the magnetospheric background field was $\mathbf{B}_0 = [-2.4\hat{\mathbf{x}} - 31.7\hat{\mathbf{y}} - 10.8\hat{\mathbf{z}}]$ nT; i.e., the background field pointed away from Jupiter and was tilted southward at an angle of approximately 19° against the $z = 0$ plane. Conversely, near closest approach of the C9 flyby on 25 June 1997, Callisto was located approximately $3.5R_J$ *below* the center of the Jovian magnetospheric current sheet. During C9, the background magnetic field was $\mathbf{B}_0 = [+3.3\hat{\mathbf{x}} + 33.9\hat{\mathbf{y}} - 9.4\hat{\mathbf{z}}]$ nT; i.e., it pointed toward Jupiter and formed an angle of approximately 15° with the $z = 0$ plane. For both flybys, the magnetospheric field component along the corotation direction ($B_{x,0}$) was small. Therefore, Callisto's induced magnetic moment $\mathbf{M}_{\text{ind}}$ was still mainly along $+\hat{\mathbf{y}}$ during C3 and along $-\hat{\mathbf{y}}$ during C9, as the $B_{z,0}$ component does not contribute to induction at Callisto (see, e.g., Kivelson et al. (1999); Zimmer et al. (2000)).

Due to the large distance of Callisto from the center of the Jovian current sheet during C3 and C9, the thermal magnetospheric plasma interaction during these flybys was weak. The Galileo magnetometer observed bipolar perturbation signatures in B_x and B_y during both encounters, and two alternative interpretations have been used to explain these observations. The first is that these features were produced by a dipole induced within a conducting subsurface ocean at Callisto (e.g., Khurana et al. (1998); Kivelson et al. (1999); Zimmer et al. (2000); Liuzzo et al. (2015)). This approach is able to explain C3 and C9 magnetic field data without taking into account any currents associated with Callisto's ionosphere (due to, e.g., mass-loading or induction within the ionosphere itself). The second, alternate interpretation is that the observed magnetic features were generated by induction within Callisto's ionosphere alone, as discussed by Hartkorn and Saur (2017). This approach can explain magnetometer data from C3 without any ocean
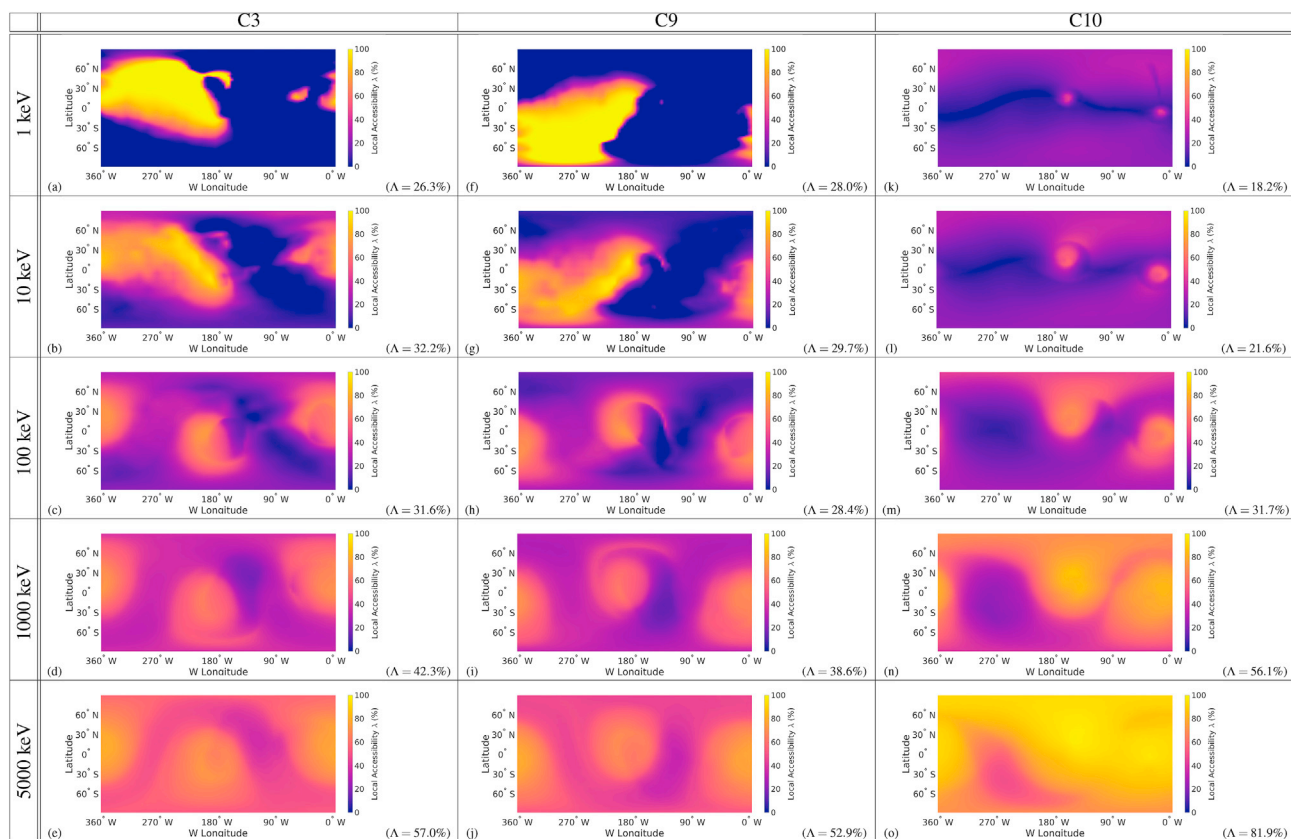

Fig. 13. Local (λ) and global (Λ) energetic H$^+$ ion accessibility of Callisto during the (a)–(e) C3, (f)–(j) C9, and (k)–(o) C10 Galileo flybys. Select energies are the same as shown in Figs. 4, 6, 8 and 10. See Fig. 4 and the text for further discussion.

beneath the moon's surface. However, the model of Hartkorn and Saur (2017) is unable to reproduce the strength of the magnetic signatures that were observed during the C9 flyby which occurred in Callisto's nightside hemisphere where the ionospheric density is low.

To study energetic ion dynamics during C3 and C9, we use the electromagnetic fields from the AIKEF hybrid simulations presented in Appendix A of Liuzzo et al. (2015). Similar to various preceding studies, these authors were able to quantitatively explain magnetic field data from *both* flybys by considering the plasma interaction with an induced dipole field at Callisto, and without any contributions from the moon's ionosphere (i.e., neither the thermal plasma interaction with the ionosphere nor induction within the ionosphere). The setup of these simulations therefore corresponds best to Run #2 in our present study (see Table 1 as well as Figs. 2 and 3). We note, however, that the density of the magnetospheric upstream plasma in the simulations of Liuzzo et al. (2015) was a factor of approximately six lower than the present study, thereby weakening the plasma interaction compared to Run #2.

The accessibility patterns of Callisto to energetic H^+ ions during the C3 and C9 flybys are presented in Fig. 13(a)–(e) and Fig. 13(f)–(j), respectively, at the same energies as in Figs. 4, 6, 8 and 10. Because the accessibility patterns of O^{2+} and S^{3+} ions are again qualitatively similar to those of H^+, but simply shifted to lower energies, they are not shown for these flybys.

For the C3 and C9 encounters, the accessibility patterns resemble those of Run #2: at energies $E < 100$ keV, a clear leading/trailing asymmetry is visible with energetic ion accessibility maximized in Callisto's trailing hemisphere and minimized in the leading hemisphere. Compared to Run #2, however, the proton accessibility patterns on the surface of Callisto are slightly rotated around the x-axis for C3 and C9. For the electromagnetic fields from the C3 flyby, the 19° southward rotation of the background field $\mathbf{B}_0$ against the $z = 0$ plane causes the accessibility pattern to rotate around the x-axis by approximately the same angle. Regions of high accessibility are moved southward in Callisto's Jupiter-averted hemisphere near 180° W longitude and northward in the Jupiter-facing hemisphere near 0° W longitude (see Fig. 13(a) and (b)).

For the C9 flyby, the strong component of the background magnetic field along the $+y$-axis (i.e., $\mathbf{B}_0$ for C9 is nearly anti-parallel to $\mathbf{B}_0$ for Run #2 and C3) causes regions of high accessibility to mainly form in Callisto's *southern* trailing hemisphere and no longer in the *northern* hemisphere (cf. Fig. 6(a), (b), Fig. 13(a), or (b) with (f) and (g)). During C9, the 15° southward rotation of the background field against the $z = 0$ plane results in regions of high accessibility that now migrate slightly northward in the Jupiter-averted hemisphere and southward in the Jupiter-facing hemisphere.

At higher energies for C3 and C9 (see Fig. 13(c)–(e) and 13(h)–(j), respectively), "clusters" of high accessibility again begin to form near the moon's "magnetic poles." Although the non-zero $B_{z,0}$ component means that the dipole no longer exactly cancels the background field at any point on Callisto's surface, the superposition of the background and induced fields still results in $|\mathbf{B}|$ minimized (and thus, proton gyroradii maximized) near the "magnetic poles." However, the clusters are no longer centered around Callisto's equatorial plane (as with Run #2) but are slightly displaced toward the north or the south. These clusters of high accessibility tend to follow the rotation of $\mathbf{B}_0$ against the $z = 0$ plane, and center around locations where the magnetic field is nearly perpendicular to Callisto's surface. Similar to Run #2, the locations of these clusters with high proton accessibility are therefore not only determined by a locally reduced magnetic field which increases proton gyroradii (as discussed in Section 3.3), but also depend on a strong component of the magnetic field perpendicular to Callisto's surface which facilitates escape of the *back-traced* ions along the field lines.

Additionally, incomplete "rings" of reduced accessibility are visible in regions where the magnetic field is nearly tangential to Callisto's surface,

which facilitates immediate impacts of *back-traced* energetic protons (see Fig. 13(c), (d), (h), and (i)). Beyond energies of $E = 1000$ keV, the clusters begin to merge and the accessibility pattern again approaches quasi-homogeneity.

The C10 Galileo flyby of Callisto occurred on 17 September 1997. At the time of closest approach, the moon was located at a smaller distance to the center of the Jovian magnetospheric current sheet than during C3 and C9 (approximately $2.5R_J$ *below* the center). Near closest approach, the magnetospheric background field vector was $\mathbf{B}_0 = [0.0\hat{\mathbf{x}} + 28.95\hat{\mathbf{y}} - 11.22\hat{\mathbf{z}}]$ nT; i.e., the field pointed toward Jupiter and was rotated southward by a 21° angle against the $z = 0$ plane. During the flyby, Callisto's induced magnetic moment was anti-parallel to the y-axis, but the non-zero $B_{z,0}$ component again means that the induced dipole field was no longer anti-parallel to the background field near the moon's "magnetic poles." Measurements of Callisto's magnetic environment during C10 indicated a complex admixture of plasma interaction and induction signatures. Callisto's Alfvén wings dominated far from the moon, whereas the induced dipole was only visible within the wakeside quasi-dipolar "core region" (Liuzzo et al., 2016).

To investigate energetic ion dynamics during the C10 flyby, we use the electromagnetic fields obtained from the AIKEF hybrid simulation presented in Liuzzo et al. (2016). That study considered the contributions of Callisto's ionosphere and induced dipole to its plasma interaction, so the field perturbations most closely resemble those of Run #4 studied here (see Table 1 as well as Figs. 2 and 3). The magnetospheric upstream parameters are documented in Section 3 of Liuzzo et al. (2016).

Fig. 13(k)–(o) display energetic H^+ accessibility patterns during the C10 flyby for the same energies as above. The two clusters of high accessibility visible in Fig. 13(k)–(m) for protons with energies $E \leq 100$ keV are shifted toward southern latitudes in Callisto's Jupiter-facing hemisphere (near 0° W longitude), and toward northern latitudes in its Jupiter-averted hemisphere (near 180° W longitude). Similar to Run #4, these clusters preferentially form where $\mathbf{B}_0$ is nearly perpendicular to Callisto's surface, i.e., in regions where H^+ gyration within the electric field void that surrounds Callisto facilitates escape of *back-traced* ions.

However, the background magnetic field component perpendicular to the magnetic moment (namely $B_{z,0}$) results in Alfvén wings that are tilted with respect to the $z = 0$ plane which contains $\mathbf{M}_{\mathrm{ind}}$ (see Fig. 2(a) of Liuzzo et al. (2016)). This rather complex geometry results in new features to form in the proton accessibility patterns, such as a wavy, band-like region of reduced accessibility that nearly follows Callisto's geographic equator. In Callisto's trailing hemisphere, this band is caused by the tilted magnetospheric field piling up against the moon's ionosphere. In the leading hemisphere, the wavy structure of this band is an imprint of the $B_x = 0$ region associated with the transition from the quasi-dipolar "core region" to the Alfvén wings (Liuzzo et al., 2016). At energies $E > 100$ keV (Fig. 13(n) and (o)), the two clusters again begin to merge and accessibility rapidly approaches $\lambda \approx 100\%$ everywhere, similar to the proton accessibility of Run #4.

5. Discussion: energetic ion accessibility during Callisto's diverse plasma interaction scenarios

The change in global (average) proton accessibility Λ between Runs #1, #2, #3, and #4 is illustrated in Fig. 14. At a given starting energy below $E = 5000$ keV, Callisto is least accessible to energetic protons for the plasma interaction scenario of Run #4 (i.e., for the interaction with Callisto's ionosphere and induced dipole). Compared to the other three scenarios (see Table 1), the plasma interaction of Run #4 is the strongest, which leads to the largest currents and associated perturbations in the magnetic field. Proton gyroradii in Run #4 are therefore minimized compared to the size of the moon. Hence, Callisto is most effectively shielded from energetic protons when the plasma interaction with the moon's ionosphere *and* induced dipole is present. Such an interaction
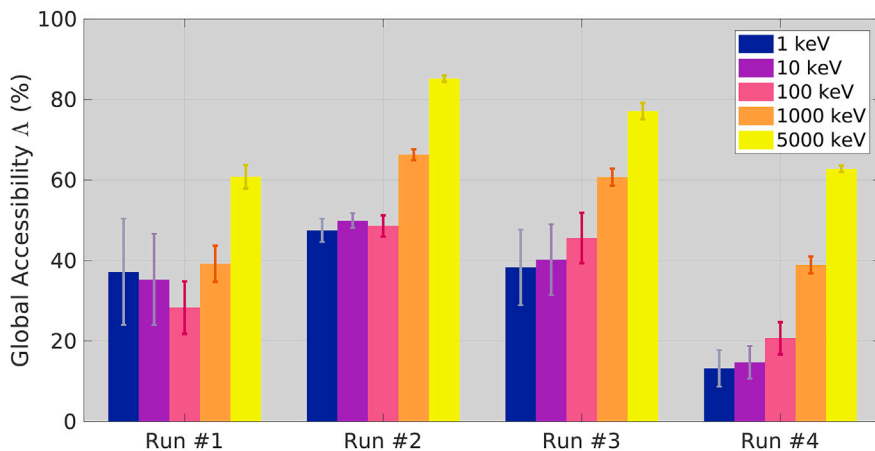
Fig. 14. Global proton accessibilities of Runs #1 through #4. For each simulation scenario from Table 1, the 5 bars illustrate global accessibility for proton energies of (blue) 1 keV, (purple) 10 keV, (pink) 100 keV, (orange) 1000 keV, and (yellow) 5000 keV. The energies, and the respective Λ values for each run, are identical to those already shown in Figs. 4, 6, 8 and 10. Vertical bars indicate the standard deviations of the local accessibility (λ) around the global accessibility value (Λ) for each run and energy. (For interpretation of the references to color in this figure legend, the reader is referred to the Web version of this article.)

scenario occurs when Callisto is located at intermediate distances from the center of the Jovian magnetospheric current sheet. At larger distances, the plasma interaction would be weaker (tending to the fields of Runs #1 and #2), whereas closer to the center of the Jovian current sheet, the induced dipole would nearly vanish (tending to the fields of Run #3). The reduced values of Λ in Run #4 are also consistent with global accessibility during the C3, C9, and C10 flybys, since average accessibilities during C3 and C9 (with fields similar to those of Run #2) are greater than or approximately equal to those of C10 (with fields similar to those of Run #4) for energies $E < 1000$ keV (see Fig. 13).

Fig. 14 also shows that a monotonic increase in average proton accessibility with increasing energy occurs *only* when the thermal plasma interaction with Callisto's ionosphere is taken into account (i.e., for Runs #3 and #4). For a weak interaction of the magnetospheric plasma with Callisto's induced dipole alone (Run #1), the global accessibility displays a clear non-monotonic dependence on energy. For the energy range studied here, a decrease in global accessibility Λ occurs until energies near the corkscrew energy E_{gr} (i.e., near $E \approx 314$ keV for an H^+ ion). Above this energy, the gyroradii of H^+ ions are greater than the radius of Callisto; i.e., *back-traced* protons are able to gyrate around the moon and escape, causing the global accessibility to then *increase* at energies greater than E_{gr}.

When the interaction with Callisto's induced dipole is stronger (Run #2), the average proton accessibility Λ is nearly independent of energy for $E = 1$ keV, 10 keV, and 100 keV. At these three energies, regions of high proton accessibility are only redistributed around Callisto's surface, but no appreciable change of Λ with increasing energy occurs (see also Fig. 6).

As can be seen in Fig. 14, the standard deviation of the individual λ values around the average Λ generally decreases with energy in all four plasma interaction scenarios. A reduction of the spread of local accessibilities around the average again illustrates that the proton accessibility patterns tend toward homogeneity with increasing particle energy for all of the thermal plasma interaction scenarios.

For all starting energies considered here, Fig. 14 reveals that a slightly stronger plasma interaction with Callisto's induced dipole alone (Run #2) results in a larger global accessibility Λ than for a weak plasma interaction with the dipole alone (Run #1). Moreover, excluding the proton accessibility of Run #1 at the highest energy considered (i.e., $E = 5000$ keV), *all* values of Λ in Run #1 are less than *any* average accessibility value in Run #2, even at the lowest energy of $E = 1$ keV. This difference is caused by the plasma interaction which stretches regions of reduced magnetic field toward downstream, thereby increasing the size of regions with large proton gyroradii and enhancing accessibility of Callisto.

For O^{2+} and S^{3+} ions in the energy range studied here and for all four interaction scenarios considered (see Appendices A–D), global accessibility always increases *monotonically* with increasing energy (see Fig. A 16 through D.19). Compared to H^+, the accessibility patterns of O^{2+} and S^{3+} ions are merely shifted to lower energies. Therefore, while a non-monotonic increase in accessibility for O^{2+} and S^{3+} may occur for the thermal plasma population (below $E = 1$ keV), accessibility of the energetic population increases monotonically with energy.

The only published energy spectrogram from any close Callisto encounter was obtained during the C3 Galileo flyby (see Fig. 3 of Cooper et al. (2001)). This spectrogram displays the intensity of particle fluxes for energetic hydrogen, oxygen, and sulfur ions, and consists of measurements taken by Galileo at various times between 11:00 and 16:00 on 04 November 1996. During the C3 encounter, closest approach to Callisto occurred at 13:34; i.e., this spectrogram includes data that were collected in the inbound and outbound segments of closest approach to the moon. The 5 h time interval during which measurements were taken is much longer than the time that Galileo spent in Callisto's local plasma interaction region (only on the order of approximately 30 min, see, e.g., Liuzzo et al. (2015)). Thus, we assume that the spectrogram from Fig. 3 of Cooper et al. (2001) is only weakly influenced by Callisto's local plasma interaction, and is representative of the ambient energetic ion distribution during the C3 encounter.

We are therefore able to constrain the average intensity of energetic ion flux at the top of Callisto's atmosphere ($I_{TOA}(E)$) during the C3 flyby by assuming that the measured ambient distribution is spatially homogeneous (i.e., that all impinging energetic ions stem from the same distribution). To do so, we multiply the measured intensities $I(E)$ from Cooper et al. (2001) with the average accessibility $\Lambda(E)$, in analogy to the approach of Regoli et al. (2016) for Titan (see Section 3.3 in that work). We assume that the change in $\Lambda(E)$ between the five discrete energies in Fig. 13(a)–(e) is approximately linear. While we focus only on the H^+ ions, the results would be similar for O^{2+} and S^{3+} ions, as the energy dependence of the fluxes for these two species is qualitatively very similar to that of H^+ (see Fig. 3 of Cooper et al. (2001)).

In Fig. 15, the intensity of energetic proton flux measured by Galileo ($I(E)$) is displayed in purple, whereas the average flux incident onto Callisto's atmosphere ($I_{TOA}(E)$) is displayed in orange. The low global accessibility for protons with energies between 10 keV and 100 keV (on the order of $\Lambda \approx 30\%$) drastically reduces the average intensity $I_{TOA}(E)$ of energetic protons incident onto the moon's atmosphere in that energy range. At higher energies, the increased value of $\Lambda(E)$ results in a flux $I_{TOA}(E)$ that is closer to the measured ambient flux $I(E)$, but is nonetheless decreased by approximately three orders of magnitude compared to the flux at 10 keV and 100 keV (as a consequence of the measured energy
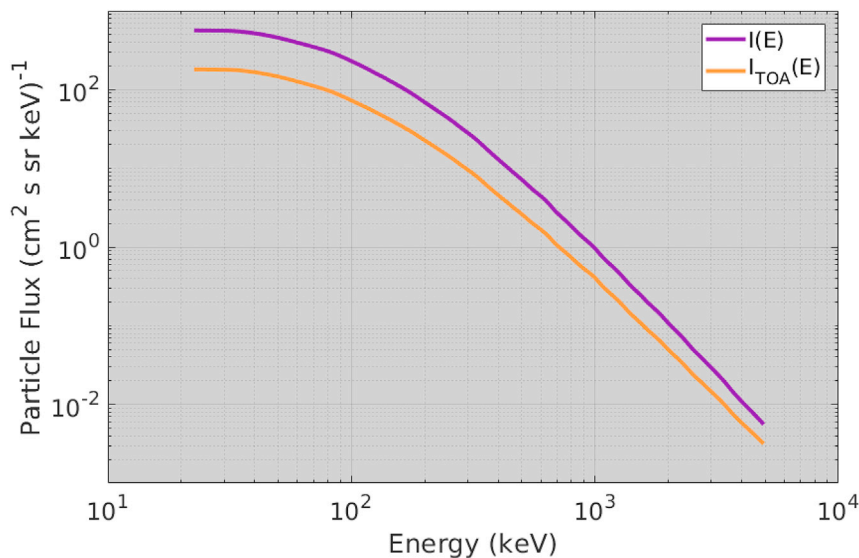
Fig. 15. Intensity of energetic proton flux near Callisto during the Galileo C3 flyby. The $I(E)$ line (purple) depicts the averaged, measured intensity of energetic proton flux for energies $E \leq 5000$ keV between 11:00 and 16:00 on 04 November 1996, obtained from Fig. 3 of Cooper et al. (2001). The $I_{TOA}(E) = \Lambda(E) \cdot I(E)$ line (orange) denotes the average energetic proton flux onto the top of Callisto's atmosphere, taking into account the reduction of the flux as a result of the thermal plasma interaction with Callisto's induced dipole (see Section 4). The electromagnetic fields calculated by Liuzzo et al. (2015) for the C3 flyby are used to determine the accessibilities (see, e.g., Section 4 and Fig. 13 of this study). (For interpretation of the references to color in this figure legend, the reader is referred to the Web version of this article.)

distribution, which decays drastically with increasing energy).

Although time series of energetic ion count rates near Callisto have not been published in the peer-reviewed literature, they are available at the web page for the EPD instrument (*http://sd-www.jhuapl.edu/Galileo_EPD*). However, raw EPD measurements from all eight Callisto flybys show no discernible signature of the moon's influence on the energetic ion population in any of the energy channels. This lack of observed features associated with Callisto is much different from energetic ion measurements at the other icy Galilean moons. At Ganymede and Europa, the moons' influence on energetic ion dynamics is visible in, e.g., dropout signatures demarcated by a reduced energetic ion count rate of the instrument (e.g., Williams et al. (1997b); Paranicas et al. (2000)). Since observability of such features strongly depends on the viewing geometry of the EPD instrument, explaining why the measurements from the eight Callisto flybys are devoid of any drop-out features is beyond the scope of this study.

6. Concluding remarks and outlook

This study has analyzed energetic ion dynamics near the Jovian moon Callisto for four distinct scenarios of the moon's Alfvénic plasma interaction: a weak interaction with its induced dipole, a stronger interaction with its induced dipole, an interaction with its ionosphere alone, and an interaction with its ionosphere *and* induced dipole in combination. Our findings have also been applied to analyze Callisto's energetic ion environment at the times of the Galileo C3, C9, and C10 flybys.

Our results have shown that Callisto's plasma interaction has a substantial effect on accessibility of the moon to energetic ions. Moreover, there is a distinct variability of the local accessibility distribution and the global/average accessibility as a function of System III longitude (represented by the four interaction scenarios presented throughout this

study). Therefore, consideration of the Alfvénic plasma interaction is crucial to constrain energetic ion dynamics near Callisto.

The imprint of Callisto's induced magnetic field on energetic ion accessibility is evident even in the case of a strong plasma interaction with the moon's ionosphere *and* induced dipole: characteristic rings of reduced accessibility are "carved out" of localized clusters of high accessibility. A future well-placed Callisto flyby through the wakeside quasi-dipolar "core region" may therefore observe highly-localized peaks and troughs in energetic particle spectra. Thus, measurements from energetic ion detectors (e.g., the *Particle Environment Package* on board the upcoming JUICE mission) may potentially be used to support identification of induction signals at Callisto. This is true even when the plasma interaction with the moon's ionosphere and induced dipole is strong and the unobscured induction signature is visible only in a narrow region at Callisto's wakeside.

Appendix A. Energetic O^{2+} and S^{3+} accessibility for Run #1

Maps depicting the accessibility of Callisto to O^{2+} and S^{3+} ions at select energies and for the electromagnetic fields of Run #1 are shown in Fig. A 16. Accessibility maps are only shown up to those energies where the global accessibility Λ approaches 100%, and the local accessibility distribution becomes quasi-homogeneous. For a given energy, the local accessibility distributions of O^{2+} and S^{3+} ions are very similar, as their mass-to-charge ratios differ only by a factor of 1.3. At energies of 1 keV and 10 keV for O^{2+} ions (Fig. A 16(a) and (b)) as well as for S^{3+} ions (Fig. A 16(e) and (f)), similar north/south and leading/trailing asymmetries are present as for H^+ ion accessibility (Fig. 4(a) and (b)). However, compared to H^+ ions (see Fig. 4), the increased gyroradii of O^{2+} and S^{3+} ions (due to their larger mass-to-charge ratios) result in "shoulders" of non-zero ion accessibility in Callisto's leading hemisphere at high northern latitudes. Additionally, the clustering of regions that are highly accessible to O^{2+} and S^{3+} ions near Callisto's "magnetic poles"a is already slightly more prominent at these lower energies compared to H^+, due to locally increased gyroradii in the regions of reduced magnetic

field, that allows these *back-traced* heavy ions to gyrate around the solid body of Callisto and escape.
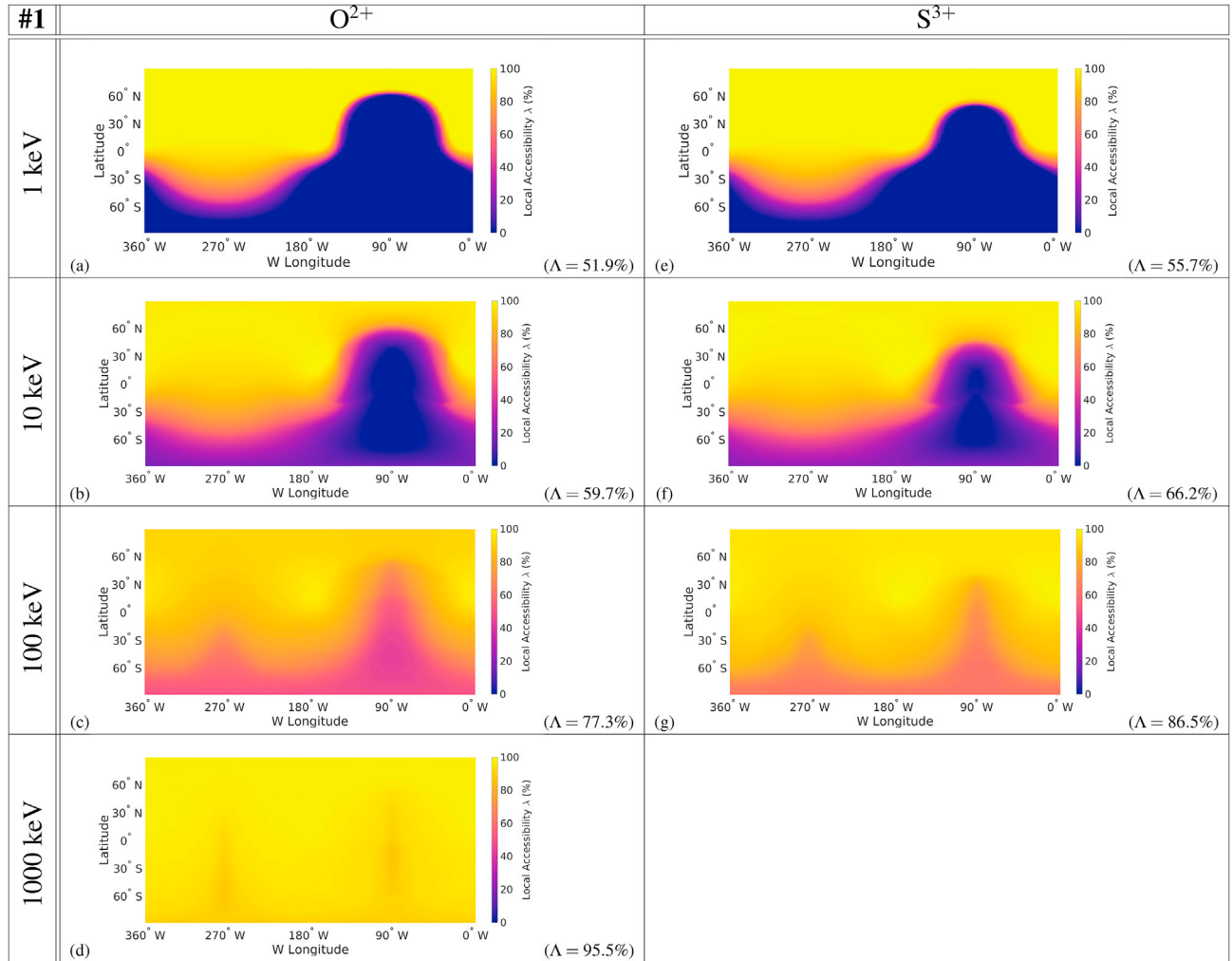

Fig. A.16. Energetic ion accessibility of Callisto at select energies for the electromagnetic fields of Run #1 (see Table 1). Local accessibility λ for energetic O^{2+} (panels (a)–(d)) and S^{3+} (panels (e)–(g)) ions is shown, with lowest local accessibility ($\lambda=0\%$) in blue, and highest local accessibility ($\lambda = 100\%$) in yellow. Global proton accessibility Λ is listed at the right of each panel. No accessibility maps are shown at higher energies once global accessibility reaches $\Lambda \approx 100\%$ and the accessibility pattern becomes quasi-homogeneous.

With increasing energy of $E = 100$ keV up to $E = 1000$ keV for O^{2+} (Fig. A 16(c) and (d)) and at $E = 100$ keV for S^{3+} (Fig. A 16(g)), these "shoulders" extend more and more toward southern latitudes as they surround the apex of Callisto's leading hemisphere (at 0° latitude at 90° W longitude). Ultimately, the two "shoulders" merge together, and accessibility becomes uniformly high. These O^{2+} and S^{3+} accessibility maps reveal that the least accessible regions for energetic ions above their respective corkscrew energies E_{gr} are located not only near 90° W in Callisto's leading hemisphere (as already seen in the H^+ maps), but also near 270° W around the moon's geometric south pole. Although r_g exceeds the radius of Callisto for O^{2+} and S^{3+} ions with energies $E > E_{gr}$ (see Table 2), not all of these ions are able to escape Callisto as some of them gyrate into the moon slightly after initialization, and the local accessibility therefore remains slightly below $\lambda = 100\%$ until $E > 1000$ keV for O^{2+}, and $E > 100$ keV for S^{3+}.

Appendix B. Energetic O^{2+} and S^{3+} accessibility for Run #2

The local and global accessibilities of energetic O^{2+} and S^{3+} ions at select energies and for the electromagnetic fields of Run #2 are presented in Fig. B 17. For these fields, the local accessibility patterns of O^{2+} and S^{3+} ions are similar to the patterns of H^+ ions (cf. Fig. 6(a)–(e)). As with H^+ ions, Callisto's southern hemisphere is almost completely inaccessible to O^{2+} and S^{3+} ions with $E < E_{gr}$, due to the radial orientation of the local electric field and the cycloidal arcs being opened toward the south (see Fig. 7(b)).

Compared to the O^{2+} and S^{3+} accessibility of Run #1, the "shoulders" of high accessibility that were visible in Callisto's northern leading hemisphere now extend all the way down to equatorial latitudes in Run #2. Due to this equatorward expansion of regions with high accessibility, the quasi-rectangular segments of reduced accessibility (depicted in blue) in Callisto's northern leading hemisphere have drastically shrunk in Fig. A 16(a) and (e), compared to Fig. A 16(a) and (e). With increasing energy, local accessibility values rapidly approach $\lambda \approx 100\%$ at all locations except for narrow bands near 90° W and 270° W longitudes, where accessibility remains slightly below $\lambda = 100\%$ for these species.
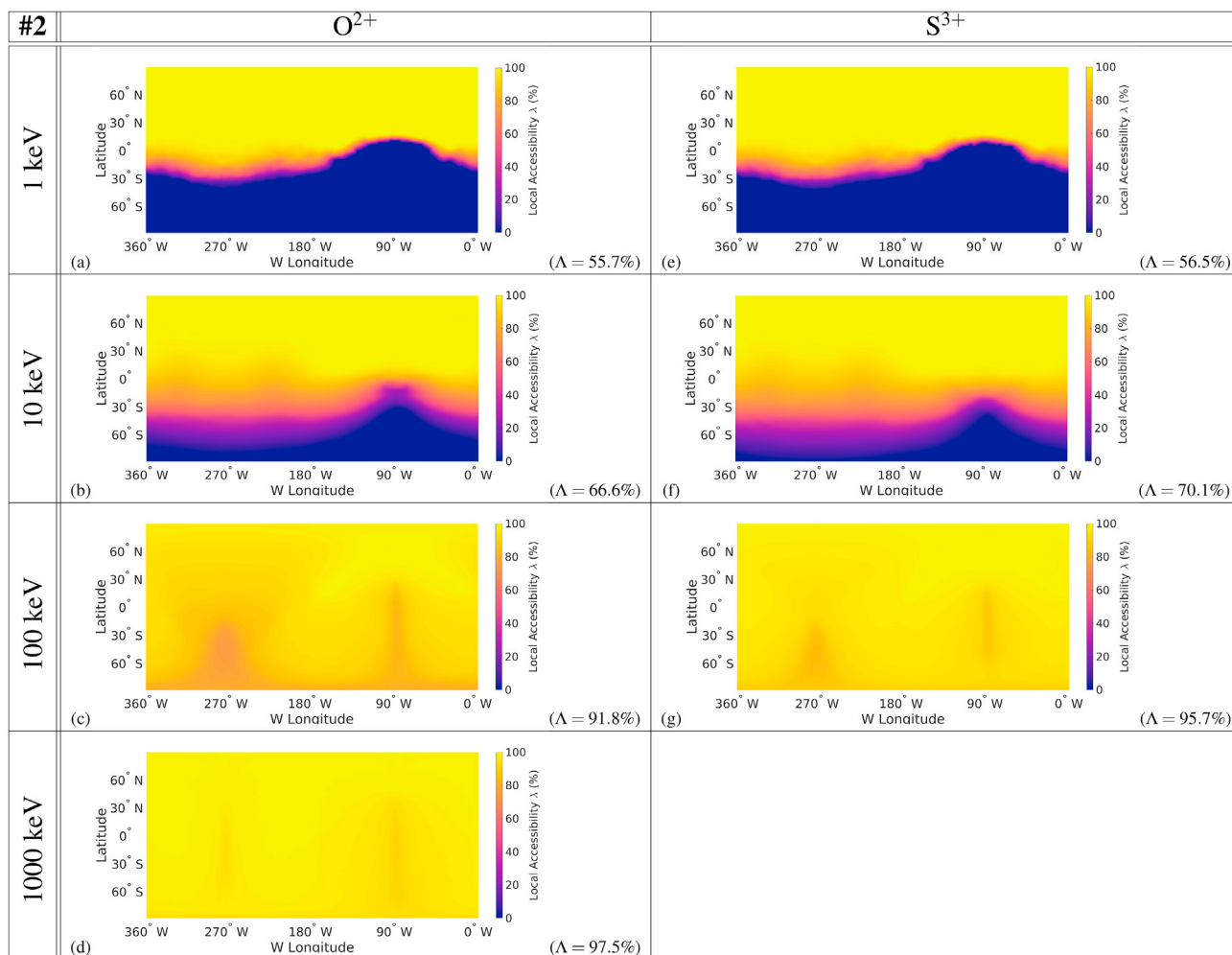
Fig. B.17. Energetic O^{2+} and S^{3+} ion accessibility of Callisto at select energies for the electromagnetic fields of Run #2 (see Table 1). See Fig. A 16 for further description.

The differences in the local and global accessibilities of energetic H^+, O^{2+}, and S^{3+} ions are mainly of a quantitative nature only. For all three species, Callisto's southern hemisphere is inaccessible at lower energies, as the local electric field orientation drastically reduces accessibility by causing a greater amount of ions to impact. In its northern leading hemisphere, the thermal plasma interaction with the moon's induced dipole facilitates ion escape, making Callisto more globally accessible to energetic ions for the electromagnetic fields of Run #2 compared to Run #1 (see, e.g., Fig. 14).

Appendix C. Energetic O^{2+} and S^{3+} accessibility for Run #3

Local and global accessibilities of energetic O^{2+} and S^{3+} ions at select energies and for the electromagnetic fields of Run #3 are presented in Fig. C 18. The accessibility patterns of the heavy energetic ions for Run #3 look very similar to those of protons (cf. Fig. 8(a)–(e)). Similar to H^+, clusters of high accessibility form at longitudes near 35° W and 145° W and extend toward Callisto's geographic poles. At 1 keV (see Fig. C 18(a) and (e)), the bands of reduced accessibility that separate these clusters are again asymmetric in width, with the band in Callisto's trailing hemisphere approximately 30° wide, and the band in the leading hemisphere approximately 10° wide. These regions of reduced accessibility start to "collapse" at a lower energy than for protons, due to the larger gyroradii of O^{2+} and S^{3+} ions (compared to the gyroradii of protons at a given energy).
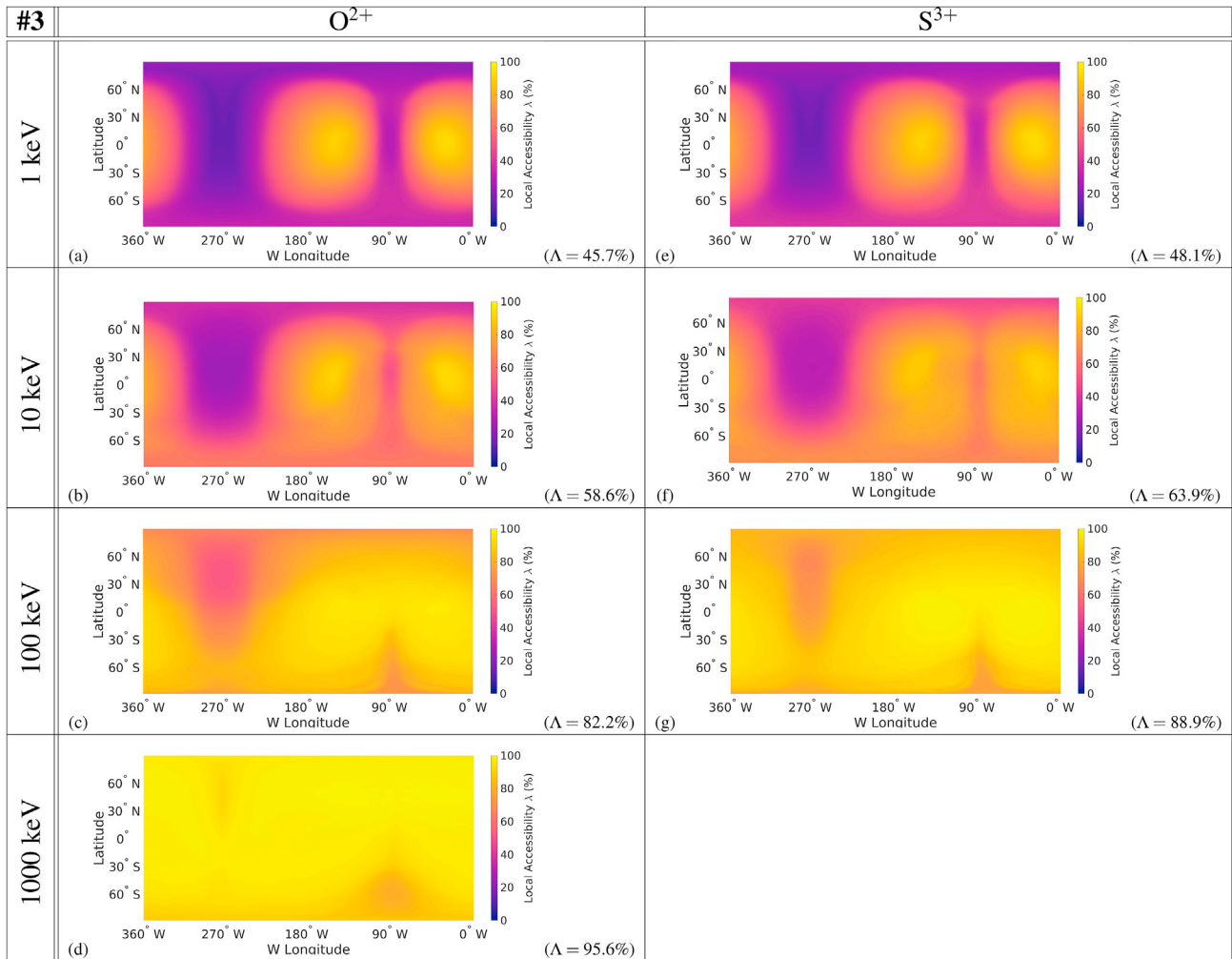
Fig. C.18. Energetic O^{2+} and S^{3+} ion accessibility of Callisto at select energies for the electromagnetic fields of Run #3 (see Table 1). See Fig. A 16 for further description.

Appendix D. Energetic O^{2+} and S^{3+} accessibility for Run #4

Local and global accessibilities for O^{2+} and S^{3+} ions at select energies for the electromagnetic fields of Run #4 are displayed in Fig. D 19. For these species, ions at $E = 1$ keV display similar features in accessibility as H^+ ions at $E \leq 100$ keV: clusters of high accessibility are "carved out" by two rings of reduced accessibility, where the quasi-dipolar "core region" locally generates more impacts of the back-traced ions (see also Fig. 10(a)–(c)). At higher energies these clusters merge, the rings disappear, and accessibility in Callisto's southern hemisphere increases, similar to that of the H^+ ions. Since at a given energy, the gyroradii of O^{2+} and S^{3+} ions are much larger than those of protons, the sequence of accessibility patterns seen in Fig. 10(a)–(e) is shifted toward lower energies for the two heavier species (see Fig. D 19(a)–(g)).
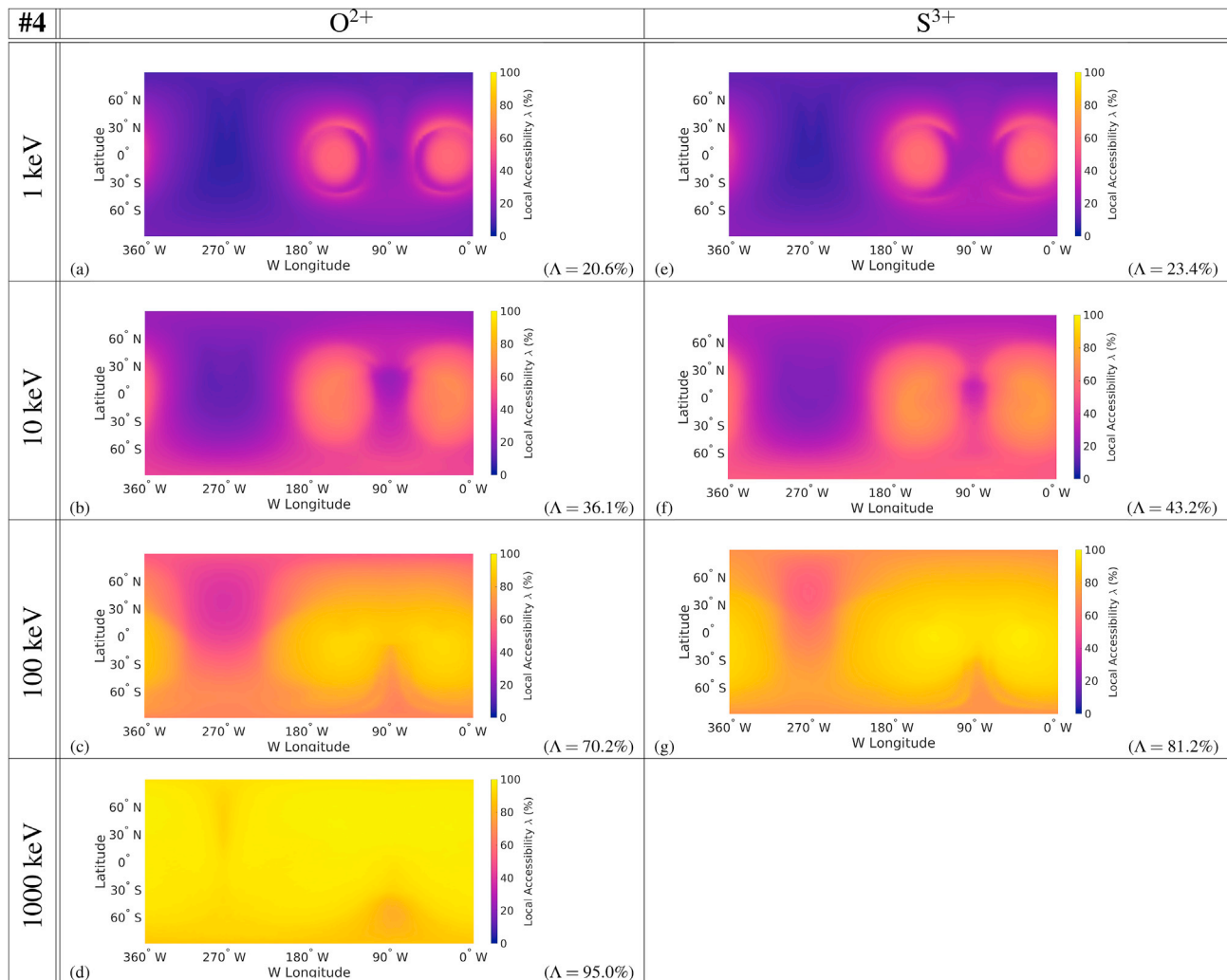
Fig. D.19. Energetic O^{2+} and S^{3+} ion accessibility of Callisto at select energies for the electromagnetic fields of Run #4 (see Table 1). See Fig. A 16 for further description.

References

Arridge, C.S., André, N., Bertucci, C.L., Garnier, P., Jackman, C.M., Németh, Z., Rymer, A.M., Sergis, N., Szego, K., Coates, A.J., Crary, F.J., 2011. Upstream of Saturn and titan. Space Sci. Rev. 162, 25–83. https://doi.org/10.1007/s11214-011-9849-x.

Bagenal, F., Sidrow, E., Wilson, R.J., Cassidy, T.A., Dols, V., Crary, F.J., Steffl, A.J., Delamere, P.A., Kurth, W.S., Paterson, W.R., 2015. Plasma conditions at Europas orbit. Icarus 261, 1–13. https://doi.org/10.1016/j.icarus.2015.07.036.

Bhattacharyya, D., Clarke, J.T., Montgomery, J., Bonfond, B., Gérard, J.-C., Grodent, D., 2017. Evidence for auroral emissions from Callisto's footprint in HST UV images. J. Geophys. Res.: Space Physics 364–373. https://doi.org/10.1002/2017JA024791.

Carlson, R.W., 1999. A tenuous carbon dioxide atmosphere on Jupiter's moon Callisto. Science 283, 820. https://doi.org/10.1126/science.283.5403.820.

Cassidy, T., Paranicas, C., Shirley, J., Dalton III, J., Teolis, B., Johnson, R., Kamp, L., Hendrix, A., 2013. Magnetospheric ion sputtering and water ice grain size at Europa. Planet. Space Sci. 77, 64–73. https://doi.org/10.1016/j.pss.2012.07.008.

Collier, M.R., Hamilton, D., 1995. The relationship between kappa and temperature in energetic ion spectra at Jupiter. Geophys. Res. Lett. 22, 303–306. https://doi.org/10.1029/94GL02997.

Cooper, J.F., Johnson, R.E., Mauk, B.H., Garrett, H.B., Gehrels, N., 2001. Energetic ion and electron irradiation of the icy Galilean satellites. Icarus 149, 133–159. https://doi.org/10.1006/icar.2000.6498.

Dalton, J., Cassidy, T., Paranicas, C., Shirley, J., Prockter, L., Kamp, L., 2013. Exogenic controls on sulfuric acid hydrate production at the surface of Europa. Planet. Space Sci. 77, 45–63. https://doi.org/10.1016/j.pss.2012.05.013.

Dessler, A., 1983. Coordinate systems. In: Dessler, A.J. (Ed.), Physics of the Jovian Magnetosphere. Cambridge University Press, pp. 498–504.

Exner, W., Heyner, D., Liuzzo, L., Motschmann, U., Shiota, D., Kusano, K., Shibayama, T., 2018. Coronal mass ejection hits Mercury: AIKEF hybrid-code results compared to MESSENGER data. Planet. Space Sci. 153, 89–99. https://doi.org/10.1016/j.pss.2017.12.016.

Fatemi, S., Poppe, A., Khurana, K., Holmström, M., Delory, G., 2016. On the formation of Ganymede's surface brightness asymmetries: kinetic simulations of Ganymede's magnetosphere. Geophys. Res. Lett. 43, 4745–4754. https://doi.org/10.1002/2016GL068363.

Feyerabend, M., Liuzzo, L., Simon, S., Motschmann, U., 2017. A three-dimensional model of Pluto's interaction with the solar wind during the New Horizons encounter. J. Geophys. Res.: Space Physics 122, 10356–10368. https://doi.org/10.1002/2017JA024456.

Feyerabend, M., Simon, S., Motschmann, U., Liuzzo, L., 2015. Filamented ion tail structures at Titan: a hybrid simulation study. Planet. Space Sci. 117, 362–376. https://doi.org/10.1016/j.pss.2015.07.008.

Geiss, J., Gloeckler, G., Balsiger, H., Fisk, L., Galvin, A., Gliem, F., Hamilton, D., Ipavich, F., Livi, S., Mall, U., Ogilvie, K., von Steiger, R., Wilken, B., 1992. Plasma composition in Jupiter's magnetosphere: initial results from the solar wind ion composition spectrometer. Science 257, 1535–1539. https://doi.org/10.1126/science.257.5076.1535.

Gurnett, D.A., Persoon, A.M., Kurth, W.S., Roux, A., Bolton, S.J., 2000. Plasma densities in the vicinity of Callisto from Galileo plasma wave observations. Geophys. Res. Lett. 27, 1867–1870. https://doi.org/10.1029/2000GL003751.

Hamilton, D., Gloeckler, G., Krimigis, S., Lanzerotti, L., 1981. Composition of nonthermal ions in the Jovian magnetosphere. J. Geophys. Res.: Space Physics 86, 8301–8318. https://doi.org/10.1029/JA086iA10p08301.

Hartkorn, O., Saur, J., 2017. Induction signals from Callisto's ionosphere and their implications on a possible subsurface ocean. J. Geophys. Res.: Space Physics 122, 11677–11697. https://doi.org/10.1002/2017JA024269.

Ip, W.-H., Williams, D., McEntire, R., Mauk, B., 1997. Energetic ion sputtering effects at Ganymede. Geophys. Res. Lett. 24, 2631–2634. https://doi.org/10.1029/97GL02814.

Ip, W.-H., Williams, D., McEntire, R., Mauk, B., 1998. Ion sputtering and surface erosion at Europa. Geophys. Res. Lett. 25, 829–832. https://doi.org/10.1029/98GL00472.

Kabanovic, S., Feyerabend, M., Simon, S., Meeks, Z., Wulms, V., 2018. Influence of asymmetries in the magnetic draping pattern at Titan on the emission of energetic neutral atoms. Planet. Space Sci. 152, 142–164. https://doi.org/10.1016/j.pss.2017.12.017.

Keppler, E., Krupp, N., 1996. The charge state of helium in the Jovian magnetosphere: a possible method to determine it. Planet. Space Sci. 44, 71–75. https://doi.org/10.1016/0032-0633(95)00076-3.

Khurana, K.K., Kivelson, M.G., Stevenson, D.J., Schubert, G., Russell, C.T., Walker, R.J., Polanskey, C., 1998. Induced magnetic fields as evidence for subsurface oceans in Europa and Callisto. Nature 395, 777–780. https://doi.org/10.1038/27394.

Kivelson, M.G., Bagenal, F., Kurth, W.S., Neubauer, F.M., Paranicas, C., Saur, J., 2004. Magnetospheric interactions with satellites. In: Bagenal, F., Dowling, T.E., McKinnon, W.B. (Eds.), Jupiter: the Planet, Satellites and Magnetosphere. Cambridge Univ. Press, pp. 513–536.

Kivelson, M.G., Khurana, K.K., Stevenson, D.J., Bennett, L., Joy, S., Russell, C.T., Walker, R.J., Zimmer, C., Polanskey, C., 1999. Europa and Callisto: induced or intrinsic fields in a periodically varying plasma environment. J. Geophys. Res. 104, 4609–4626. https://doi.org/10.1029/1998JA900095.

Kliore, A.J., Anabtawi, A., Herrera, R.G., Asmar, S.W., Nagy, A.F., Hinson, D.P., Flasar, F.M., 2002. Ionosphere of Callisto from Galileo radio occultation observations. J. Geophys. Res. (Space Physics) 107, 1407. https://doi.org/10.1029/2002JA009365.

Kotova, A., Roussos, E., Krupp, N., Dandouras, I., 2015. Modeling of the energetic ion observations in the vicinity of Rhea and Dione. Icarus 258, 402–417. https://doi.org/10.1016/j.icarus.2015.06.031.

Krupp, N., Roussos, E., Kriegel, H., Kollmann, P., Kivelson, M.G., Kotova, A., Paranicas, C., Mitchell, D., Krimigis, S.M., Khurana, K.K., 2013. Energetic particle measurements in the vicinity of Dione during the three Cassini encounters 2005-2011. Icarus 226, 617–628. https://doi.org/10.1016/j.icarus.2013.06.007.

Liuzzo, L., Feyerabend, M., Simon, S., Motschmann, U., 2015. The impact of Callisto's atmosphere on its plasma interaction with the Jovian magnetosphere. Journal of Geophysical Research (Space Physics) 120, 9401–9427. https://doi.org/10.1002/2015JA021792.

Liuzzo, L., Simon, S., Feyerabend, M., Motschmann, U., 2016. Disentangling plasma interaction and induction signatures at Callisto: the Galileo C10 flyby. J. Geophys. Res.: Space Physics 121, 8677–8694. https://doi.org/10.1002/2016JA023236.

Liuzzo, L., Simon, S., Feyerabend, M., Motschmann, U., 2017. Magnetic signatures of plasma interaction and induction at Callisto: the Galileo C21, C22, C23, and C30 flybys. J. Geophys. Res.: Space Physics 122, 7364–7386. https://doi.org/10.1002/2017JA024303.

Mauk, B., Mitchell, D., McEntire, R., Paranicas, C., Roelof, E., Williams, D., Krimigis, S., Lagg, A., 2004. Energetic ion characteristics and neutral gas interactions in Jupiter's magnetosphere. J. Geophys. Res.: Space Physics 109. https://doi.org/10.1029/2003JA010270.

Müller, J., Simon, S., Motschmann, U., Schüle, J., Glassmeier, K., Pringle, G.J., 2011. A.I.K.E.F.: Adaptive hybrid model for space plasma simulations. Comput. Phys. Commun. 182, 946–966. https://doi.org/10.1016/j.cpc.2010.12.033.

Neubauer, F.M., 1980. Nonlinear standing Alfvén wave current system at Io: Theory. Journal of Geophysical Research (Space Physics) 85, 1171–1178. https://doi.org/10.1029/JA085iA03p01171.

Neubauer, F.M., 1999. Alfvén wings and electromagnetic induction in the interiors: Europa and Callisto. Journal of Geophysical Research (Space Physics) 104, 28671–28684. https://doi.org/10.1029/1999JA900217.

Paranicas, C., Carlson, R., Johnson, R., 2001. Electron bombardment of Europa. Geophys. Res. Lett. 28, 673–676. https://doi.org/10.1029/2000GL012320.

Paranicas, C., McEntire, R., Cheng, A., Lagg, A., Williams, D., 2000. Energetic charged particles near Europa. J. Geophys. Res.: Space Physics 105, 16005–16015. https://doi.org/10.1029/1999JA000350.

Paranicas, C., Ratliff, J., Mauk, B., Cohen, C., Johnson, R., 2002. The ion environment near Europa and its role in surface energetics. Geophys. Res. Lett. 29 https://doi.org/10.1029/2001GL014127.

Pospieszalska, M., Johnson, R., 1989. Magnetospheric ion bombardment profiles of satellites: Europa and Dione. Icarus 78, 1–13. https://doi.org/10.1016/0019-1035(89)90065-1.

Regoli, L., Roussos, E., Feyerabend, M., Jones, G.H., Krupp, N., Coates, A.J., Simon, S., Motschmann, U., Dougherty, M., 2016. Access of energetic particles to Titan's exobase: a study of Cassini's T9 flyby. Planet. Space Sci. 130, 40–53. https://doi.org/10.1016/j.pss.2015.11.013.

Rosenqvist, L., Wahlund, J.-E., Ågren, K., Modolo, R., Opgenoorth, H., Strobel, D., Müller-Wodarg, I., Garnier, P., Bertucci, C., 2009. Titan ionospheric conductivities from Cassini measurements. Planet. Space Sci. 57, 1828–1833. https://doi.org/10.1016/j.pss.2009.01.007.

Roussos, E., Kollmann, P., Krupp, N., Paranicas, C., Krimigis, S., Mitchell, D., Persoon, A., Gurnett, D., Kurth, W., Kriegel, H., et al., 2012. Energetic electron observations of Rhea's magnetospheric interaction. Icarus 221, 116–134. https://doi.org/10.1016/j.icarus.2012.07.006.

Seufert, M., 2012. Callisto: Induction Signals, Atmosphere and Plasma Interaction. Ph.D. thesis Universität zu Köln. .ub.uni-koeln.de/4903.

Seufert, M., Saur, J., Neubauer, F.M., 2011. Multi-frequency electromagnetic sounding of the Galilean moons. Icarus 214, 477–494. https://doi.org/10.1016/j.icarus.2011.03.017.

Simon, S., Kriegel, H., Saur, J., Wennmacher, A., Neubauer, F.M., Roussos, E., Motschmann, U., Dougherty, M.K., 2012. Analysis of Cassini magnetic field observations over the poles of Rhea. J. Geophys. Res. (Space Physics) 117, A07211. https://doi.org/10.1029/2012JA017747.

Simon, S., Saur, J., Neubauer, F.M., Wennmacher, A., Dougherty, M.K., 2011. Magnetic signatures of a tenuous atmosphere at Dione. Geophys. Res. Lett. 38, L15102. https://doi.org/10.1029/2011GL048454.

Strobel, D.F., Saur, J., Feldman, P.D., McGrath, M.A., 2002. Hubble space telescope space telescope imaging spectrograph search for an atmosphere on Callisto: a jovian unipolar inductor. Astrophys. J. 581, L51–L54. https://doi.org/10.1086/345803.

Thomsen, M.F., Van Allen, J.A., 1980. Motion of trapped electrons and protons in Saturn's inner magnetosphere. J. Geophys. Res. Space Physics 85, 5831–5834. https://doi.org/10.1029/JA085iA11p05831.

Williams, D., Mauk, B., McEntire, R., 1997a. Trapped electrons in Ganymede's magnetic field. Geophys. Res. Lett. 24, 2953–2956. https://doi.org/10.1029/97GL03003.

Williams, D., Mauk, B., McEntire, R., Roelof, E., Armstrong, T., Wilken, B., Roederer, J., Krimigis, S., Fritz, T., Lanzerotti, L., et al., 1997b. Energetic particle signatures at Ganymede: implications for Ganymede's magnetic field. Geophys. Res. Lett. 24, 2163–2166. https://doi.org/10.1029/97GL01931.

Williams, D., McEntire, R., Jaskulek, S., Wilken, B., 1992. The Galileo energetic particles detector. Space Sci. Rev. 60, 385–412. https://doi.org/10.1007/BF00216863.

Williams, D.J., Mauk, B., McEntire, R.W., 1998. Properties of Ganymede's magnetosphere as revealed by energetic particle observations. J. Geophys. Res.: Space Physics 103, 17523–17534. https://doi.org/10.1029/98JA01370.

Wulms, V., Saur, J., Strobel, D.F., Simon, S., Mitchell, D.G., 2010. Energetic neutral atoms from Titan: particle simulations in draped magnetic and electric fields. J. Geophys. Res. Space Physics 115, 1–18. https://doi.org/10.1029/2009JA014893.

Zimmer, C., Khurana, K.K., Kivelson, M.G., 2000. Subsurface oceans on Europa and Callisto: constraints from Galileo magnetometer observations. Icarus 147, 329–347. https://doi.org/10.1006/icar.2000.6456.